Title

Numerical tool development of fluid-structure interactions in upper airway for investigation of obstructive sleep apnea

Author

Huang, Chien-Jung

Publication Date

2017

Peer reviewed|Thesis/dissertation

UNIVERSITY OF CALIFORNIA

Los Angeles

Numerical Tool Development of Fluid–Structure Interactions in Upper Airway for Investigation of Obstructive Sleep Apnea

A dissertation submitted in partial satisfaction
of the requirements for the degree
Doctor of Philosophy in Mechanical and Engineering

by

Chien-Jung Huang

2017

ABSTRACT OF THE DISSERTATION

Numerical Tool Development
of Fluid–Structure Interactions in Upper Airway
for Investigation of Obstructive Sleep Apnea

by

Chien-Jung Huang
Doctor of Philosophy in Mechanical and Engineering
University of California, Los Angeles, 2017
Professor Jeffrey D. Eldredge, Chair

Obstructive sleep apnea (OSA) is a medical condition characterized by repetitive partial or complete occlusion of the airway during sleep. The soft tissues in the airway of OSA patients are prone to collapse under the low pressure loads incurred during breathing. A numerical tool suitable for simulation of air-tissue interactions with patient-specific upper airway geometries has been developed. The tool is designed to utilize non-body-fitted Cartesian grid to avoid grid generation and remeshing processes for the deforming irregular geometries. A sharp-interface embedded boundary method is used resolving the airflow in the airway geometries, while a novel cut-cell non-linear finite element analysis is constructed for structure undergoing large deformation. The separate fluid and structure solvers are strongly coupled with a partitioned iterative algorithm. The interface is represented with the signed distance function in the flow and structural solvers. Also, the explicit interface representation with the union of Lagrangian triangle elements is introduced to manage the data exchange between two solvers. The simulation of deformation of cantilever beam under uniformly distributed load demonstrated the ability of the structural solver. The capability of the developed tool dealing with flow induced deformation problems has been exhibited with several two- and three- dimensional validation cases. To obtain the patient-specific airway and soft tissue

geometries, a procedure by which patient-specific airway geometries are segmented and processed from dental cone-beam CT scans into signed distance fields is presented. The results are shown for three-dimensional flow simulation inside two rigid patient-specific airways. The simulation results of fluid–structure interaction of the pressure driven flow surrounded by deformable soft palate and tongue structures are also presented.

The dissertation of Chien-Jung Huang is approved.

Sanjay M. Mallya

Xiaolin Zhong

Lihua Jin

Jeffrey D. Eldredge, Committee Chair

University of California, Los Angeles

2017

TABLE OF CONTENTS

LIST OF FIGURES

LIST OF TABLES

ACKNOWLEDGMENTS

I would like to express my sincere gratitude to my advisor and mentor, Professor Jeff Eldredge, for his support and guidance throughout this research. His guidance is always inspiring and extremely helpful. Without his help and encouragement this dissertation could not have been finished. I also want show my deepest appreciation to my co-advisor, Dr. Sanjay Mallya from UCLA School of Dentistry, for providing precious advice from medical perspectives.

I want to thank my committee members, Professor William Klug, Professor Xiaolin Zhong, and Professor Lihua Jin for their advice during my research.

I am indebt to Dr. Shao-Ching Huang for all the thoughtful discussions and assistance on the numerical experiments. I would like to thank Dr. Susan White for helpful discussions and sharing data. I would like to extend my appreciation to all the members in SOFIA lab for the encouragement and the stimulating conversations.

Last but not least, I would like to offer my special thanks to my family, my significant other, Nick. I could never finished this journey without their love, understanding and tolerance. I am also grateful to my friends who have helped me and supported me along the journey.

VITA

2009	B.S. in Physics, National Taiwan University, Taipei, Taiwan. Minor in Mechanical Engineering.
2011	M.S. in Mechanical Engineering, National Taiwan University, Taipei, Taiwan.
2011-2012	Teaching Assistant, Mechanical Engineering Department, National Taiwan University, Taipei, Taiwan.

CHAPTER 1

Introduction

1.1 Obstructive Sleep Apnea

1.1.1 General Introduction

Obstructive sleep apnea (OSA) is characterized by repetitive airway partial (hypopnea) or complete (apnea) occlusion during sleep (of Sleep Medicine, 2014). The risk factors of OSA including age, obesity, gender, race and craniofacial anatomy. Excess of body weight is the strongest risk factor for OSA (Lurie, 2011). It was found that a one increase in the standard deviation difference in BMI will lead to 4 times increase in the disease prevalence (Young et al., 1993). The OSA affects about $3\% - 7\%$ for adult men and $2\% - 4\%$ for adult women in the general population (Punjabi, 2008). However, due to the unawareness of the patients, up to 83% of man and 93% of women are not clinically diagnosed (Lurie, 2011). These untreated patients may have problems like daytime sleepiness, poor work performance, and cognitive dysfunction. Moreover, the OSA may contribute to the development of hypertension (Marin et al., 2013), coronary artery disease (Valham et al., 2008), or even ischmetic stroke (Adams et al., 2007).

The occurrence of OSA is caused by the airway occlusion in nasal or pharynx during sleep due to the relaxed muscle tone. For the obstruction in pharynx, Remmers et al. found it is more likely to happen within pharyngeal segment between tip of the soft palate and glottic inlet. In other word, velopharynx and oropharynx are more collapsible regions in upper airway (see figure 1.1). The overnight polysomnography is the standard diagnostic method for the syndrome. The in-laboratory testing records the physiologic signals including

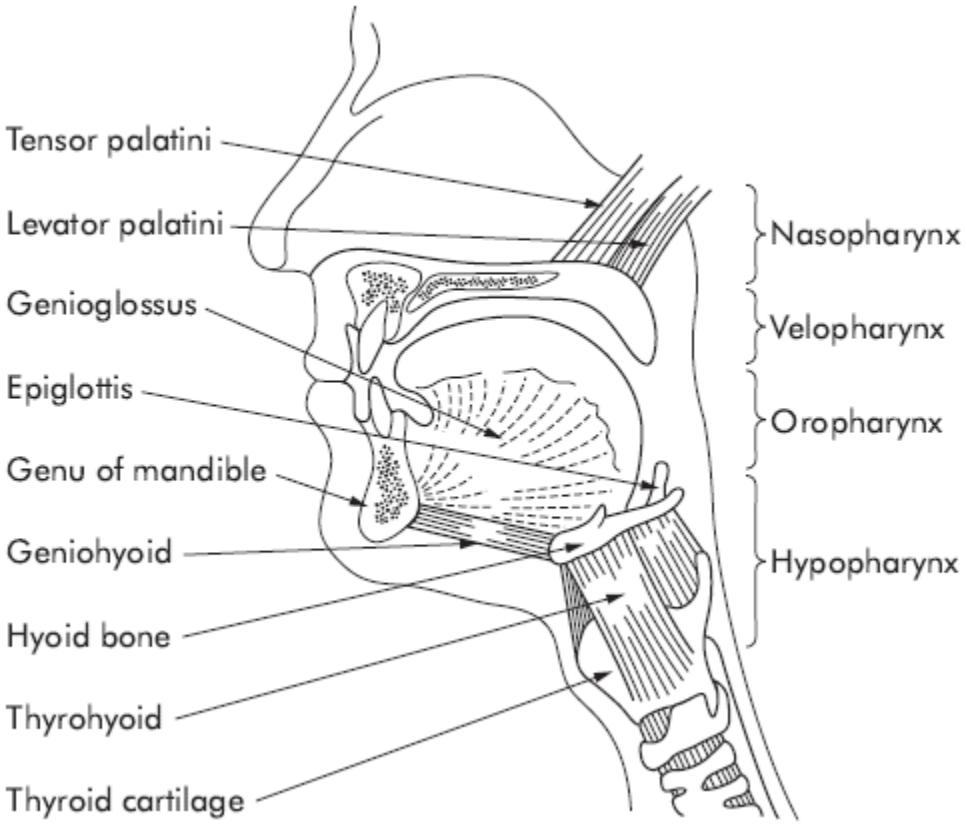

Figure 1.1: Anatomy representation of the human upper airway (Fogel et al., 2004).

electrocardiogram, electrooculogram, airflow, oxygen saturation, respiratory effort and other signals of the patients (Epstein et al., 2009). The severity of the syndrome is evaluated with the Apnea-Hypopnea Index (AHI) and Respiratory Disturbance Index (RDI). The AHI represents the number of occurrence of apnea and hypopnea per hour, where the apnea is commonly defined as when the breathing amount is less than 25% of the usually amount and the hypopnea is defined as when the breathing amount is $26\% - 69\%$ of one's normal breath (Quan et al., 1999). The RDI represents the number of airway disturbance including respiratory effort related arousal (RERA), apnea, and hypopnea, so that the value of RDI is generally larger than AHI. For adults, one is commonly considered to be OSA patient if one's AHI$>$ 5. The severity of OSA is defined as mild with 5 $\leq$RDI$<$ 15, moderate with 15 $\leq$RDI$<$ 30, and severe with RDI$>$ 30.

The Starling resistor is a classic model to understand upper airway occlusion (Gleadhill

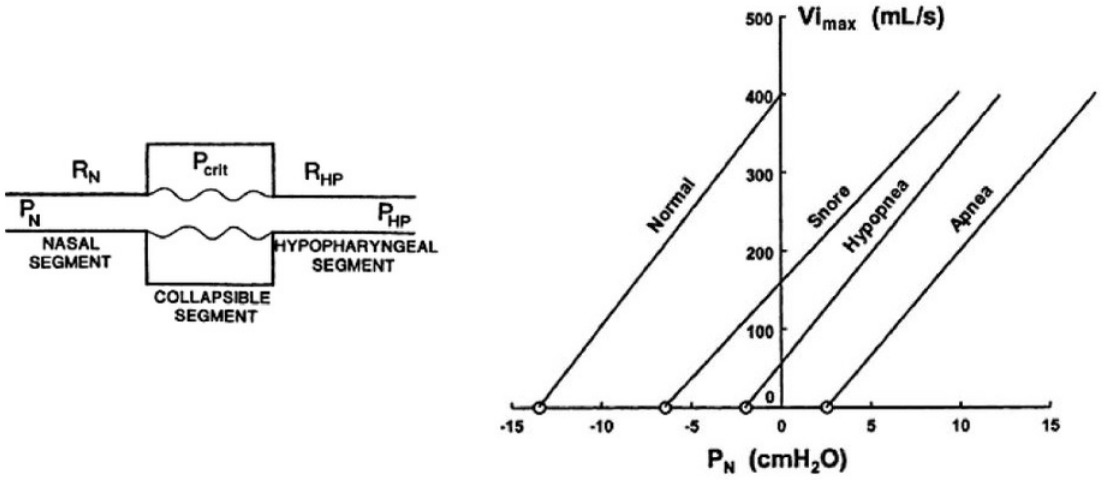

Figure 1.2: Left: the Starling resistor model by Gleadhill et al. (1991). Right: the pressure-flow relationship for different subject types.

et al., 1991; Smith et al., 1988). The pharynx is modeled as a collapsible tube to discuss the factors affecting the occurrence of the OSA (left plot in figure 1.2). The collapsible segment of the tube is surrounded with external pressure P_{crit}, and two rigid segments represent the upstream nasal and downstream hypopharygeal parts. The collapsibility can then be defined as the degree of P_{crit}. While the transmural pressure P_{crit} minus pressure in lumen is positive, this corresponds to occlusion of the airway. Smith and Schwartz (2011) measured the P_{crit} by changing the pressure in the nasal and observed the pressure-flow relationship for normals, subjects with snoring, hypopnea, and apnea as shown in the right plot in figure 1.2. The value of P_{crit} is equal to the value of nasal pressure P_N when zero airflow is reached. The normal subjects typically have $P_{crit} < -8$ $\mathrm{cmH_2O}$ and mild OSA patients have P_{crit} slightly greater then 0. This model relates the airway collapsibility to the transmural pressure. Abramson et al. summarized the factors affecting the transmural pressure and airway collapsibility in the figure 1.3.

The three-dimensional imaging techniques like computed tomographic (CT) (Abramson et al., 2010) scans and magnetic resonance imaging (MRI) (Cosentini et al., 2004; Schwab et al., 2003) have been utilized to characterize the airway anatomy of OSA patients. Abramson et al. used 3D-CT scans and showed that patients of sleep apnea usually have smaller

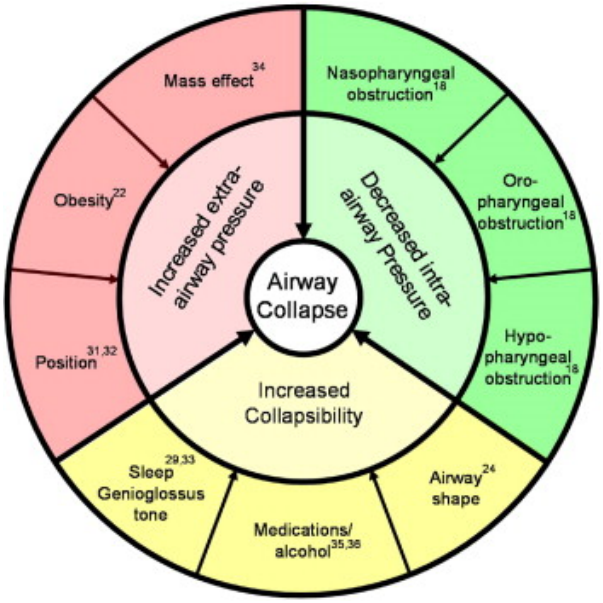

Figure 1.3: Factors that predisposed to airway collapse (summarized by Abramson et al.).

minimum cross-sectional area, longer airway, or smaller lateral dimension and anteroposterior dimension ratio. Schwab et al. utilized volumetric MRI, and larger volume of tongue, lateral pharyngeal wall, and soft tissue were found in the OSA patients. The limitation of classical CT and MRI analysis are that MRI only can obtain images that is averaged with time, and CT scans are usually obtained from awake patients. The anatomy and physiology are different from awake and sleep (Ayappa and Rapoport, 2003). The cine Magnetic resonance, or sleep MRI was utilized to observe the dynamic airway collapse and identify location and type of occlusion (Moon et al., 2010).

1.1.2 Treatment

The treatments of OSA include continuous positive airway pressure (CPAP), behavioral treatment, oral appliances (OA), and surgeries. Among all the treatments, the CPAP is the preferred one (Epstein et al., 2009). Being applied through a nasal, oral, or oronasal interface during sleep, CPAP maintains a continuous level of positive airway pressure. This maintains the airway patency by providing the sufficient internal pressure to resist the wall collapse. The use of CPAP is proven to reduce the risk of cardiovascular events (Marin et al., 2005)

and stroke (Martínez-García et al., 2009). The limitation of CPAP is the low tolerance of patient to this treatment. In 5-year follow-up study by Martínez-García et al. (2009), only 30% of patients were considered to have good long-term adherence of CPAP treatment.

Behavioral treatment (Epstein et al., 2009) options include weight loss, exercise, positional therapy. Obesity is a main risk factor for OSA and the ideal BMI should be 25 kg/m^2 or less. The positional therapy is the method to keep patient in a non-supine sleeping position to enlarge the airway size. Costume made oral appliance (OA) can enhance the airway patency by increasing the upper airway calibre Chan et al. (2010) or improving the airway muscle tone (Ferguson et al., 2006). Oral appliance is a well-tolerated treatment by patients and with about 50% of rate of success. The OA includes mandibular repositioning appliance (MRA), which hold the mandibular in an advance position, and tongue retaining devices (TRD), which prevent tongue from falling backward to the resting position.

Surgical treatments are alternative treatments when patients fail to adhere to CPAP therapy (figure 1.4). Maxillo-mandibular advancement (MMA) is a skeletal surgery to enlarge the velo-oro-hypopharyngeal airway by moving the upper jaw and lower jaw forward. Surgeries involving excision of uvula and tightening soft palate tissue include uvulopalatopharyngoplasty (UPPP), laser assisted uvulopalatoplasty (LAUP), and soft palatal implants (Caples et al., 2010). Nasal surgery improves the nasal breath by reducing the size of the turbinate and enlarging the nasal valve to reduce nasal obstruction. Sometimes multi-level simultaneous surgery, which combining different surgery in the same surgical session, or multi-level phased surgeries, which contains series of step-wise surgeries, are applied (Caples et al., 2010).

1.2 Review of Studies Focusing on Human Upper Airway

1.2.1 Experimental Research

The in-vivo experiment in upper airway is hard to conduct. In-vitro experiments by Hahn et al. (1993) and Kelly et al. (2000) were performed to observe the flow field in the human

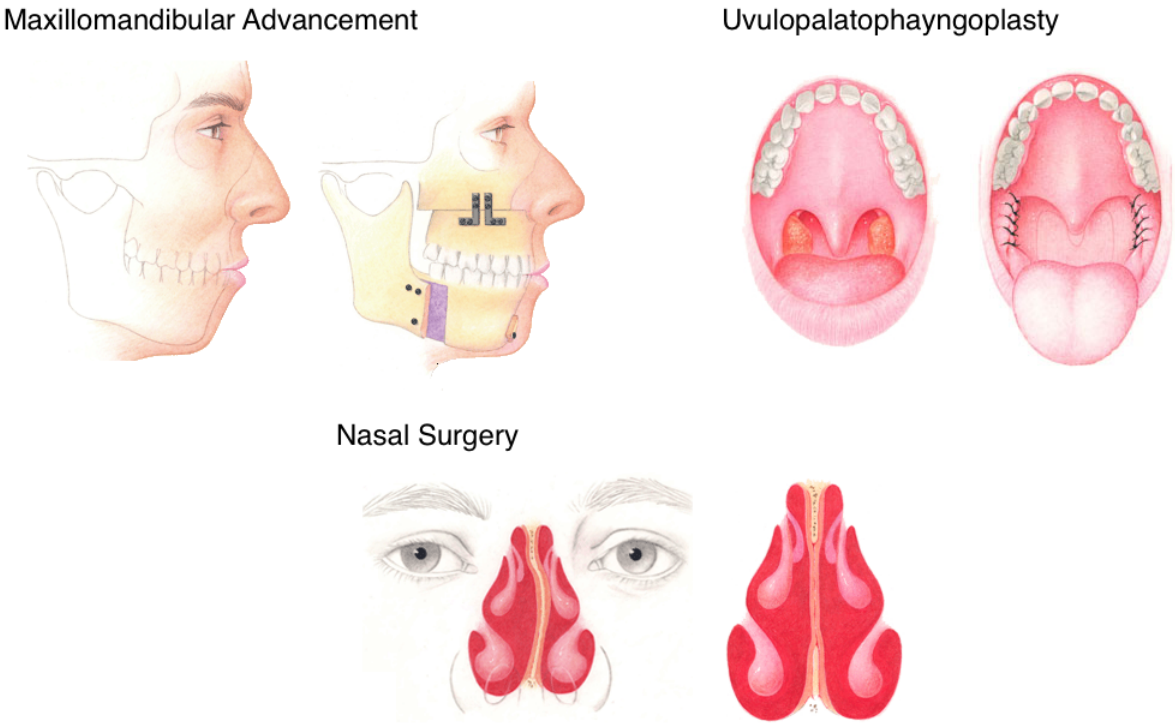

Figure 1.4: Surgical treatments of maxillomandibular advancement, uvulopalatopharyngoplasty, and nasal surgery (from www.sleepapneasurgery.com).

nasal cavity obtained from CT scans and MRI. The rigid airway models were used and steady flow rate was imposed. Kelly et al. observed laminar flow in the nasal cavity in a low steady flow rate (125 ml/s), while Hahn et al. (1993) demonstrated that the flow inside the nasal cavity was laminar for low flow rate (180 ml/s) and became turbulent for moderate (560 ml/s) and high flow rate (1,100 ml/s).

As to the in-vitro experiments for the flow in pharynx, Heenan et al. (2003) and Pollard and Shinneeb (2010) created an idealized, symmetric airway model to see the global flow behaviour. Features of jet-like flow, asymmetry, anisotropy and recirculation are developed in the air flow. Some studies used experiments results for validation and comparison with CFD simulations (Chouly et al., 2008; Xu et al., 2006; Zhao et al., 2013).

1.2.2 Theoretical Modelling

Some theoretical models were built to describe the flow and structure interaction in the airway. On top of the classic the Starling resistor model proposed by Smith et al., there are some advanced mathematical snoring models including Gavriely and Jensen (1993), Fodil et al. (1997), and Aittokallio et al. (2001) describe the dynamic response of the airway. The model by Gavriely and Jensen and Fodil et al. take the inertia of airway tissue into consideration. Gavriely and Jensen proposed spring mass model to simulate the collapsible segment in the airway to be a mass linking to a spring. The transmural pressure at the collapsible segment has component of the pressure drop due to the upper airway resistance as well as the Bernoulli effect. The force balance between spring force and the transmural pressure force governs the behavior of the mass and affects the airway width. The phase-plane plots, which show the relation of airway width and rate of change of the width, with different topology are observed under different parameters. It showed the area of the airway and gas density play an important role on the onset of snoring. Fodil et al. (1997) proposed two-element model by modeling the collapsible wall to be a series of two individualized elements with different compliant and size. On the other hand, Aittokallio et al. considered the tube with varying cross-sectional area. The proposed one-dimensional model uses averaged properties in cross-sectional direction. It resulted in the governing equations with area, flow velocity, and pressure in variables x and t. The tube law described the relation between the transmural pressure and airway area. The flow patterns of snoring and airway collapse were observed by considering different values of tube stiffness, driving pressure, and muscle tone.

Instead of modeling OSA as the collapse of tube, there exists a different view that OSA may be related with the airway blockage by the motion of the soft-palate. Balint and Lucey proposed a mechanical model of the upper airway to be the air-flow in a rigid airway channel, and a flexible plate is mounted behind an upstream rigid plate. The inlet is divided into two sections representing the inflow from the nasal and oral cavity, while the flexible thin plate represent the motion of the soft palate and uvula. The FSI studies of flow induced deformation of the flexible plate were performed with different inlet velocities and plate

heights. It was found that under the situation when one inlet is blocked, which means the flow rates from nasal and oral cavity are imbalanced, the divergence instability of the flexible plate can be observed when the flow speed in beyond a critical value. Furthermore, Cisonni et al. considered a compound flexible plate composed with two sections with different dimensions and properties representing soft palate and uvula. It is found the instability is more likely to develop with a thinner, lighter, and softer uvula.

1.2.3 Numerical Research

1.2.3.1 Rigid Wall Assumption

In several studies, simplified averaged-extra-thoracic airway geometries were created to analyze the flow field inside. Kleinstreuer and Zhang (2003) developed an idealized model with circular cross-section with constriction at larynx. The low-reynolds-number turbulence $k-\omega$ model was utilized to simulate steady laminar-to-turbulent suspension flow from mouth to trachea. The onset of turbulent after the constriction at larynx was observed. Matida et al. (2006) used idealized mouth 3D geometry, which is a average model based on literatures, to predict aerosol deposition in mouth. The LES was used for turbulence simulation and steady inhalation flow was set. It showed good agreement compared with experiment with same idealized geometry. Pollard and Shinneeb (2010) also did numerical simulations on the idealized model to make comparison between different turbulence model with experiment.

Although the simulation results showed good concordance with experiments using the idealized geometry in the in above studies, simplified airway model may not be able to reflect the true flow field in the real airway. Collins et al. (2007) compared the simulated flow fields and particle depositions in orotracheal airway using the idealized and patient-specific model obtained from MRI. The flow field in this idealized model have good agreement with results by Heenan et al. (2003) was observed due to the similar geometry. They both showed three major regions of flow recirculation as well as laryngeal jet structure. However, in the results using patient-specific airway model, neither recirculatory flow nor laryngeal jet structure

were observed. This may due to the sharp edges and the longer trachea structure in the idealized airway model. In the particle deposition simulation, the percentages of different size of particles trapped by the wall were much less than that in the patient-specific model. This research conveys the importance to used anatomically accurate airway model for airflow analysis. Also, because the airway geometry varies largely from person to person, the cause of OSA and the location of occlusion differ with patients. It is important to build patient-specific upper airway model for analysis of the occlusion of the airway.

For the studies using the three-dimensional anatomically accurate airway model, in most of the researches airway wall was considered to be rigid. The Reynolds number of the airflow in pharynx are on the order of $O(10^3)$ (about 1000 to 2700 during light breathing with flow rate 10 L/min). This implies the transition from laminar to turbulence might happen locally in airway, where the transitional flow usually occurs at Reynolds number at 2000 to 10000. However, the three-dimensional flow separation or recirculation in airway may trigger the onset of transitions to turbulence at high respiratory flow rate. The Reynolds-averaged Navier-Stokes (RANS) method have been used in several literatures.

Shome et al. (1998) chose two-equation $k-\epsilon$ model in simulation. The flow was assumed to be steady and with the uniform inlet flow velocity. The minimum intraluminal pressure was found at the location with the smallest cross-section area. The pressure drop was up to 40% larger in the turbulence flow compared with the one in laminar flow due to the high mixing ability to exchange to energy between near-wall and core flows. Xu et al. (2006) used RANS equation with low Reynolds number two-equations $k-\omega$ turbulence model with finite volume method to simulate airway of children patients from nostril to trachea on inspiration and expiration respectively. The flow was assumed to be steady while the constant pressure condition was set at nostril and uniform flow velocity was set at trachea. After comparison between results of airway subjects to OSA and normal airway, Xu et al. (2006) found the resistances in pharynx were a lot higher in children with OSA than without OSA, while the resistances in nostril are similar in both groups. The pharyngeal airway shape in children with OSA have significant influence of the internal pressure distribution.

Vos et al. (2007) simulated steady expiratory flow in upper airway of 20 OSA patients with different values of AHI. The outlet was set to be constant atmospheric pressure at nostril, while the inlet was set to be uniform velocity at larynx. The parameters including minimum cross-sectional area, resistance, pressure drop and BMI were checked. These parameters showed a linear correlation with the values of AHI. Jeong et al. (2007) used low Reynolds number two-equations $k-\epsilon$ turbulence model with finite volume method to simulate steady flow in airway from nostril to trachea of a patients with OSA obtained from CT scan. A validation test of the axisymmetric tube with sinusoidal construction showed good agreement with the velocity distribution between the $k-\epsilon$ turbulence model and experiments. The simulations were done with different inhaled flow rates, and it showed that the pressure drop and aerodynamic force increase quadratically with the increasing inhaled flow rate. The flow pattern in the pharynx demonstrated the acceleration flow (pharyngeal jet) extends at velopharynx into hypopharynx and flows along the posterior side of the airway. Jeong et al. considered the strength and flow characteristics of this pharyngeal jet would be the main reason of the airway obstruction. The force acting on the wall surface had the maximum value in the downstream region of the velopharynx, while the high shear force was observed on the posterior pharyngeal wall due to the pharyngeal jet. It was concluded in this research that the velopharynx is the most collapsible area due to the minimum intraluminal pressure and maximum aerodynamic force.

Nonetheless, RANS may not be the best choice for analysis on flow pattern in upper airway. Wilcox (1993) have found the ability of RANS to accurately predict anisotropic flows which develop adverse pressure gradient, secondary flow regions or curved streamlines is limited. In contract, the large eddy simulation (LES), which filters out and models the small scale structure, is a relatively appropriate choice to simulate flow in the upper airway. Mihaescu et al. (2008) simulated steady flow in upper airway reconstructed from MR scan with RANS $k-\omega$, $k-\epsilon$ model and LES. The results by RANS $k-\omega$ model was more close to the results by LES. However, there still existed 30% of difference in the mean axial velocities between these two models. The pharyngeal jet structure were observed in all the

turbulence models, but for the $k-\epsilon$ model only one recirculation region were observed, while two recirculation regions on posterior and anterior wall after the jet are observed using $k-\omega$ and LES models. The sizes of these two recirculation regions appeared to be similar in $k-\omega$ model, while the size of recirculation region was larger on posterior wall in LES model. Mihaescu et al. considered LES can provide an increased level of detail and accuracy for the unsteady, separated and vortical turbulent flow in upper airway.

1.2.3.2 Fluid–Structure Intersection

The unsteadiness and wall flexibility may play an important role in the airway collapse (Luo and Pedley, 1996). In the studies using rigid wall assumption, the location with lowest intraluminal pressure and maximum force on the airway wall were obtained and was claimed to be the most collapsible location. Actually, if the fluid–structure interaction is taken into consideration, it has been observed that lowest pressure may not really correspond to the location of collapse (Zhao et al., 2013). Considering interaction of the airflow with surrounding tissue provides a more realistic and accurate prediction of the occlusion location.

There are limited studies on the fluid–structure interaction in upper airway. Huang et al. (2007) considered that the fluid and structure are only weakly coupled. The patient-specific airway geometry is reconstructed from the two-dimensional MRI slices and is set to be anatomic symmetry about the midline. The flow field was computed first and the force distribution on the airway wall was obtained. This information was then load on surface of the tongue, soft palate, and uvula to calculate their deformation. For fluid, the laminar, incompressible flow was assumed and the pressure boundary conditions were imposed at inlet and outlet. For solid, the passive tongue and pharyngeal tissue were assumed to be linear elastic materials. The genioglosus, which is the dilator muscle in airway, was assumed to have nonlinear behavior under axial contraction. The closing pressure was measured when the soft palate or tongue tissue touch the posterior wall. It was observed that the closing pressure decreases after applying UPPP surgery, palatal implants, and tongue implants.

Chouly et al. (2008) utilized the strong coupling algorithm for FSI, however, a simplified

airway model was considered. The pharynx was represented by the rigid circular pipe, while the base of tongue was represented by a short deformable circular cylinder. The deformable cylinder intersected orthogonally with the rigid circular pipe. The in-vitro experiment, using the metallic rigid tube and short latex tube filled with water to represent pharynx and tongue tissue, was performed to compare with the numerical results. For the numerical model, the fluid was considered to be incompressible, laminar, and stationary, and the tissue is assumed to be linear elastic material. Chouly et al. gradually increased the external pressure, which is the pressure outside of the tongue tissue, and the decrease of the cross-sectional area was observed. A similar simplified airway model was also simulated by Mohammad Rasani et al. (2011). The tongue tissue was also assumed to be linear elasticity material, while the turbulent flow was considered for fluid using the RANS with $k-\omega$ turbulent model. The relation between pressure drop from inlet to outlet and flow rate showed the flow rate limitation phenomena. The degree of flow plateauing, which the increase of flow rate decreases with increasing pressure, decreased through raising of the constriction heigh, which corresponds to the smallest hight in the airway model. Mohammad Rasani et al.'s turbulent model predicted a more severe pressure drop in the constriction than the laminar flow model by Chouly et al.. This result is in accordance with the numerical result in Shome et al. (1998). This leads to the conclusion that the elastic wall collapse was more severe in turbulent flow model than laminar model.

The simulation of strong coupled fluid–structure interaction in patient-specific upper airway geometries were conducted in Sun et al. (2007), , Wang et al. (2012), Zhu et al. (2012a), Zhao et al. (2013), and Pirnar et al. (2015) with software ANSYS or ADINA. In all these studies, the soft tissues are governed with linear elasticity model. In most studies RANS equation was utilized as the turbulence model, except for the laminar flow assumption in Zhu et al. (2012a). Zhao et al. considered patient-specific airway geometry from hard palate to the base of epiglottis. The fluid domain is surrounded with the 2 mm thick deformable pharyngeal wall, while inspiration flow was set to be sinusoidal uniformly distributed velocity at the inlet with maximum flow rate 166 ml/s. It was observed that

the wall contact happened at the base of the tongue at flow rate 127 ml/s in the airway geometry of OSA patient. The site of occlusion does't coincide with the site with the lowest pressure, which is about 4 cm before it. However, the lowest pressure decreased the overall oropharyngeal and laryngeal pressures and induced wall occlusion in these regions. After the mandibular advancement treatment, a more uniform flow with lower flow speed and smaller transmural pressure were observed. Thus no airway obstruction occurred in the post-treatment airway.

The results in Zhao et al. (2013) suggests the importance of including fluid–structure interaction in the analysis. It shows the cite with the lowest pressure doesn't guarantee the be the location of airway collapse. Nevertheless, the assumption of uniform thickness of tissue surrounding the airway can not reflect the real situation which the collapsibility should vary along the airway. The patient-specific soft tissue geometries should be considered. Sun et al. (2007), Wang et al. (2012), and Zhu et al. (2012a) conducted simulations of the interaction between the soft palate and the airflow, where the first two studies considered steady inspiratory and expiratory flow, and the last study considered transient flow within two breathing cycles. Sun et al. used shorter airway geometries from nostril to oropharynx from a healthy person and an OSA patient. It was observed that the characteristics involving hypertrophic soft palate and narrow velopharynx lead to the rapid increase in both pressure gradient and velocity gradient as well as increment of resistance. This leads to not only larger deformation in soft palate but also larger transmural pressure in airway. Wang et al. considered airway from nostril to laryngopharynx focusing on the influences of nasal surgery. Not only the soft palate geometry was obtained from CT scans, the muscle supporting soft palate was also taken into consideration by adding the four pairs of artificial bilateral palate muscle on the basis of the anatomy of the soft palate. The material of these muscle pairs were still assumed to be linear elastic but with about 40 times stiffer than the soft palate. The comparison between flow field and displacement in airway before and after the nasal surgery showed that airway resistances has significant decrease after the surgery due to the increased volume in nasal cavity. The decrease of aerodynamic force resulted in the smaller

displacement of soft palate after the surgery. Zhu et al. (2012a) used lower Young's moduli $E = 7539$ Pa and $E = 3000$ Pa in the simulations. It was found for in the studied patient-specific airway geometry the deformation of the soft palate is larger during expiration than in inspiration.

In the simulations in Pirnar et al. (2015), all the tissues surrounding the airway at velopharynx were included. Not only the deformation of soft palate and uvula structure at anterior side of the airway, but also the soft tissue at the posterior side connecting to the supine is included. At the location where soft tissue adhering to the supine, hard palate and other bone structure, the soft tissue is set to be fixed. In other words, more realistic soft tissue structure and boundary conditions were considered. The airway starts from nostril to the trachea, and except for the velopharynx, the rest of the airway remains rigid, including the tongue. The sinusoidally-varying airflow rate is imposed with the peak flow rate 416 ml/s. The soft palate exhibited flutter behavior under the pressure variation in the respiratory flow. The flutter frequency of the soft palate is in accordance with the value reported in the previous study in palatal snoring.

In summary, several previous studies have attempted conducting the simulations of airflow-tissue interaction in patient-specific upper airway geometries. The airway narrowing and the flutter behavior soft palate have been exhibited. Also, the reduction of the airway resistance and the removal of the airway occlusion after treatment have also been demonstrated. These show the numerical analysis of the fluid–structure interaction in patient-specific airway geometries is promising for investigation of the OSA. However, there still exists some deficiencies in the numerical model adopted in the previous studies considering fluid–structure interaction. First, the physical model for the soft tissue and transitional flow may be not appropriate. The nonlinear analysis is more proper for the prediction of the motion of the soft tissue. Also, the soft tissue displays both properties of viscous and elastic materials. The viscoelastic model would be the suitable model to predict the motion of soft tissue in the respiratory flow. For the turbulence model, as discussed in the previous section, is more appropriate for the transitional flow in the upper airway. Second, the deformation

of the tongue was ignored in all the studies listed above. The area behind the tongue is also considered a common site of airway collapse, so that the deformation at the back of the tongue should not be ignored.

1.3 Objectives

This research aims to develop a numerical tool to simulate the fluid–structure interaction (FSI) in the upper airway. The ultimate gaol of this tool is expected to capture the airway occlusion with inspiratory flow in the patient-specific upper airway geometry. The airway and tissue geometries will be obtained by cone-beam CT scans, and the data can be segmented by using the software ITK-SNAP, which are used for structures segmentation of 3D medical images. The segmented data will then be converted to the signed distance function by MATLAB. For the OSA diagnosis, the polysomnography is time consuming and costly. The numerical simulation is a relatively less expensive and fast analysis technique which provides help on assess the severity of OSA. It can also provide assistant on selection the proper treatment or surgery type for specific patients. To reach the goal, this tool needs to be equipped with elements which enable accurate and efficient numerical analysis:

- **FSI**

  Most of the previous studies targeted on the flow simulation in the fixed airway. However, the collapsibility of the surrounding tissue should vary with location and the geometry. There are only limited number of studies considering FSI in the upper airway. Moreover, some studies considering FSI used simplified airway models or chose commercial CFD codes to do simulation and coupling. Our main objectives of this research is to design an in-house numerical tool dealing with FSI in human upper airway efficiently and accurately with strong coupling algorithm.

- **Patient specific geometries**

  It has been shown in the previous studies that the flow field in the simplified airway model and patient-specific airway geometries showed different flow characteristics. To

figure out the location of airway collapse and give suggestion on treatment selections, it is crucial to conduct simulations with patient-specific upper airway geometries.

- **Non-body-conformal Cartesian grid**

  Grid conformal finite element or finite volume method were used in most studies. Considering the deforming and complex boundary geometry, the time consuming grid generation and remeshing processes are the major drawbacks of the conformal grid. Instead of setting the boundary domain to be adhered with the irregular geometries, another group of solvers utilizing Cartesian grid system seem to be more suitable. We choose to use non-body-conforming grid system with immersed boundary method for fluid and cut-cell finite element method with virtual nodes for solid to avoid the cumbersome grid generation and remeshing.

- **Nonlinear elasticity**

  Most papers used linear elasticity model for tissue. However, linear elasticity model is only suitable for structure undergoing infinitesimal displacement. When a structure undergoing large rotation or deformation, the, linear elasticity model predicts the wrong strain field due to ignoring the higher order terms. This results in obtaining a wrong displacement field. The simplest nonlinear elasticity, Saint-Venant's model, will be chosen to represent the constitutive law of soft tissue. The material properties of tissues around upper airway obtained by Cheng et al. (2011) using a new magnetic resonance elastography (MRE) can be utilized.

- **Parallel computing**

  The parallel computing, which the calculations are split and distributed to multiple processing elements, can highly raise the efficiency. It is implemented by using parallel computing libraries including MPI, PETSc on distributed memory system.

CHAPTER 2

Methodology

The domain of the fluid–structure interaction system Ω can be divided into two parts: the one occupied by the solid Ω^S and another occupied by the fluid Ω^F as illustrated in plot 2.1. The superscript S denotes the solid structure, while the superscript F denotes the fluid. The union of Ω^S and Ω^F is an empty space. Γ_S and Γ_F denote the boundary of the domain Ω^S and Ω^F respectively, while Ω^{FSI} refers to the fluid–structure interaction interface between these two domains. The subscript represents the different types of the boundary. The d refers to the Dirichlet boundary type, and the n refers to the Neumann boundary type (or traction boundary type for solid).

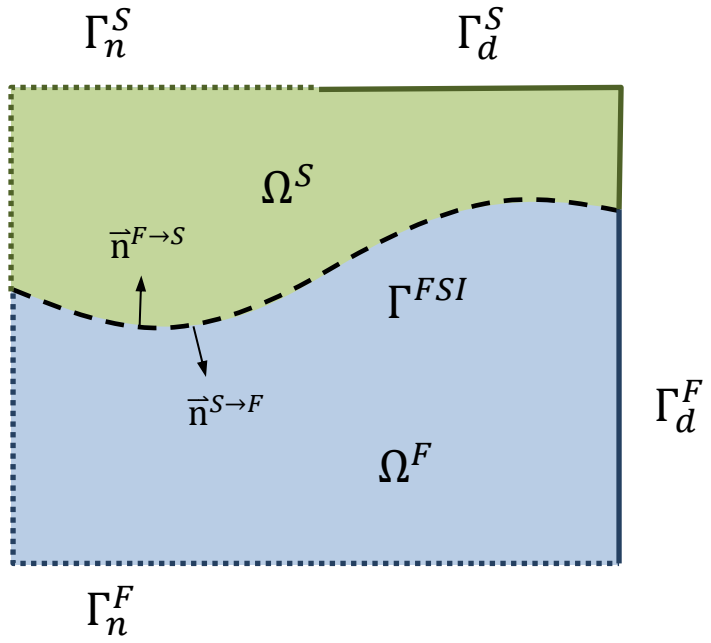

Figure 2.1: System domain of a fluid–structure interaction problem.

The solid and fluid domains are treated in different frameworks. For solid, the material (or Lagrangian) coordinates $\underline{X}$ is used to describe the positions of a solid particle in the reference state, while the spatial (or Eulerian) coordinates $\underline{x}$ describe the positions of a solid particle in the deformed or current state. The displacement field $\underline{\xi}$ of this solid particle, which is the difference between $\underline{X}$ and $\underline{x}$, can then be tracked. The deformation-gradient tensor, which is defined as $\underline{\underline{F}} \equiv \partial \underline{x}/\partial \underline{X}$, relates the deformed state and reference state, while the Jacobian, which is defined as $J \equiv \det(\partial \underline{x}/\partial \underline{X})$, is the volume change of a solid element. The naught subscript refers to the properties in the reference state, for example, ρ_0^S, b_0^S, and τ_0^S. For fluid, due to its high deformability, the Eulerian description is used. The Cartesian spatial (or Eulerian) coordinates $\underline{x}$ describe the positions of a fluid particle in the current state. The flow variables at the fixed grid points are computed.

2.1 Governing equations

For two-dimensional Newtonian and incompressible fluid, the governing momentum and continuity equations are

$$\rho^F \left(\frac{\partial \underline{u}}{\partial t} + \underline{u} \cdot \nabla \underline{u} \right) = -\nabla p + \mu^F \nabla^2 \underline{u} + \rho^F \underline{b}^F \qquad \text{in } \Omega^F \tag{2.1}$$

$$\nabla \underline{u} = 0 \qquad \text{in } \Omega^F \tag{2.2}$$

where $\underline{u}$ refers to the velocity field, p is the fluid pressure field, $\underline{f}^F$ is the external body force, and μ and ρ^F are the dynamic viscosity coefficient and density of the fluid.

For the homogeneous, isotropic, and elastic solid material, the momentum equation with respect to the current state is

$$\rho_t^S D_{tt} \underline{\xi}(\underline{x}, t) = \nabla_t \cdot \underline{\underline{\sigma}} + \rho_t^S \underline{b}_t^S \qquad \text{in } \Omega_t^S \tag{2.3}$$

where $\underline{\xi}$ is the displacement field, $\underline{\underline{\sigma}}$ is the Cauchy stress tensor, ρ^S and $\underline{b}^S$ are the density and body force, and D represents the material derivatives, which is the rate of change of the properties of a specific solid particle. The subscripts t represent the properties in the current state at time t, while double subscript tt means second derivatives in time. In order

to simulate the structure undergoing large displacement or rotation, the nonlinear analysis shall be performed. In this research, we choose to use the total Lagrangian formulation, which all the properties are with respect to the reference state. The governing equation can be rewritten as

$$\rho_0^S D_{tt}\underline{\xi}(\underline{X},t) = \nabla_0 \cdot \underline{\underline{P}} + \rho_0^S \underline{b}_0^S, \qquad \text{in } \Omega_0^S \tag{2.4}$$

where $\underline{\underline{P}}$ is the first Piola stress tensor.

The relation between stress and strain is described by the constitutive law. In the total Lagrangian formulation nonlinear analysis, the strain measure is defined by the Green-Lagrange strain tensor E,

$$E_{ij} = \frac{1}{2}\left(\frac{\partial\, \xi_i}{\partial X_j} + \frac{\partial\, \xi_j}{\partial X_i} + \frac{\partial\, \xi_k}{\partial X_i}\frac{\partial\, \xi_k}{\partial X_j}\right) \tag{2.5}$$

The diagonal elements in Green-Lagrange strain tensor represent the change in length per unit length in different direction, while the off-diagonal terms indicate change in the angle between perpendicular lines. In this research, the Saint Venant-Kirchhoff model assumes the stress is linearly related with the strain,

$$\underline{\underline{S}}(\underline{X},t) = 2\mu^S \underline{\underline{E}} + \lambda^S tr\left(\underline{\underline{E}}\right)\underline{\underline{I}}, \qquad \text{in } \Omega_0^S, \tag{2.6}$$

where $\underline{\underline{S}}$ represents the second Piola stress tensor, which is related with $\underline{\underline{P}}$ by $\underline{\underline{P}} = \underline{\underline{S}} \cdot \underline{\underline{F}}^T$. The μ^S and λ^S denote the two Lamé's coefficients of the solid, which has the relation with the Young's modulus E and poisson ratio ν,

$$E = \frac{\mu(3\lambda + 2\mu)}{\lambda + \mu}, \qquad\qquad \nu = \frac{\lambda}{2(\lambda + \mu)},$$

The Saint Venant-Kirchhoff model is the simplest hyperelastic elasticity model, which the stress-strain relation is derived from the strain energy function.

The Dirichlet and Neumann boundary conditions at the borders of solid and fluid domains

are

$$\underline{\xi} = \underline{\xi}_D, \qquad \text{on } \Gamma^S_{0v} \tag{2.7}$$

$$\underline{\underline{P}} \cdot \underline{n}_0 = \underline{\tau}^S_{N0}, \qquad \text{on } \Gamma^S_{0\tau} \tag{2.8}$$

$$\underline{u} = \underline{u}_D, \qquad \text{on } \Gamma^F_v \tag{2.9}$$

$$\underline{\underline{\sigma}} \cdot \underline{n} = \underline{\tau}^F_N, \qquad \text{on } \Gamma^F_\tau \tag{2.10}$$

where $\underline{n}_0$ and $\underline{\tau}^S_{N0}$ denotes the normal vector and traction with respect to the material coordinates. As to the boundary condition at the fluid–structure interface, the kinematic boundary condition (no-slip boundary condition),

$$\underline{u}(\underline{x}, t) = \dot{\underline{\xi}}(\underline{X}, t) \qquad \text{on } \Gamma^{FSI} \tag{2.11}$$

and the dynamic boundary condition,

$$\underline{\underline{\sigma^F}} \cdot \underline{n}^{F\to S} = -\underline{\tau} \qquad \text{on } \Gamma^{FSI} \tag{2.12}$$

$$\underline{\underline{\sigma}}^S \cdot \underline{n}^{S\to F} = \underline{\tau} \qquad \text{on } \Gamma^{FSI} \tag{2.13}$$

need to be satisfied, where the stress tensor σ^F for Newtonian fluid is defined as

$$\underline{\underline{\sigma}}^F(\underline{x}, t) = 2\mu^F \left[\nabla \underline{u}(\underline{x}, t) + (\nabla \underline{u}(\underline{x}, t))^T\right] - p^F(\underline{x}, t)\underline{\underline{I}}, \qquad \text{in } \Omega^F \tag{2.14}$$

and the σ^S is the Cauchy stress in the deformed state and can be related to the first Piola stress tensor using,

$$\underline{\underline{\sigma}}^S = J^{-1}\underline{\underline{F}} \cdot \underline{\underline{P}} \tag{2.15}$$

Non-dimensionalized governing equations

Considering the characteristic length L and the characteristic velocity U_0 in the fluid–structure interaction system, the characteristic time can thus be defined as $t_0 = L/U_0$. The coordinates $\underline{x}$, $\underline{X}$ and displacement field $\underline{\xi}$ are non-dimensionalized using L, while the velocity field in fluid is non-dimensionalized using U_0. The variables $\underline{\underline{P}}$, $\underline{\underline{S}}$, $\underline{\underline{\sigma}}$, $\underline{\tau}^S_{N0}$, μ^S and λ^S associated with structure and the variables $\underline{\underline{\sigma}}^F$, $\underline{\tau}^F_N$ and p associated with fluid have the unit

force/area. The former group of variables are non-dimensionalized using $\rho^S U_0^2$, while the latter group of variables are non-dimensionalized using $\rho^F U_0^2$. The traction at the interface $\underline{\tau}$ is chosen to be non-dimensionalized using $\rho^S U_0^2$. Also, define Reynolds number and density ratio as

$$Re = \frac{\rho^F L U_0}{\mu^F} \qquad\qquad \tilde{\rho}_0^S = \frac{\rho_0^S}{\rho^F}$$

The non-dimansionalized governing equations and boundary conditions are listed below. (The tilde representing non-dimansional variables and parameters are dropped.)

$$\frac{\partial \underline{u}}{\partial t} + \underline{u} \cdot \nabla \underline{u} = -\nabla p + \frac{1}{Re} \nabla^2 \underline{u} + \underline{b}^F \qquad \text{in } \Omega^F \tag{2.16}$$

$$\nabla \underline{u} = 0 \qquad \text{in } \Omega^F \tag{2.17}$$

$$D_{tt} \underline{\xi}(\underline{X}, t) = \nabla_0 \cdot \underline{\underline{P}} + \underline{b}_0^S, \qquad \text{in } \Omega_0^S \tag{2.18}$$

$$\underline{\underline{S}}(\underline{X}, t) = 2\mu^S \underline{\underline{E}} + \lambda^S tr\left(\underline{\underline{E}}\right) \underline{\underline{I}}, \qquad \text{in } \Omega_0^S \tag{2.19}$$

$$\underline{\underline{\sigma}} \cdot \underline{n} = \underline{\tau}_N^F \qquad \text{on } \Gamma_\tau^F \tag{2.20}$$

$$\underline{\underline{P}} \cdot \underline{n_0} = \underline{\tau}_{N0}^S \qquad \text{on } \Gamma_{0\tau}^S \tag{2.21}$$

$$\underline{u} = \underline{u}_D \qquad \text{on } \Gamma_v^F \tag{2.22}$$

$$\underline{\xi} = \underline{\xi}_D \qquad \text{on } \Gamma_{0v}^S \tag{2.23}$$

$$\underline{\underline{\sigma}} \cdot \underline{n}^{F \to S} = -\rho_0^S \, \underline{\tau} \qquad \text{on } \Gamma^{FSI} \tag{2.24}$$

$$\underline{\underline{\sigma}}^S \cdot \underline{n}^{S \to F} = \underline{\tau} \qquad \text{on } \Gamma^{FSI} \tag{2.25}$$

$$\underline{u}(\underline{x}, t) = \dot{\underline{\xi}}(\underline{X}, t) \qquad \text{on } \Gamma^{FSI} \tag{2.26}$$

2.2 Fluid Solver

2.2.1 Introduction

The immersed boundary method pioneered by Peskin (1972) has wide applications. The governing equations are discretized on Cartesian grid system and the immersed boundary

is not conformal to grid points. The boundary conditions are imposed indirectly. A body-force field or forcing term is introduced in the momentum equation to represent effect of the immersed boundary. The non-body-conformal feature makes immersed boundary method suitable for dealing with moving immersed boundaries. It eliminates the cumbersome body-conformal-grid generation process and no grid transformation is needed.

The imposition of boundary condition is an important issue in IB algorithm. The forcing approach can be classified into two categories: continuous and discrete forcing approaches (Mittal and Iaccarino, 2005). For continuous forcing approach, the forcing term is introduces into the continuous governing equation. The governing equation is then discretized on Cartesian grid and solved in the entire domain. Peskin (1972) first simulated flow through natural heart valve. The elastic boundary is tracked by a set of points linked by springs and the stresses the boundary produces are transmitted to the fluid through Dirac delta function. Goldstein et al. (1993) introduced the feedback forcing to simulate the flow over rigid bodies. The forcing makes boundary acts like a damped oscillator when the boundary velocities deviate from the enforced velocities. These approaches using continuous forcing are not ideal approaches for simulating flow at high Reynolds number. Firstly, the smooth discretized Dirac delta function smears the influence of the sharp boundary so that the accuracy in the thin boundary layer decreases in flow at high Reynold number. Secondly, stability problem may rise when rigid or stiff body is simulated.

For the discrete forcing approach, the governing equation without effect of boundary is discretized on Cartesian grid first and forcing terms are imposed on the discrete governing system of equations. For finite volume method, boundary cells are cut by boundary and the part in fluid is merged with neighboring cell (Ye et al., 1999). The fluxes on the faces of these boundary cells are evaluated by interpolation using the flow properties at neighboring nodes in fluid. For finite difference method, Majumdar et al. (2001) reconstructed the flow variables at ghost cells, which are the solid nodes having at least one neighbor in fluid, so that through interpolation the boundary conditions on the boundary are satisfied. Majumdar et al. employed interpolant which is quadratic in the direction normal to boundary and

linear in tangential direction. Similarly, Mohd-Yusof (1997) and Fadlun et al. (2000) applied forcing to reconstruct flow variables at selected set of nodes. Mohd-Yusof applied forcing at ghost nodes and Fadlun et al. tried to add forcing at different sets of nodes with different interpolation schemes. Fadlun et al. showed choosing the fluid nodes closest to boundary as the forcing points with reconstruction their flow variables using linear interpolation had the best performance with second order of accuracy. The flow variables at forcing points were linear interpolated using velocities at nearest boundary points and fluid nodes along horizontal or vertical grid lines. However, the ambiguity of which direction to perform interpolation appears for complex boundary geometry. Balaras (2004) then proposed to do linear interpolation along the direction normal to boundary surface. To have a more compact interpolation stencil, Yang and Balaras (2006) developed a triangular stencil to do two-dimensional bilinear interpolation using one boundary point and two fluid nodes. The discrete forcing approaches mentioned above treat the boundary as sharp interface without using smooth distribution function. Also, no use of stability constraints is needed and governing equations need only to be solved in fluid domain. These features make discrete forcing approach more desirable for simulation at high Re number.

For transitional and turbulent flows, their small spatial and temporal scale require very fine grid and time step. Using direct numerical simulation (DNS), which solves Navier-Stokes equation without modeling, is very time consuming. The Reynolds-averaged Navier-Stokes equation (RANS) solves the averaged flow variables in time and needs model of the Reynolds stress. However, it is not suitable for anisotropic flows with secondary flow region or curved streamlines (Wilcox, 1993). In large eddy simulation (LES), a spatial filter is used to compute large-scale quantity and subgrid-scale (SGS) stress is modeled. Smagorinsky (1963) modeled eddy viscosity to be proportional to and magnitude of local large-scale strain rate tensor with a universal constant coefficient. This commonly used model is more desirable for isotropic turbulence and need modification near wall. Germano et al. (1991) proposed dynamic model to use two different widths of spatial filter to calculate the local coefficient in eddy viscosity. This model is less *ad hoc* in determining eddy viscosity and no modification is needed near

wall.

2.2.2 Numerical Methodology

The non-body-conforming Cartesian grid with immersed-boundary method proposed by Yang and Balaras (2006) is used to simulate the airflow in airway. The projection method is employed to solve the governing equations (2.1), (2.2) (Chorin, 1968; Kim and Moin, 1985). For spatial discretization, central difference method to discretize velocity and pressure field on the MAC staggered grid are used (figure 2.2). The time advancement is achieved using third-order Runge-Kutta scheme. For both convection and viscous term, the explicit Adam-Bashforth scheme is used. Rather than using implicit scheme for viscous terms, it was found in previous studies that implicit scheme for viscous terms didn't have obvious gains in the time step (Balaras, 2004). The use of explicit scheme greatly simplifies the imposition of boundary condition. The momentum equation then becomes

$$\frac{\hat{u}_i^k - u_i^{k-1}}{\Delta t} = \gamma_k H(u_i^{k-1}) + \rho_k H(u_i^{k-2}) - \alpha_k \frac{\partial p^{k-1}}{\partial x_i} + f_i^k, \tag{2.27}$$

where H is an operator containing convection and viscous terms,

$$H(u_i^n) \equiv -\frac{\partial u_i^n u_j^n}{\partial x_j} + \frac{1}{Re}\frac{\partial^2 u_i^n}{\partial x_j \partial x_j},$$

and k refers to substep index of RK method, and the values of α, γ, ρ are listed in table 2.1. The intermediate velocities $\hat{u}_i^k$ are first computed and boundary conditions at domain boundary are imposed. Then projection method is employed to obtain the divergence free velocity field u_i^k,

$$\nabla^2 \delta p = \frac{1}{\Delta t}\frac{\partial \hat{u}_i^k}{\partial x_i}, \tag{2.28}$$

$$u_i^k = \hat{u}_i^k - \Delta t \nabla \delta p, \tag{2.29}$$

$$p^k = p^{k-1} + \delta p. \tag{2.30}$$

For the immersed body in the fluid with non-conformal grid system, the boundary conditions at the interface are satisfied by adding forcing term f_i on the forcing points. The

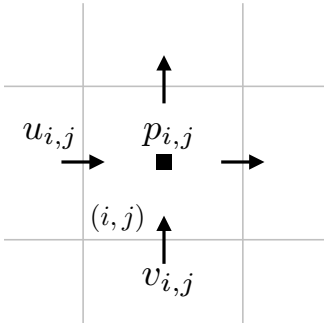

Figure 2.2: The MAC stagger grid for fluid in two-dimension.

forcing points are defined as grid points with at least one neighboring grid points in the structure. The value of f_i is set to let the velocities on the forcing point to be u_f, which means

$$f_i^k = \frac{u_f - u_i^{k-1}}{\Delta t} - \gamma_k H(u_i^{k-1}) - \rho_k H(u_i^{k-2}) + \alpha_k \frac{\partial p^{k-1}}{\partial x_i}. \tag{2.31}$$

For most cases, the forcing point will not be located right at the interface. The u_f will be obtained from linear interpolation of velocities at the interface and on nearby fluid nodes. In figure 2.3 two examples of the compact triangular interpolation stencil proposed by Yang and Balaras (2006) are shown. The point 1 is the associated interface point of this forcing point with its normal line passes the forcing point, and point 2 and 3 are nearby fluid nodes. The interface is defined by the Eulerian implicit signed distance function, which is a special case of the level set function. The value of the signed distance function represents the distance from each grid point to the nearest surface, while the sign of it shows if the grid point is inside (positive) or outside (negative). The advantage of using the implicit interface representation for the immersed method is the simplicity of indentifying the fluid points and the forcing points.

Table 2.1: Coefficients used in momentum equation (2.27)

k	1	2	3
a	8/15	2/15	1/3
g	8/15	5/12	3/4
r	0	-17/60	-5/12

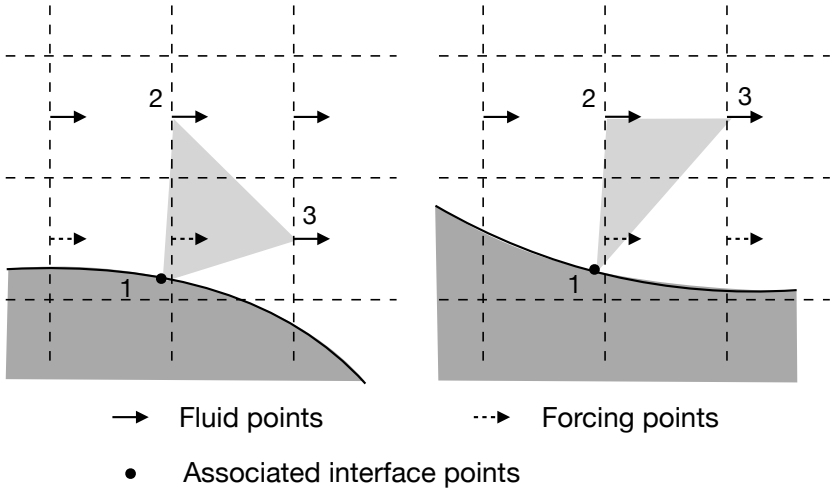

Figure 2.3: Two examples of the interpolation stencils for forcing points.

The flow field in the stencil can be obtained through linear interpolation, which is

$$\phi = b_0 + b_1 x + b_2 y + b_3 z. \tag{2.32}$$

, where ϕ represent the flow variables. The variable on the forcing points can be reconstructed from the updated variables at nearby fluid points and interface,

$$\phi_f = \begin{bmatrix} 1 & x_f & y_f & z_f \end{bmatrix} \begin{bmatrix} b_0 \\ b_1 \\ b_2 \\ b_3 \end{bmatrix} = \begin{bmatrix} 1 & x_f & y_f & z_f \end{bmatrix} \begin{bmatrix} 1 & x_0 & y_0 & z_0 \\ 1 & x_1 & y_1 & z_1 \\ 1 & x_2 & y_2 & z_2 \\ 1 & x_3 & y_3 & z_3 \end{bmatrix}^{-1} \begin{bmatrix} \phi_1 \\ \phi_2 \\ \phi_3 \\ \phi_4 \end{bmatrix} \tag{2.33}$$

The choice of stencil differs with the interface geometries and the orientation of it's local normal direction. To maintain accuracy, usually only the fluid points within one grid size away in each directions can be selected as interpolation stencils. Considering the two-dimensional case, if the forcing point (i, j) is associated with the interface normal vector pointing upright, fluid nodes $(i+1, j)$ and $(i, j+1)$ are naturally chosen to be the other two stencils, like in the left plot in figure 2.3. In other case, if one of $(i+1, j)$ or $(i, j+1)$ node is also a forcing point, as in the right plot in figure 2.3, nodes $(i+1, j)$ and $(i+1, j+1)$ are chosen instead.

With this interpolation stencil, it takes two (in 2D) or three (in 3D) nearby fluid points to reconstruct flow field near interface. However in some cases, especially with very irregular

interface geometries, there are insufficient number of fluid nodes that meet the criteria (the right plot in figure 2.4). This is considered as a degenerate case, and the triangular or tetrahedron stencils are not applicable. Instead of bilinear or trilinear interpolation, the field reconstruction is achieved by the inverse distance weighted average of the field on nearby available fluid nodes and the associated interface point.

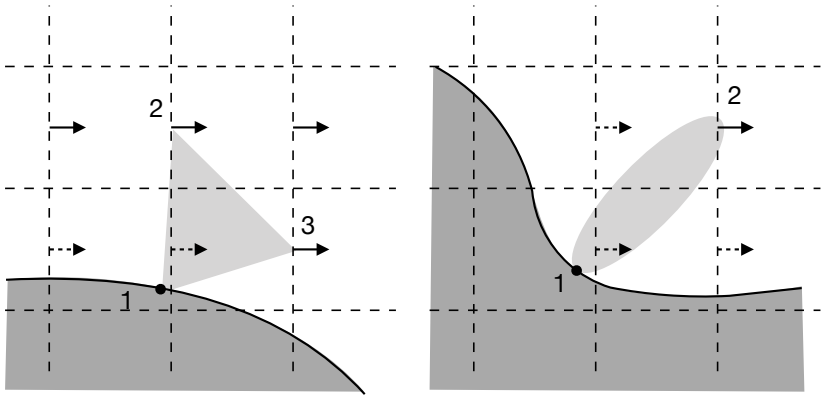

Figure 2.4: Left: normal triangular stencil. Right: degenerate case.

Treatment Due to Moving Boundary

For moving interface geometry undergoing large deformation, scenarios of grid points change from solid to fluid or fluid to solid may happen. These nodes are called flag-changing points. Considering a fluid point being a solid point at the previous time step, it doesn't contain the appropriate flow property information at the previous time step needed in the Runge-Kutta temporal advancement scheme. Yang and Balaras (2006) mentioned a field extension treatment to extend flow field into solid within one grid distance by extrapolation at end of every time step. The extrapolation sometimes produces extreme large value of flow properties due to the extrapolation. To solve this problem, we labelled these flag-changing pressure grids at beginning of every time step. Similar to the interpolation stencil for forcing points, the pressure values at the current time step on the flag-changing points are also computed by bilinear interpolation.

Force Calculation

The force exerted on the interface by the flow plays an important role in fluid–structure interaction. Lai and Peskin (2000) has discussed different ways to compute resultant force on boundary. Yang and Balaras (2006) proposed force calculation algorithm based on reconstruction stencil mentioned in section 2.2.2. The traction exerted on the interface has the form:

$$t_i = \tau_{ij} n_j = \left[-p\delta_{ij} + \mu \left(\frac{\partial u_i}{\partial x_j} + \frac{\partial u_j}{\partial x_i} \right) \right] n_j. \tag{2.34}$$

The derivatives on velocity can be computed using the bilinear or trilinear interpolation mentioned in the previous section, and are directly related to b_1, b_2 and b_3,

$$\frac{\partial \phi}{\partial x} = b_1, \qquad \frac{\partial \phi}{\partial y} = b_2, \qquad \frac{\partial \phi}{\partial z} = b_3.$$

The pressure on the interface cannot be obtained directly from interpolation. However, the pressure gradient can be evaluated by projecting the momentum equation on interface along the normal vector $\vec{n}$ and ignoring contribution of viscous terms. The pressure gradient along the normal vector,

$$\frac{\partial p}{\partial \vec{n}} \approx -\frac{D\vec{u}}{Dt} \cdot \vec{n} \Big)_{boundary}. \tag{2.35}$$

So the pressure on interface p_b can be obtained through trilinear relation using the gradient on boundary and pressure on three fluid nodes,

$$p_b = \begin{bmatrix} 1 & x_b & y_b & z_b \end{bmatrix} \begin{bmatrix} b_0 \\ b_1 \\ b_2 \\ b_3 \end{bmatrix} = \begin{bmatrix} 1 & x_b & y_b & y_z \end{bmatrix} \begin{bmatrix} 0 & n_x & n_y & n_z \\ 1 & x_2 & y_2 & z_2 \\ 1 & x_3 & y_3 & z_3 \\ 1 & x_4 & y_4 & z_4 \end{bmatrix}^{-1} \begin{bmatrix} \partial p/\partial \vec{n} \\ p_2 \\ p_3 \\ p_4 \end{bmatrix} \tag{2.36}$$

where n_x, n_y, n_z denote the component of the unit normal vector on boundary. The pressure and velocity gradients will be obtained on the center of the triangular elements (called simplices), which represent the discretization of the interface surface.

2.3 Solid Solver

2.3.1 Introduction

Finite element method, first used by Hrennikoff (1941), is a commonly used and powerful method to solve differential equations with boundary value problems. The governing equations are solved in weak form and variational method is used to obtain the approximation solutions. In the structural problems, the approximation solutions can either choose the function to minimized the total energy or to have minimum error compared to the exact solution. Its capability to discretize weak form governing equation on unstructured grid system makes it suitable for dealing with complex boundary geometry. However, cumbersome grid generation and time consuming remeshing processes are the main drawbacks of using unstructured elements.

Embedded techniques deal with problems using non-body-conformal grid system. Some embedded techniques tackling with incompressible material are introduced below. In fictitious domain method by Saulev (1963), irregular domain was extended to the whole regular domain and impose boundary condition through Lagrange multiplier. Glowinski et al. (1999) dealt with particulate flow which is viscous incompressible flow with suspended particles. The irregular fluid domain was extended to a simpler extended domain by enforce the rigid body motion in the particle domain. By combining the equation of motion in particle domain and fluid domain, the weak form equations of motion for the extended domain were be obtained. The rigid body assumption was then be relaxed to impose it in a weak sense using Lagrange multiplier.

The immersed boundary method introduced in the fluid part is also an example for using embedded method in incompressible material. Ng et al. (2009) added a discrete forcing in the discretized momentum equation as the influence of the boundary. The ghost nodes were utilized to satisfy the Dirichlet boundary condition at the boundary. Extended finite element method (XFEM) is capable to modeling the material with arbitrary crack geometry (Daux

et al., 2000). The crack was modeled independently of the regular mesh system. The shape function of the displacement field was enriched by the step function to represent the crack discontinuity and the asymptotic near-tip field representing the branched cracks. Daux et al. successfully demonstrated simulation of material with cracks of multiple branches. This method can also deal with problems containing voids or cracks emanating from holes. Bijelonja et al. (2006) used cut-cell finite volume method on the incompressible material. Zhu et al. (2012b) has the similar cut cell method in finite element method. Shape functions are cut by the boundary and the part outside of the solid domain is disregarded. Virtual nodes, which located outside of solid domain but having shape function inside the solid domain, was introduced.

2.3.2 Numerical Methodology

For the nonlinear analysis, the total Lagrangian nonlinear finite element formulation is sued following the framework by Bathe (2006). This solver aims to deal with different complex geometries without element generation. The cut-cell treatment by Zhu et al. (2012b) is incorporated in the solver. The domain will be decomposed into non-body-conformal Cartesian grids. The structure shape is described by level set function. Those elements that are cut by the boundary undergo integration only within the cut polyhedronal (or polygonal in 2D) region.

2.3.2.1 Formulation of Nonlinear Finite Element Analysis

When it comes to the numerical solution of the governing equation, the variational formulation provides the advantage of reduction of the order of continuity needed for approximated solution than dealing with the PDE directly. In solid mechanics, the variational formulation with the principle of virtual displacement states that the total internal work should be equal to the total external work,

$$\int {}^{t+\Delta t}S_{ij} \left(\delta\, {}^{t+\Delta t}E_{ij}\right) dV_0 = {}^{t+\Delta t}\mathcal{R}, \tag{2.37}$$

where $\mathcal{R}$ represents the external virtual work. The super script t on the left denotes the configuration at time t, which is the current state, and Δt represents the time stepping size. Unlike in section 2.1 the configuration at time t was represented in the subscript on the right, in the following sections it will be moved to the superscript to the left for readability.

The equation (2.37) is a nonlinear equation in terms of the displacement. The displacement is not assumed to be infinitesimal, so that the second order terms can not be ignored. To linearized the governing equation, the stress and strain are decomposed into two parts: the value obtained at the end of previous step and an incremental value,

$$^{t+\Delta t}S_{ij} = {}^{t}S_{ij} + S_{ij} \tag{2.38}$$

$$^{t+\Delta t}E_{ij} = {}^{t}E_{ij} + E_{ij}. \tag{2.39}$$

Furthermore, the incremental strain can be decomposed into linear and nonlinear parts:

$$E_{ij} = e_{ij} + \eta_{ij} \tag{2.40}$$

$$e_{ij} = \frac{1}{2}\left(\frac{\partial \xi_i}{\partial X_j} + \frac{\partial \xi_j}{\partial X_i} + \frac{\partial\, {}^{t}\xi_k}{\partial X_i}\frac{\partial \xi_k}{\partial X_j} + \frac{\partial \xi_k}{\partial X_i}\frac{\partial\, {}^{t}\xi_k}{\partial X_j}\right) \tag{2.41}$$

$$\eta_{ij} = \frac{\partial \xi_k}{\partial X_i}\frac{\partial \xi_k}{\partial X_j} \tag{2.42}$$

where the displacement $^{t+\Delta t}\xi_i = {}^{t}\xi_i + \xi_i$. At the current time, the deformed configuration are known. Those incremental stress, strain and displacement at next step are the unknowns to be solved for. After the incremental decomposition, governing equation (2.37) becomes

$$\int {}^{t+\Delta t}S_{ij}\delta\, {}^{t+\Delta t}\epsilon_{ij} dV_0 = \int S_{ij}\delta\epsilon_{ij} dV_0 + \int {}^{t}S_{ij}\left(\delta e_{ij} + \delta\eta_{ij}\right) dV_0 \tag{2.43}$$

With the Saint Venant-Kirchhoff model, the constitutive law can be written as $S_{ij} = C_{ijrs}E_{rs}$. The equation (2.43) becomes

$$\int {}^{t+\Delta t}S_{ij}\delta\, {}^{t+\Delta t}E_{ij} dV_0 = \int C_{ijrs}E_{rs}\delta E_{ij} dV_0 + \int {}^{t}S_{ij}\delta e_{ij} dV_0 + \int {}^{t}S_{ij}\delta\eta_{ij} dV_0 \tag{2.44}$$

The governing equation is still nonlinear in terms of displacement. The nonlinear term $E_{rs}\delta E_{ij}$ term can be approximated and linearized to $e_{rs}\delta e_{ij}$. The linear governing equation turns into

$$\int C_{ijrs}e_{rs}\delta e_{ij} dV_0 + \int {}^{t}S_{ij}\delta\eta_{ij} dV_0 \approx {}^{t+\Delta t}\mathcal{R} - \int {}^{t}S_{ij}\delta e_{ij} dV_0 \tag{2.45}$$

Due to the linearization approximation, the discrepancies between the internal and external virtual work has been introduced. The iteration is necessary to reduce the "out-of-balance" of virtual work,

$$\int C_{ijrs}\Delta e_{rs}^{(k)}\delta e_{ij}dV_0 + \int {}^{t+\Delta t}S_{ij}^{(k-1)}\delta\Delta\eta_{ij}^{(k)}dV_0 = {}^{t+\Delta t}\mathcal{R} - \int {}^{t+\Delta t}S_{ij}^{(k-1)}\delta\ {}^{t+\Delta t}e_{ij}^{(k-1)}dV_0, \tag{2.46}$$

where the sign Δ represents the difference of variables between previous and current iteration, meaning ${}^{t+\Delta t}\xi_i^{(k)} = {}^{t+\Delta t}\xi_i^{(k-1)} + \Delta\xi_i^{(k)}$.

The (2.46) describes the linearized governing equation at the static equilibrium. For dynamics problems, the work by inertia forces can be introduced using the d' Alembert's principle on the external work term.

$$\begin{aligned}\int C_{ijrs}\Delta e_{rs}^{(k)}\delta e_{ij}dV_0 + \int {}^{t+\Delta t}S_{ij}^{(k-1)}\delta\Delta\eta_{ij}^{(k)}dV_0 = {}^{t+\Delta t}\mathcal{R} \\ - \int {}^{t+\Delta t}\ddot{\xi}_i^{(k)}\delta\xi_i dV_0 - \int {}^{t+\Delta t}S_{ij}^{(k-1)}\delta\ {}^{t+\Delta t}e_{ij}^{(k-1)}dV_0,\end{aligned} \tag{2.47}$$

After moving the inertia term to the left hand side, the left hand side of the equation contains terms linearly related to the displacement field, while the right hand side has terms associated with the discrepancies between the external and internal work in the previous iteration.

$$\begin{aligned}\int {}^{t+\Delta t}\ddot{\xi}_i^{(k)}\delta\xi_i dV_0 + \int C_{ijrs}\Delta e_{rs}^{(k)}\delta e_{ij}dV_0 + \int {}^{t+\Delta t}S_{ij}^{(k-1)}\delta\Delta\eta_{ij}^{(k)}dV_0 \\ = {}^{t+\Delta t}\mathcal{R} - \int {}^{t+\Delta t}S_{ij}^{(k-1)}\delta\ {}^{t+\Delta t}e_{ij}^{(k-1)}dV_0,\end{aligned} \tag{2.48}$$

2.3.2.2 Discretization

The above variational formulations are discretized on a MAC staggered grid system as in the fluid solver shown in figure 2.5. The grid spacing h is uniform. In the following section, the superscript will represent the component of a variable, and the subscript will represent the I$^{\text{th}}$ involved element which has influence within the solid boundary. If an involved x-displacement node ξ_I^x resides on the the grid (i, j, k), it is located at $(ih, jh + 1/2h, kh + 1/2h)$. The y-displacement node ξ_J^y and the z-displacement node on the same grid are at $(ih + 1/2h, jh, kh + 1/2h)$ and $(ih + 1/2h, jh + 1/2h, kh)$ respectively..

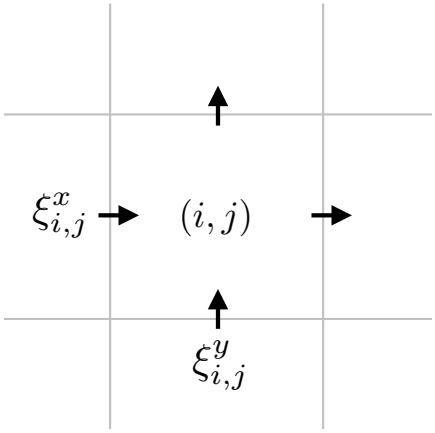

Figure 2.5: Staggered grid system (two-dimensional).

The displacement field, $\underline{\xi}\,(\underline{X},t)$, is discretized into the superposition of the piecewise trilinear shape functions multiply with the associated nodal values:

$$\begin{aligned}\underline{\xi}(\underline{X},t) &= \xi^x(\underline{X},t)\underline{e}_x + \xi^y(\underline{X},t)\underline{e}_y + \xi^z(\underline{X},t)\underline{e}_z \\ &= \sum_I \xi^x_I(t)N^{\xi x}_I(\underline{X})\underline{e}_x + \sum_J \xi^y_J(t)N^{\xi y}_J(\underline{X})\underline{e}_y + \sum_K \xi^z_K(t)N^{\xi z}_K(\underline{X})\underline{e}_z\end{aligned} \tag{2.49}$$

The $N^{\xi x}_I(\underline{X})$, $N^{\xi y}_J(\underline{X})$ and $N^{\xi z}_K(\underline{X})$ denote the shape function for x-, y- and z-displacements. The shape function associated with displacement ξ^x_I, ξ^y_J, and ξ^z_K is defined as a piecewise trilinear function in the cubic area centered at locations of ξ^x_I, ξ^y_J, and ξ^z_K with width $2h$. In other words, $N^{\xi x}_I(\underline{X})$ has nonzero value in $[ih-h, ih+h]\times[jh-1/2h, jh+3/2h]\times[kh-1/2h, kh+3/2h]$. Similarly, $N^{\xi y}_J(\underline{X})$ and $N^{\xi z}_K(\underline{X})$ have nonzero value in $[ih-1/2h, ih+3/2h]\times[jh-h, jh+h]\times[kh-1/2h, kh+3/2h]$ and $[ih-1/2h, ih+3/2h]\times[jh-1/2h, jh+3/2h]\times[kh-h, kh+h]$. These shape functions have value unity at the center and decreases to zero at the boundary of cubic area (as shown in the figure 2.6). However, not all the shape function has intersection with the domain occupied by solid Ω^S. Only the shape functions which has non-empty intersection with Ω^S are considered. There are scenarios that some nodes outside of the solid domain still have the shape function partially inside the domain. These nodes are called 'virtual nodes', and they are at most with distance h away from the solid domain. In the variational form of governing formulation, the volume integration (or, in two-dimension, area integration) are only applied in the Ω^S domain. This implies

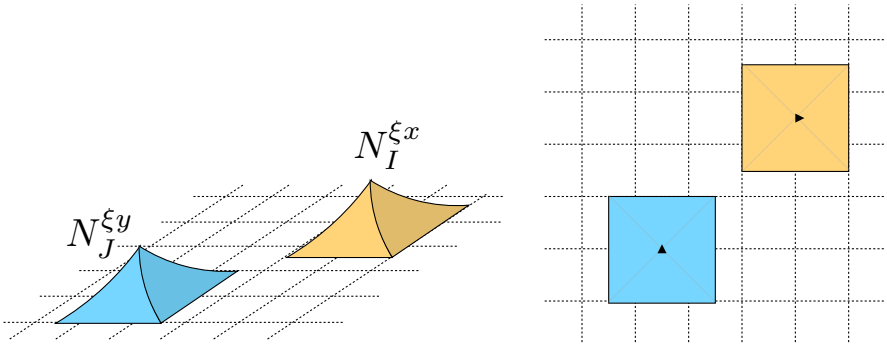

Figure 2.6: Side view (left) and the top view (right) of the shape functions of the displacement field in two-dimensional, which are piecewise bilinear functions.

there exists some 'cut-cells' that are partially inside the solid domain. The part of the shape functions being outside of solid domain will be disregarded.

As to the traction, $\underline{\tau}_D(\underline{X},t)$, $\underline{\tau}_N(\underline{X},t)$, $\underline{\tau}_F(\underline{X},t)$ denote the traction exerted on the Dirichlet, Neumann and FSI boundary respectively. The traction field are discretized into the superposition of the piecewise constant shape functions with the associated nodal values:

$$\underline{\tau}^D(\underline{X},t) = \sum_I \tau_I^{Dx}(t) N_I^{\tau Dx}(\underline{X})\underline{e}_x + \sum_J \tau_J^{Dy}(t) N_J^{\tau Dy}(\underline{X})\underline{e}_y + \sum_K \tau_K^{Dz}(t) N_K^{\tau Dz}(\underline{X})\underline{e}_z \quad (2.50)$$

$$\underline{\tau}^N(\underline{X},t) = \sum_I \tau_I^{Nx}(t) N_I^{\tau Nx}(\underline{X})\underline{e}_x + \sum_J \tau_J^{Ny}(t) N_J^{\tau Ny}(\underline{X})\underline{e}_y + \sum_K \tau_K^{Nz}(t) N_K^{\tau Nz}(\underline{X})\underline{e}_z \quad (2.51)$$

$$\underline{\tau}^F(\underline{X},t) = \sum_I \tau_I^{Fx}(t) N_I^{\tau Fx}(\underline{X})\underline{e}_x + \sum_J \tau_J^{Fy}(t) N_J^{\tau Fy}(\underline{X})\underline{e}_y + \sum_K \tau_K^{Fz}(t) N_K^{\tau Fz}(\underline{X})\underline{e}_z \quad (2.52)$$

The piecewise constant shape function is defined in the cubic area which has left corner at the location of ξ_I^x, ξ_J^y, and ξ_K^z with width h as shown in figure 2.7. The traction terms are associated with the integration along the solid boundary, so only the elements having intersection with Γ^S and Γ^{FSI} are considered. This is equivalent to treat the traction on boundary as a piecewise constant function along the solid boundary.

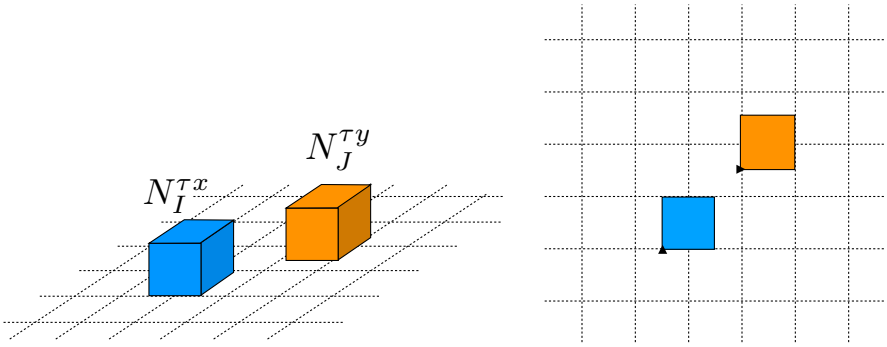

Figure 2.7: Side view (left) and the top view (right) of the shape functions of the displacement field in two-dimensional, which are piecewise bilinear functions.

2.3.2.3 System of Equations

After the discretizing the displacement and traction field into superposition of shape functions, the original functional in the weak form can be transformed into a function with nodal displacement and traction. The involved nodal displacement in each direction can be rearranged into vectors:

$$\underline{\hat{\xi}}_x \equiv \begin{bmatrix} \xi_1^x \\ \xi_2^x \\ \vdots \\ \xi_{n_x}^x \end{bmatrix}, \ \underline{\hat{\xi}}_y \equiv \begin{bmatrix} \xi_1^y \\ \xi_2^y \\ \vdots \\ \xi_{n_y}^y \end{bmatrix}, \ \underline{\hat{\xi}}_z \equiv \begin{bmatrix} \xi_1^z \\ \xi_2^z \\ \vdots \\ \xi_{n_z}^z \end{bmatrix}, \tag{2.53}$$

where n_x, n_y, n_z are the number of total involved nodal points in each component. And $\hat{\xi}$ vector denotes the involved nodal displacement in all directions:

$$\underline{\hat{\xi}} \equiv \begin{bmatrix} \hat{\xi}_x \\ \hat{\xi}_y \\ \hat{\xi}_z \end{bmatrix}. \tag{2.54}$$

The corresponding displacement shape function can also be written as:

$$\underline{h}_x \equiv \begin{bmatrix} N_1^{\xi x} \\ N_2^{\xi x} \\ \vdots \\ N_{n_x}^{\xi x} \end{bmatrix}, \ \underline{h}_y \equiv \begin{bmatrix} N_1^{\xi y} \\ N_2^{\xi y} \\ \vdots \\ N_{n_y}^{\xi y} \end{bmatrix}, \ \underline{h}_z \equiv \begin{bmatrix} N_1^{\xi z} \\ N_2^{\xi z} \\ \vdots \\ N_{n_z}^{\xi z} \end{bmatrix}, \tag{2.55}$$

Now the discretized displacement field can be written as

$$\underline{\xi} = \begin{bmatrix} \xi_x \\ \xi_y \\ \xi_z \end{bmatrix} = \begin{bmatrix} \underline{h}_x^T & & \\ & \underline{h}_y^T & \\ & & \underline{h}_z^T \end{bmatrix} \cdot \begin{bmatrix} \hat{\underline{\xi}}_x \\ \hat{\underline{\xi}}_y \\ \hat{\underline{\xi}}_z \end{bmatrix} \equiv \underline{\underline{H}} \cdot \hat{\underline{\xi}}, \tag{2.56}$$

where $\underline{\underline{H}}$ can be viewed as the trilinear displacement interpolation matrices. Similarly, the virtual displacement field can be shown as

$$\delta\underline{\xi} = \underline{\underline{H}} \cdot \delta\hat{\underline{\xi}}, \tag{2.57}$$

The linear part of the incremental strain tensor has 6 independent components. It can

be related with the displacement vector:

$$
\begin{aligned}
e_{ij} = \begin{Bmatrix} e_{11} \\ e_{22} \\ e_{33} \\ 2e_{12} \\ 2e_{23} \\ 2e_{13} \end{Bmatrix} &= \begin{bmatrix} \underline{h}^T_{x,x} & & \\ & \underline{h}^T_{y,y} & \\ & & \underline{h}^T_{y,y} \\ \underline{h}^T_{x,y} & \underline{h}^T_{y,x} & \\ & \underline{h}^T_{y,z} & \underline{h}^T_{z,y} \\ \underline{h}^T_{x,z} & & \underline{h}^T_{z,x} \end{bmatrix} \cdot \begin{Bmatrix} \hat{\underline{\xi}}_x \\ \hat{\underline{\xi}}_y \\ \hat{\underline{\xi}}_z \end{Bmatrix} \\
&+ \begin{bmatrix} & {}^t u_{x,x}\underline{h}^T_{x,x} & & {}^t u_{y,x}\underline{h}^T_{y,x} & & {}^t u_{z,x}\underline{h}^T_{z,x} \\ & {}^t u_{x,y}\underline{h}^T_{x,y} & & {}^t u_{y,y}\underline{h}^T_{y,y} & & {}^t u_{z,y}\underline{h}^T_{z,y} \\ & {}^t u_{x,z}\underline{h}^T_{x,z} & & {}^t u_{y,z}\underline{h}^T_{y,z} & & {}^t u_{z,z}\underline{h}^T_{z,z} \\ {}^t u_{x,x}\underline{h}^T_{x,y} + & {}^t u_{x,y}\underline{h}^T_{x,x} & {}^t u_{y,x}\underline{h}^T_{y,y} + & {}^t u_{y,y}\underline{h}^T_{y,x} & {}^t u_{z,x}\underline{h}^T_{z,y} + & {}^t u_{z,y}\underline{h}^T_{z,x} \\ {}^t u_{x,y}\underline{h}^T_{x,z} + & {}^t u_{x,z}\underline{h}^T_{x,y} & {}^t u_{y,z}\underline{h}^T_{y,y} + & {}^t u_{y,y}\underline{h}^T_{y,z} & {}^t u_{z,z}\underline{h}^T_{z,y} + & {}^t u_{z,y}\underline{h}^T_{z,z} \\ {}^t u_{x,x}\underline{h}^T_{x,z} + & {}^t u_{x,z}\underline{h}^T_{x,x} & {}^t u_{y,x}\underline{h}^T_{y,z} + & {}^t u_{y,z}\underline{h}^T_{y,x} & {}^t u_{z,x}\underline{h}^T_{z,z} + & {}^t u_{z,z}\underline{h}^T_{z,x} \end{bmatrix} \cdot \begin{Bmatrix} \hat{\underline{\xi}}_x \\ \hat{\underline{\xi}}_y \\ \hat{\underline{\xi}}_z \end{Bmatrix} \\
&\equiv {}^t\underline{\underline{B}}_L \cdot \hat{\underline{\xi}}
\end{aligned}
\tag{2.58}
$$

where $\underline{\underline{B}}_L$ is the linear strain-displacement transformation matrix. The $\underline{\underline{B}}_L$ matrix is varying with time. The superscript t on the left represents the matrix is calculated from the displacement gradient field at time t. On the other hand, the internal virtual work by the

nonlinear part of the incremental strain tensor can be written as

$$
{}^{t}S_{ij}\delta\eta_{ij} = \left\{ \delta\hat{\underline{\xi}}_{x}^{T} \quad \delta\hat{\underline{\xi}}_{y}^{T} \quad \delta\hat{\underline{\xi}}_{z}^{T} \right\} \cdot \begin{bmatrix} \underline{h}_{x,x} & \underline{h}_{x,y} & \underline{h}_{x,z} & & & & & & \\ & & & \underline{h}_{y,x} & \underline{h}_{y,y} & \underline{h}_{y,z} & & & \\ & & & & & & \underline{h}_{z,x} & \underline{h}_{z,y} & \underline{h}_{z,z} \end{bmatrix} \tag{2.59}
$$

$$
\begin{bmatrix} {}^{t}\underline{\underline{S}} & & \\ & {}^{t}\underline{\underline{S}} & \\ & & {}^{t}\underline{\underline{S}} \end{bmatrix} \cdot \begin{bmatrix} \underline{h}_{x,x}^{T} & & \\ \underline{h}_{x,y}^{T} & & \\ \underline{h}_{x,z}^{T} & & \\ & \underline{h}_{y,x}^{T} & \\ & \underline{h}_{y,y}^{T} & \\ & \underline{h}_{y,z}^{T} & \\ & & \underline{h}_{z,x}^{T} \\ & & \underline{h}_{z,y}^{T} \\ & & \underline{h}_{z,z}^{T} \end{bmatrix} \begin{Bmatrix} \hat{\underline{\xi}}_{x} \\ \hat{\underline{\xi}}_{y} \\ \hat{\underline{\xi}}_{z} \end{Bmatrix} \equiv \delta\hat{\underline{\xi}}^{T}\, \underline{\underline{B}}_{NL}^{T}\, {}^{t}\underline{\underline{S}}\, \underline{\underline{B}}_{NL}\hat{\underline{\xi}}
$$

where $\underline{\underline{B}}_{NL}$ is the nonlinear strain-displacement transformation matrix and the stress tensor ${}^{t}\underline{\underline{S}}$ means

$$
{}^{t}\underline{\underline{S}} \equiv \begin{bmatrix} {}^{t}S_{11} & {}^{t}S_{12} & {}^{t}S_{13} \\ {}^{t}S_{21} & {}^{t}S_{22} & {}^{t}S_{23} \\ {}^{t}S_{31} & {}^{t}S_{32} & {}^{t}S_{33} \end{bmatrix} \tag{2.60}
$$

The external virtual work ${}^{t+\Delta t}\mathcal{R}$ relates to the displacement and the traction exerted on the solid boundary

$$
{}^{t+\Delta t}\mathcal{R} = \int \left({}^{t+\Delta t}\tau_{i}^{D} + {}^{t+\Delta t}\tau_{i}^{N} + {}^{t+\Delta t}\tau_{i}^{F} \right) \delta\xi_{i} dS_{0}. \tag{2.61}
$$

Similar to the derivation in the previous section, the traction field can be written as the inner product between the nodal stresses vector $\hat{\underline{\tau}}$ and the piecewise constant interpolation matrix $\underline{\underline{T}}$:

$$
\underline{\tau}^{D} = \underline{\underline{T}}^{D} \cdot \hat{\underline{\tau}}^{D} \tag{2.62}
$$

$$
\underline{\tau}^{N} = \underline{\underline{T}}^{N} \cdot \hat{\underline{\tau}}^{N} \tag{2.63}
$$

$$
\underline{\tau}^{F} = \underline{\underline{T}}^{F} \cdot \hat{\underline{\tau}}^{F} \tag{2.64}
$$

After the discretization, the governing equation (2.49) becomes

$$\begin{aligned}
&\int \delta\hat{\underline{\xi}}^T \underline{\underline{H}}^T \, \underline{\underline{H}} \, {}^{t+\Delta t}\hat{\ddot{\underline{\xi}}}^{(k)} dV_0 + \int \delta\hat{\underline{\xi}}^T \, {}^{t+\Delta t}\underline{\underline{B}}_L^{(k-1)T} \underline{\underline{C}} \, {}^{t+\Delta t}\underline{\underline{B}}_L^{(k-1)} \Delta\hat{\underline{\xi}}^{(k)} dV_0 \\
&+ \int \delta\hat{\underline{\xi}}^T \underline{\underline{B}}_{NL}^T \, {}^{t+\Delta t}\underline{\underline{S}}^{(k-1)} \underline{\underline{B}}_{NL} \Delta\hat{\underline{\xi}}^{(k)} dV_0 \\
&= \int \delta\hat{\underline{\xi}}^T \underline{\underline{H}}^T \left(\underline{\underline{T}}^D \hat{\underline{\tau}}^D + \underline{\underline{T}}^N \hat{\underline{\tau}}^N + \underline{\underline{T}}^F \hat{\underline{\tau}}^F \right) dS_0 + \int \delta\hat{\underline{\xi}}^T \, {}^{t+\Delta t}\underline{\underline{B}}_L^{(k-1)T} \, {}^{t+\Delta t}\underline{\underline{S}}^{(k-1)} \, dV_0
\end{aligned} \tag{2.65}$$

The term $\delta\hat{\underline{\xi}}^T$ can be factored out. Also, the nodal displacements and tractions can be taken out of the the volume or surface integral. The variational form of governing equation has been transformed into a system of linear algebraic equations:

$$\underline{\underline{M}} \, {}^{t+\Delta t}\hat{\ddot{\underline{\xi}}}^{(k)} + \left({}^{t+\Delta t}\underline{\underline{K}}_L^{(k-1)} + {}^{t+\Delta t}\underline{\underline{K}}_{NL}^{(k-1)} \right) \Delta\hat{\underline{\xi}}^{(k)} = \underline{\underline{D}}^s \hat{\underline{\tau}}^D + \underline{\underline{N}}^s \hat{\underline{\tau}}^N + \underline{\underline{F}}^s \hat{\underline{\tau}}^F - {}^{t+\Delta t}\underline{F}^{(k-1)}, \tag{2.66}$$

and the displacement iteration

$${}^{t+\Delta t}\hat{\underline{\xi}}^{(k)} = {}^{t+\Delta t}\hat{\underline{\xi}}^{(k-1)} + \Delta\hat{\underline{\xi}}^{(k)}. \tag{2.67}$$

The $\underline{\underline{M}}$ is the mass matrix, $\underline{\underline{K}}_L$ and $\underline{\underline{K}}_{NL}$ are the linear and nonlinear incremental stiffness matrices, and $\underline{\mathrm{F}}$ is the force vector due to the internal stress at previous iteration or step. $\underline{\underline{D}}^s$, $\underline{\underline{N}}^s$, and $\underline{\underline{F}}^s$ are the traction matrices associated with the traction exerted on the Dirichlet, Neumann and FSI boundary.

$$\underline{\underline{M}} = \int \underline{\underline{H}}^T \underline{\underline{H}} dV_0 \tag{2.68}$$

$$\underline{\underline{K}}_L = \int \underline{\underline{B}}_L^T \, \underline{\underline{C}} \, \underline{\underline{B}}_L dV_0 \tag{2.69}$$

$$\underline{\underline{K}}_{NL} = \int \underline{\underline{B}}_{NL}^T \, \underline{\underline{S}} \, \underline{\underline{B}}_{NL} dV_0 \tag{2.70}$$

$$\underline{F} = \int \underline{\underline{B}}_L^T \, \underline{\underline{S}} dV_0 \tag{2.71}$$

$$\underline{\underline{D}}^s = \int \underline{\underline{H}}^T \underline{\underline{T}}^D dS_0 \tag{2.72}$$

$$\underline{\underline{N}}^s = \int \underline{\underline{H}}^T \underline{\underline{T}}^N dS_0 \tag{2.73}$$

$$\underline{\underline{F}}^s = \int \underline{\underline{H}}^T \underline{\underline{T}}^F dS_0 \tag{2.74}$$

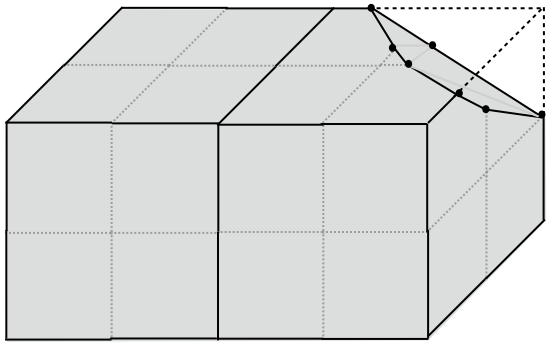

Figure 2.8: Doubly refined grid system for cut-cell integration.

For the Dirichlet boundary condition, the weak time-derivative formulation is imposed

$$\underline{\underline{D}}^{sT\ t+\Delta t}\dot{\underline{\xi}}^{(k)} = \underline{\underline{D}}^{sT}\ \dot{\underline{\xi}}_D. \tag{2.75}$$

2.3.2.4 Cut-Cell Treatment

If the cell is cut by the interface, it is not straight forward to do integration over an irregular volume or surface mentioned above. Min and Gibou (2007) proposed a systematic way to decompose the domain into a set of tetrahedron, and decompose the surface into a set of triangular elements with given level set function describing the geometry. This way of geometric integration over irregular domain has been utilized and modified to solve elliptic problems by Hellrung et al. (2012). Every cubic grid cell is divided into 8 doubly refined grids with size $h/2$, as shown in figure 2.8 (Zhu et al., 2012b). The volume integral in the governing equation is the sum of the volume integral computed in all the involved doubly refined grids inside the solid domain.

To systematically decompose the cubic grids into tetrahedron and discretize the surface into triangles, Min and Gibou suggested to decompose a grid cell into several tetrahedra first. Firstly, the cross section between a flat surface and any tetrahedron can be either a triangle and a quadrilateral as shown in the figure 2.9. A quadrilateral can be easily divided into two triangles. Secondly, there are limited scenarios of the outcome shape of polyhedron after

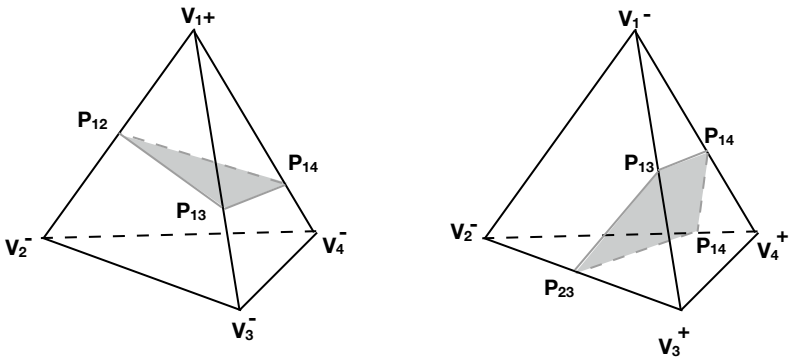

Figure 2.9: Two scenarios of the obtained triangle and quadrilateral cross section between a surface and a tetrahedron. V denotes the vertex of the tetrahedron and P is the intersection points. The sign + or - next to the vertex represent the sign of the signed distance function on that point.

cutting the tetrahedron by a flat surface. The faces of the cut polyhedron will be triangles or/and quadrilaterals.

There are various ways to perform triangulation. The cube can be divided into 5 tetrahedra (middle cut triangulation), 6 tetrahedra (Kuhn triangulation) or even 24 tetrahedra or more. Considering the computation efficiency, middle cut triangulation is performed on each doubly refined grid shown in figure 2.10. There exists two different orientations of the middle cut triangulation as plotted on the left in figure 2.11. In order to match the triangulations between the neighboring doubly refined grids, we use both two orientations of the middle cut triangulation in a staggered manner as shown on the right in figure 2.11. In other wards, in each grid cell, there will be totally 40 tetrahedra after the triangulation.

As to the calculation of the surface integral, given the level set function describing the surface geometry, the signed distance values on the vertices of a tetrahedron can be obtained. From the signed distance values on the vertices, it can be determined whether the tetrahedra is completely inside, completely outside or partially inside. If a tetrahedra is partially inside, the approximated intersection point P_{ij} can be calculated with linear interpolation by

$$P_{ij} = \frac{V_j \phi(V_i)}{\phi(V_i) - \phi(V_j)} - \frac{V_i \phi(V_j)}{\phi(V_i) - \phi(V_j)}, \tag{2.76}$$

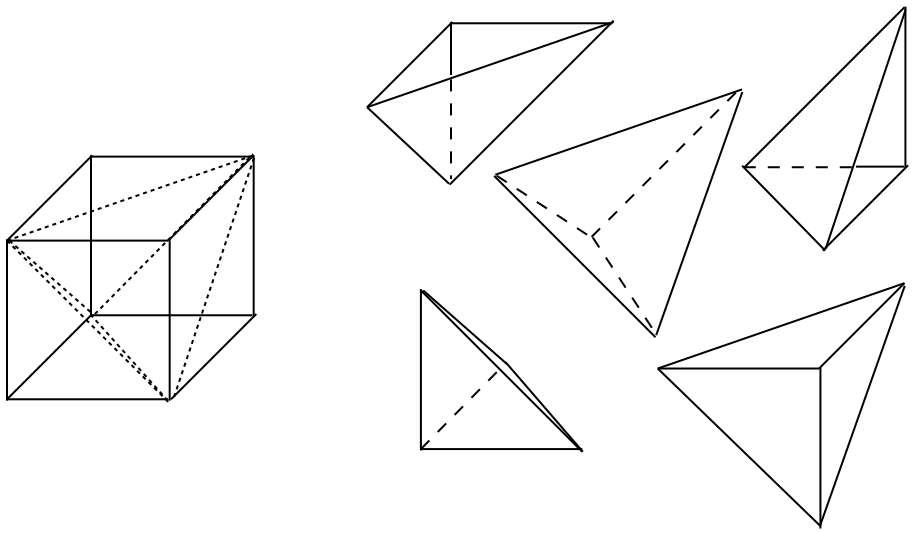

Figure 2.10: The middle cut triangulation.

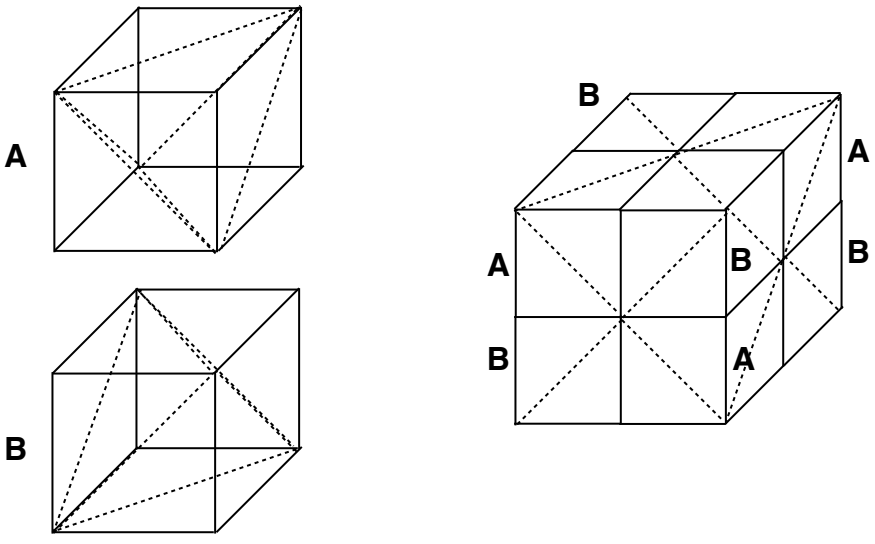

Figure 2.11: Left: two orientations of the middle cut triangulation. Right: the staggered arrangement of the triangulation A and B in one grid cell.

with the fact that the signed distance function represents the nearest distance from one point to the surface. If 3 intersection points are obtained, the surface integral on this triangle cross section can be computed using the seventh-order twelve-points Gaussian quardrature for the triangle (Dunavant, 1985). On the other hand, if there are 4 intersection points, this quadrilateral cross section will then be decomposed into two triangles, and the surface integral can be obtained with the same Gaussian quardrature rule.

As to the volume integral, after removing the part of the tetrahedron outside of the surface, the remaining part can be either a tetrahedron or a pentahedron listed in the figure 2.12. The obtained pentahedron will have three quadrilateral faces and two triangular faces. Since the integrand functions in the governing equation are in the form of polynomial, the volume integral can be transformed to surface integral using the divergence theorem (Hellrung et al., 2012),

$$\int_{\Omega} x^p y^q z^r \; dV = \int_{\Omega} \nabla \cdot (x^p y^q z^r, 0, 0) \; dV = \int_{\partial\Omega} \nabla \cdot (x^{p+1} y^q z^r, 0, 0) \cdot \underline{n} \; dS. \tag{2.77}$$

The surface integral on the faces of the tetrahedron or pentahedron can then be computed with Gaussian quardrature rule.

2.3.2.5 Time Marching Scheme

The governing matrix contains not only variables of displacement, but also first and second order of derivative of the displacement. The Newmark method by Newmark (1959) relates the variable $X(t)$ and its first and second time derivative using the relation

$$\frac{\dot{X}^{n+1} - \dot{X}^n}{\Delta t} = \delta \; \ddot{X}^{n+1} + (1 - \delta) \; \ddot{X}^n \tag{2.78}$$

$$\frac{\left(\dfrac{X^{n+1} - X^n}{\Delta t}\right) - \dot{X}^n}{\Delta t/2} = 2\theta \ddot{X}^{n+1} + (1 - 2\theta)\ddot{X}^n, \tag{2.79}$$

where subscripts n and $n+1$ refer to the approximation of any variable X at time $n\Delta t$ and $(n+1)\Delta t$ respectively.

There are two adjustable parameters δ and θ. The parameter $\delta \in [0, 1]$ relates to the stability, convergence and accuracy of the system,

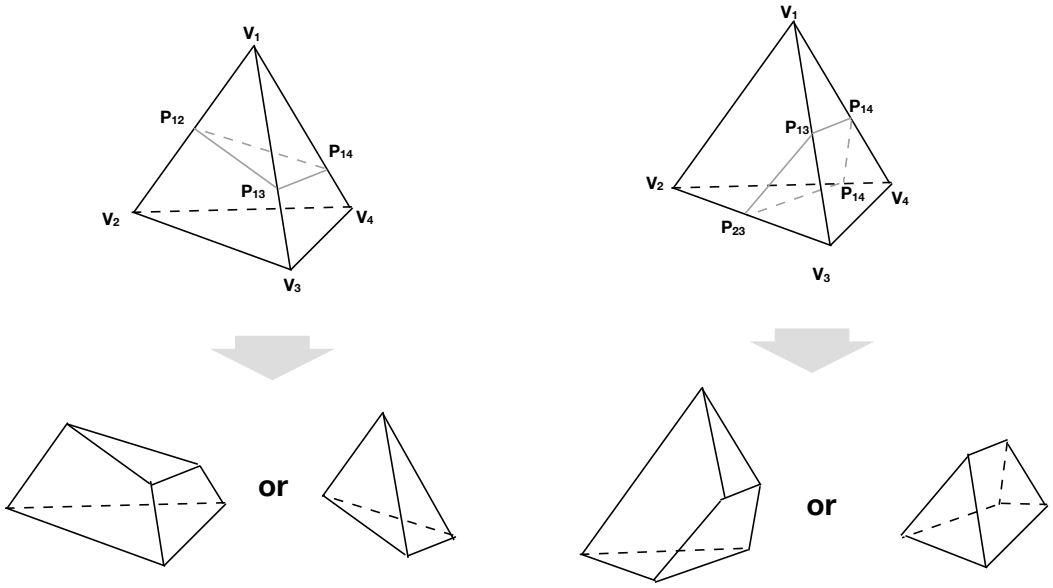

Figure 2.12: The polygon generated after dividing a tetrahedron with a flat surface. The resultant polygon can be either tetrahedron or pentahedron.

- $\delta < \frac{1}{2}$ leads to an unstable system
- $\delta = \frac{1}{2}$ leads to the accurate 2^{nd} order θ-scheme
- $\delta > \frac{1}{2}$ leads to a robust, but dissipative, 1^{st} order scheme

The value of δ is set to be $\frac{1}{2}$ to reach the highest order of accuracy. With this set-up, the parameter $\theta \in [0, 1/2]$ influences the system in the following way:

- $\theta < \frac{\delta}{2} = \frac{1}{4}$ leads to a conditionally stable system
  - $\theta = 0$ is the explicit scheme
  - $\theta = 1/12$ leads to the 4^{th} order Fox-Goodwin scheme
  - $\theta = 1/6$ leads to the linear-acceleration scheme
- $\theta \geq \frac{\delta}{2} = \frac{1}{4}$ leads to an unconditionally stable system
  - $\theta = 1/4$ is the constant-average-acceleration or trapezoidal scheme

The Newmark coefficients δ and θ are set as follow to obtain an unconditionally stable 2^{nd} order scheme.

$$\delta = \frac{1}{2} \qquad\qquad \theta = \frac{1}{4} \tag{2.80}$$

Using the Newmark method, the accelerations and the displacements can be written in term of velocities and the known variables in the previous steps or iteration.

$$ {}^{t+\Delta t}\ddot{\xi}^{(k)} = \frac{{}^{t+\Delta t}\dot{\xi}^{(k-1)} + \Delta\dot{\xi}^{(k)} - {}^{t}\dot{\xi}}{\Delta t\delta} - \frac{1-\delta}{\delta}\ {}^{t}\ddot{\xi} \tag{2.81}$$

$$\begin{aligned} \Delta\xi^{(k)} = {}& {}^{t}\xi - {}^{t+\Delta t}\xi^{(k)} + \Delta t\left(\frac{\theta}{\delta}\dot{\xi}^{(k-1)} + \frac{\delta-\theta}{\delta}\ {}^{t}\dot{\xi}\right) \\ & + \Delta t^2\left(\frac{1}{2} - \frac{\theta}{\delta}\right)\ {}^{t}\ddot{\xi} + \frac{\Delta t\theta}{\delta}\Delta\dot{\xi}^{(k)} \end{aligned} \tag{2.82}$$

These reduces the unknown variables in the governing linear system into $\Delta\dot{\xi}^{(k)}$. The system of equations for the solid material then has the form

$$\begin{bmatrix} \mathbb{M} & D^s \\ D^{s\ T} & 0 \end{bmatrix} \begin{bmatrix} \Delta\dot{\xi}^{(k)} \\ \tau^D \end{bmatrix} = \begin{bmatrix} \mathrm{RHS}_\xi \\ \mathrm{RHS}_\tau \end{bmatrix} \tag{2.83}$$

where the submatrices after applying Newmark scheme are

$$\underline{\underline{\mathbb{M}}} = \frac{\theta\Delta t}{\delta}\left({}^{t+\Delta t}\underline{\underline{K}}_L^{k-1} + {}^{t+\Delta t}\underline{\underline{K}}_{NL}^{k-1}\right) + \frac{1}{\delta\Delta t}\ \underline{\underline{M}} \tag{2.84}$$

$$\begin{aligned} \mathrm{RHS}_\xi = {}& \underline{\underline{D}}^s\underline{\hat{\tau}}^D + \underline{\underline{N}}^s\underline{\hat{\tau}}^N + \underline{\underline{F}}^s\underline{\hat{\tau}}^F - {}^{t+\Delta t}\underline{F}^{(k-1)} \\ & - \underline{\underline{M}}\left(\frac{{}^{t+\Delta t}\underline{\dot{\xi}}^{(k-1)} - {}^{t}\underline{\dot{\xi}}}{\Delta t\ \delta} - \frac{1-\delta}{\delta}\ {}^{t}\underline{\ddot{\xi}}\right) \\ & - \left({}^{t+\Delta t}\underline{\underline{K}}_L^{k-1} + {}^{t+\Delta t}\underline{\underline{K}}_{NL}^{k-1}\right)\left[{}^{t}\underline{\xi} - {}^{t+\Delta t}\underline{\xi}^{(k)} + \Delta t\left(\frac{\theta}{\delta}\ \underline{\dot{\xi}}^{(k-1)} + \frac{\delta-\theta}{\delta}\ {}^{t}\underline{\dot{\xi}}\right)\right. \\ & \left. + \Delta t^2\left(\frac{1}{2} - \frac{\theta}{\delta}\right)\ {}^{t}\underline{\ddot{\xi}} + \frac{\Delta t\ \theta}{\delta}\Delta\underline{\dot{\xi}}^{(k)}\right] \end{aligned} \tag{2.85}$$

$$\mathrm{RHS}_\tau = \underline{\underline{D}}^{s\ T}\underline{\dot{\xi}}_D \tag{2.86}$$

The governing system of equations (2.83) is ill-conditioned. One treatment proposed by Zhu et al. (2012b) using the null-space of D^s can transform the governing equations into a well-conditioned system.

The elastic pressure and shear waves develop in the elastic material without dissipation. In some cases, artificial damping is needed to filter out some high-frequency elastic waves. For this purpose, in the discretized equation, a damping term $\underline{\underline{C}}_d \, {}^{t+\Delta t}\dot{\underline{\xi}}$ will be added into the governing equation (2.66), where $\underline{\underline{C}}_d$ is a damping matrix to be determined by the Rayleigh damping, which is the mass- and stiffness- proportional damping (Bathe, 2006). The damping matrix is defined as

$$\underline{\underline{C}}_d = \alpha \underline{\underline{M}} + \beta \underline{\underline{K}}_L, \tag{2.87}$$

where α and β are scalar constants. The α and β are obtained according to the eigenvalues defined by

$$\underline{\underline{K}}_L \phi = \omega_i^2 \underline{\underline{M}}_L \phi \tag{2.88}$$

where ϕ is the eigenvectors. The ω_i refers to the frequency of the ith vibration mode. With the mode superposition analysis on the governing equation with damping, it becomes

$$\alpha + \beta \omega_i^2 = 2\omega_i \xi_i \tag{2.89}$$

where ξ_i refers to the exponentially damping rate related to the elastic wave with vibration frequency ω_i. The appropriate α and β can be calculated by choosing the desired damping ratio for two target vibration modes.

2.4 Interface

The flow field and structure deformation field are solved by separate solvers alternatively and iteratively. Only the motion and the traction at the interface need to be exchanged between these two solvers. Although the signed distance function on grid points is already defined in the fluid and solid solvers, this implicit description of the interface may not be helpful on the information exchanged between two domains. The Lagrangian interface elements are introduced in order to build the mapping between the corresponding grids in fluid and structure solvers.

The interface is decomposed into a union of Lagrangian triangle elements, called simplices. The decomposition are based on the solid grid lines. Since in the structural solver the total Lagrangian formulation is used, every simplex is always associated with the same solid grid cells and will not change with time. The location of the triangle elements are updated from the solid displacement field. On the other hand, the flow field is solved with Eulerian method, before each time step, the mapping between updated simplices and the associated fluid grid points needs to be updated.

2.4.1 Interface Decomposition

In section 2.3.2.4, a surface decomposition algorithm using the middle cut triangularization was already described. The use of this triangularization method is easy to be implemented. This method also provides a systematic way to numerically calculate the surface and volume for irregular geometry. Nevertheless, this method tends to generate more simplices, and the geometry of the interface may be largely distorted near the edges and corners.

A new method without using the middle cut triangularization is proposed to reduce the number of simplices without distorting the surface geometry. It is assumed that the intersection between the cubic grid cell and the interface is nearly flat, so that the resulting cross section will be a polygon. There are four possible scenarios of polygon: triangle, quadrilateral, pentagon and hexagon. These polygon can be divided into 1 to 4 triangular elements. The first step of the decomposition is to figure out the intersecting points, which are the vertices of the polygon, between the grid lines and the interface. The intersecting points residing on the same face of cell are connected with line segments as shown in figure 2.13. The obtained polygon is then divided into triangle elements.

This new method is not meant to replace the middle cut triangularization used in the solid solver. It is introduced only for interface decomposition on generating Lagrangian triangle elements. Figure 2.14 and 2.15 show the surface decomposition of cubic shape and spherical shape simplices using the middle cut triangularization and the proposed method. It can be observed that using middle cut triangularization does generate more triangles and distort the

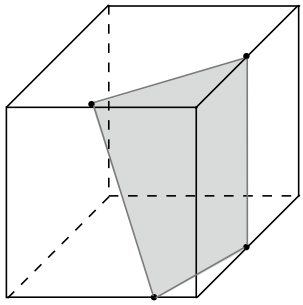

Figure 2.13: The quadrilateral intersection of a flat surface and a cubic grid cell.

shape near edges and corners. With the used of the proposed new method, the distortion of the sharp edges and corners is reduced, but the corners and edges will still be chamfered after the new proposed decomposition. The generated triangular elements may have small aspect ratio. However, the interface simplices element is introduced for information communication between fluid and solid solvers. The less number of simplices is more important than the consistency of the shape of the triangular elements.

2.4.2 Update the Signed Distance Field

In this research, the Eulerian interface description is used in the solid and fluid solvers, while the Lagrangian simplices are also introduced for the information communication. Once the structure deforms, the updated location of the simplices can be obtained. The signed distance field also needs to be updated according to the current configuration of the simplices.

To update the signed distance function, the distance between each grid point to the nearest triangle element is computed. Considering the distance from a triangle bounded with vertices $\underline{P_1}$, $\underline{P_2}$, $\underline{P_3}$ and an arbitrary point $\underline{P}$. These three vertices is coplanar on plane P_{123}, and the distance from $\underline{P}$ to P_{123} can be computed from $\|\underline{P} - \underline{P_0}\|$, where $\underline{P_0}$ is the projection point of $\underline{P}$ on the plane. However, $\|\underline{P} - \underline{P_0}\|$ only can be regarded as the nearest distance from $\underline{P}$ to the triangle only when $\underline{P_0}$ lies inside the triangle as shown in figure 2.16. To figure out whether $\underline{P_0}$ lies inside the triangle, $\underline{P_0}$ can be written as the linear superposition

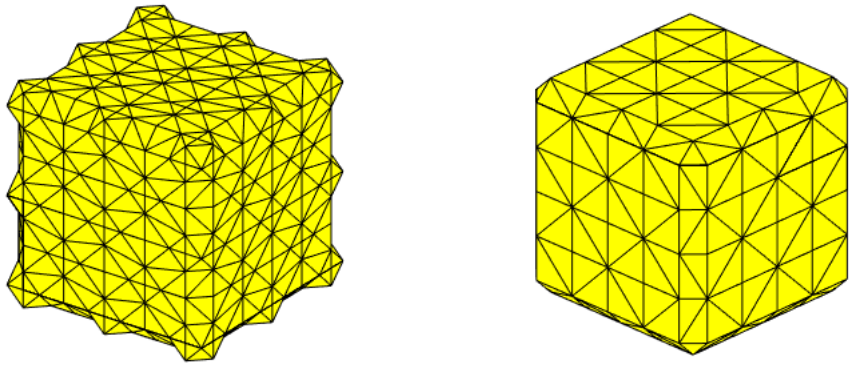

(a) (b)

Figure 2.14: Decomposition of the surface of a cubic object using the middle cut triangularization (left) into 848 elements and the proposed method (right) into 296 elements. The cube is with length 0.24 and the grid cell size is 0.05.

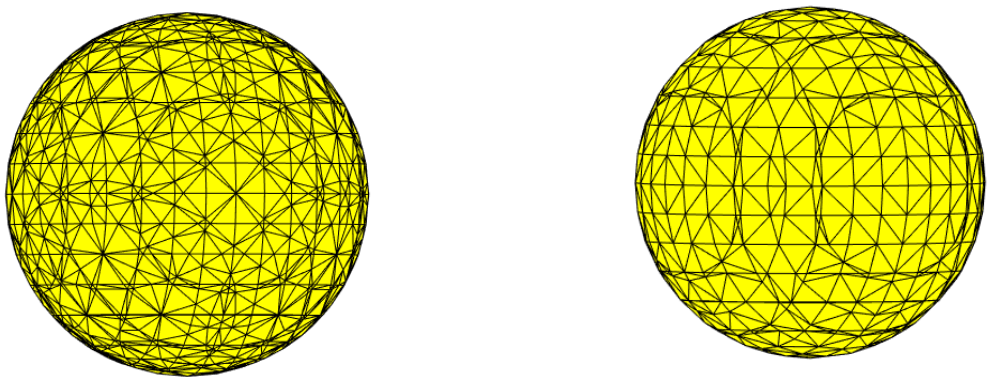

(a) (b)

Figure 2.15: Decomposition of the surface of a spherical object using the middle cut triangularization (left) into 3224 elements and the proposed method (right) into 1304 elements. The sphere is with radius 0.3 and the grid size is 0.05.

of the three vertices,

$$\underline{P_0} = c_1\underline{P_1} + c_2\underline{P_2} + c_3\underline{P_3}, \tag{2.90}$$

where the coefficient c_1, c_2 and c_3 satisfy the relation $c_1 + c_2 + c_3 = 1$ since $\underline{P_0}$ is coplanar with the three vertices. The signs of the three coefficients indicate the relation between $\underline{P_0}$ and the triangle as listed in figure 2.16. The plane P_{123} can be divided into seven regions by the extension lines of the sides of the triangle. Here we denote $\underline{P_B}$ to be the nearest point on the triangle to the point $\underline{P}$. Following are the three different scenarios according to the signs of the coefficients:

1. $\underline{P_B}$ inside the triangle

   If all the three coefficients are positive, $\underline{P_B}$ is equivalent to $\underline{P_0}$ and it will be located inside the triangle. (case (1) in figure 2.17)

2. $\underline{P_B}$ on the side

   If there is more than one negative coefficient, the projection point must lies outside of the triangle. For example, consider the case in the figure 2.16, if the coefficient c_1 is negative, this implies $\underline{P_0}$ is outside of the side $\underline{P_2P_3}$. In this case, find the projection point from point $\underline{P_0}$ to $\underline{P_2P_3}$. If the projection point lies between $\underline{P_2}$ and $\underline{P_3}$, the projection point is then the $\underline{P_B}$. (case (2) in figure 2.17)

3. $\underline{P_B}$ on the vertex

   If in the previous case, $\underline{P_0}$ is outside $\underline{P_2P_3}$ and the projection point from $\underline{P_0}$ to $\underline{P_2P_3}$ lies outside of $\underline{P_3}$, then the $\underline{P_B}$ is $\underline{P_3}$. (case (3) in figure 2.17)

Once the location of $\underline{P_B}$ is determined, the distance from point $\underline{P}$ to the triangle is $\|\underline{P} - \underline{P_B}\|$. The distance from a point to the nearest triangle is the magnitude of the signed distance function on that point. The sign of the signed distance function is determined from the normal vector of the simplex. If $\left(\underline{P} - \underline{P_B}\right) \cdot \underline{N}$ is positive, this means than the sign distance function on $\underline{P}$ is positive and vice versa.

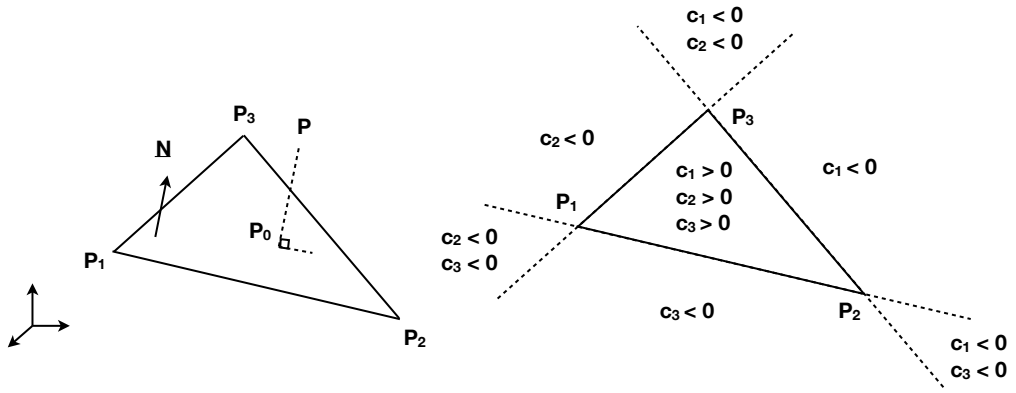

Figure 2.16: Left: the projection point $\underline{P_0}$ of the point $\underline{P}$ on the plane P_{123}. Right: the sign of the coefficients c_1, c_2 and c_3 in the seven regions defined by the extension lines of the three sides of the triangle.

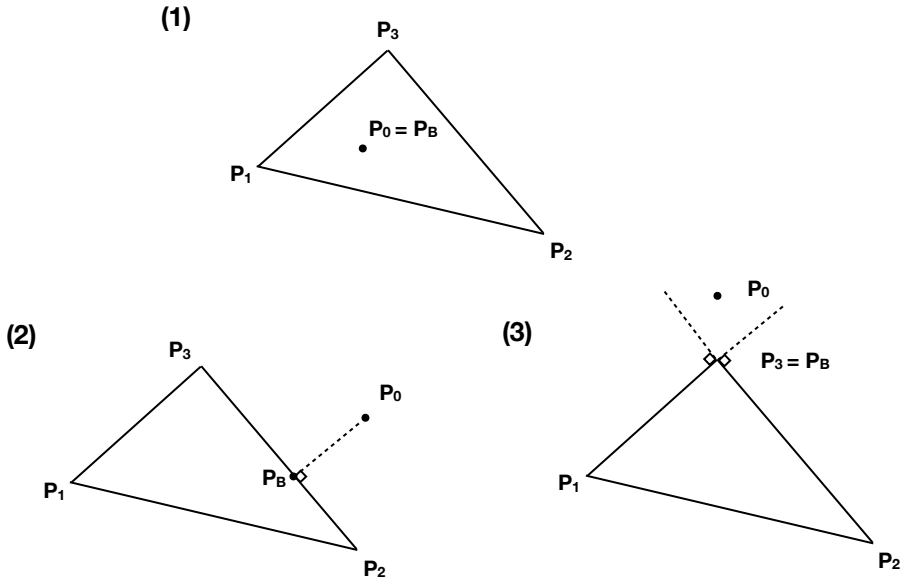

Figure 2.17: Three scenarios of the location of the nearest point on the triangle, $\underline{P_B}$, to the point $\underline{P}$.

2.5 Fluid–Solid Interaction

At the fluid–structure interface, the kinematic and dynamic boundary conditions should be satisfied at the same time. To couple the separate fluid and solid solvers described above, a strong-coupling partitioned method is used to combine the solvers together. For the fluid solver, the inputs needed are the boundary location and velocity. On the other hand, for the solid solver, the input information is the traction on the solid boundary. It is a natural choice for the solvers to form a loop so that they can use the output from each other as the input information. The loop continues until the interface conditions converge.

For the interface description, the signed distance field is used in the solid and fluid solvers for its convenience in obtaining the required information for field reconstruction at the fluid forcing points and in acquiring the configuration of the cut-cell structure. However, it is not trivial to exchange the information of velocities and traction from one system to another using the signed distance field. A set of Lagrangian triangular elements are utilized as the description of the fluid–structure interface to provide auxiliary information interchange between the two systems introduced in the section 2.4. These triangular elements, which are also called simplices, are defined from the intersection points between the interface and the doubly refined grid lines in the solid domain. The set of simplices are an approximation of the interface geometry. In this manner, the resolution of the interface is twice the resolution of the solid grid. The signed distance field is updated from the updated location of the simplices.

The critical aspect of the coupling is the communication of information between the fluid and solid solvers. The interface velocities can be readily transferred from the solid to the fluid by evaluating the trilinear shape functions in each element. With the field reconstruction using the linear interpolation and the tetrahedron stencil described in the section 2.2, the velocity gradients and pressure can be evaluated at the centroid of each triangular interface elements. The stencils include the centroid of the specific triangle element and three nearby fluid points which are not forcing points. After getting the pressure and velocity gradient on

each centroid of the simplices, the traction exerted on each simplex can then be obtained. Because of the piecewise constant shape function of the traction in the present finite element analysis, the traction in a cell is obtained from the weighted average of the traction on the simplices corresponding to that traction cell.

Figure 2.18 depicts the strong-coupling algorithm in the present work. To advance from step n to $n+1$:

1. The initial guesses of the locations $\mathbf{x}_I^{(0)}$ and velocities $\mathbf{v}_I^{(0)}$ of the Lagrangian simplices, which are usually the values obtained in the previous step, are made.

2. The signed distance field needed in the fluid immersed-boundary solver is generated according to the configuration of the simplices. The velocities on the boundary points associated with the velocity forcing points can be computed.

3. The fluid field is advanced for one step. The updated interface traction from the fluid on the structure is obtained.

4. The structure is advanced for one step. The locations $\mathbf{I}_b^*$ and velocities $\mathbf{v}_I^*$ on the Lagrangian simplices are updated.

5. Compare the locations of the simplices between the input to the output of iteration k. If their discrepancy is larger than the tolerance value tol_{fsi}, repeat the steps 2 to 4. The $(k+1)^{\text{th}}$ iterations of the marker locations and velocities are the weighted sum of the input and output marker data with the relaxation parameter ω to ensure the numerical stability of the iteration.

6. If the discrepancy between the input and output of the simplices locations (which is defined as the square root of the sum of square of distances between the input and output positions of the simplices' centroid) is smaller than the tolerance value, the kinematic and dynamic boundary conditions are deemed satisfied on the interface and the updated state at step $n+1$ can be obtained.

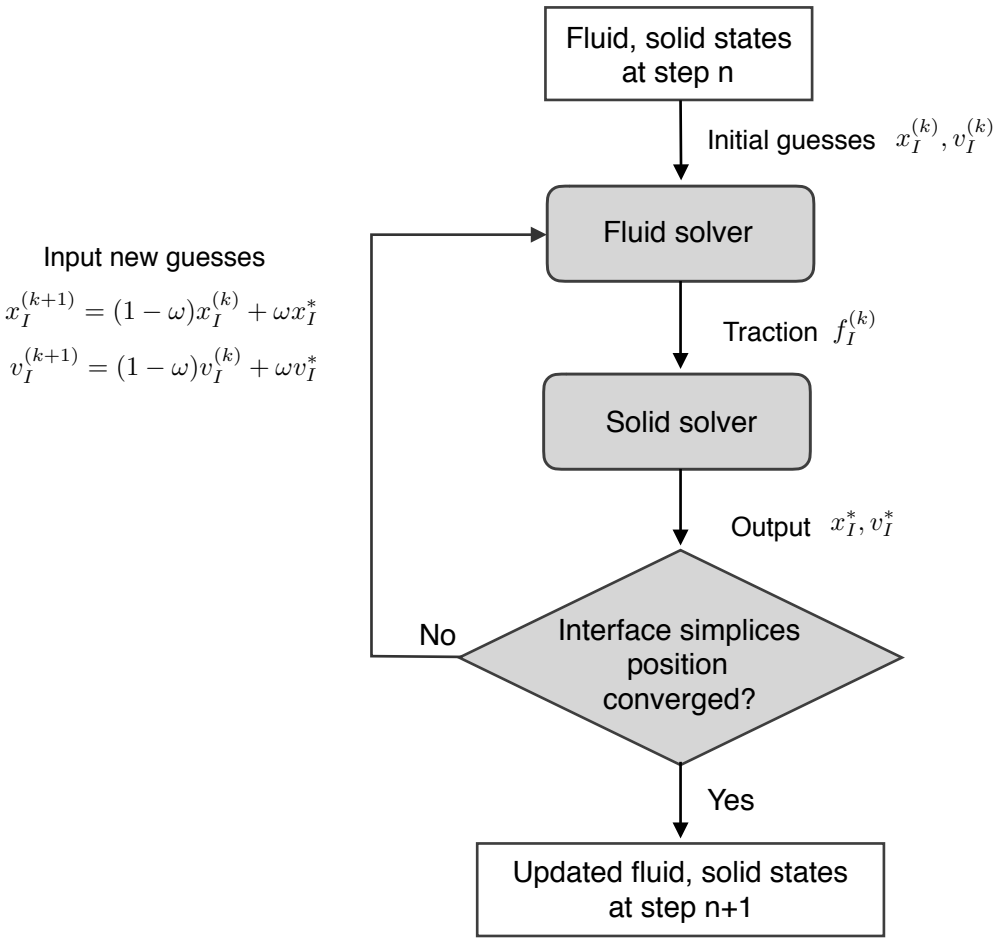

Figure 2.18: The strong coupling iterative algorithm of fluid–structure interaction.

2.6 Parallel Computing

The parallel computing is introduced with MPI (Message Passing Interface) and PETSc (Portable, Extensible Toolkit for Scientific computation) (Balay et al., 2016) for computation on distributed memory multiprocessor computer system. PETSc is designed for parallel computing on dealing with the partial differential equations with scientific applications. PETSc provides data structures of distributed vector and matrices. It also has modules dealing with domain partitioning and data management for the structured grid, Krylov subspace iterative linear equation solver, algebraic manipulation on distributed matrices and vectors, data communications, and etc.

The fluid domain and the solid domain may have different grid sizes and domain sizes. For parallel computing, these two domains are partitioned independently (for example, as shown in figure 2.19). Each processing element will store a portion of the field information. When updating the field variables, the information on the nearby grid points may be needed. In other words, when updating the values on the bordering points, the field information on the ghost points, which are the bordering portion of points belonging to the neighboring processes, may be needed. So that the communication of the data on the ghost points between processes is necessary.

When it comes to the interaction at the interface, the data on the simplices is partitioned in two different ways: one according to the fluid domain partitioning and other one according to the solid domain partitioning. Figure 2.19 shows one example of data distribution on fluid domain, solid domain, and of interface markers. Consider a bounded flow in a elliptic cavity surrounded by deformable structure. Both the solid and fluid domain are partitioned into four parts, and the fields are separately stored in four processors. For the interface markers, after the solid solver advancing the displacement field for one step, process 0 and 2 will calculate the updated information of its local portion of markers. The updated position, velocities and acceleration on the markers needs to be redistributed to match the partitioning of the fluid domain before we can update signed distance function on the fluid points in each

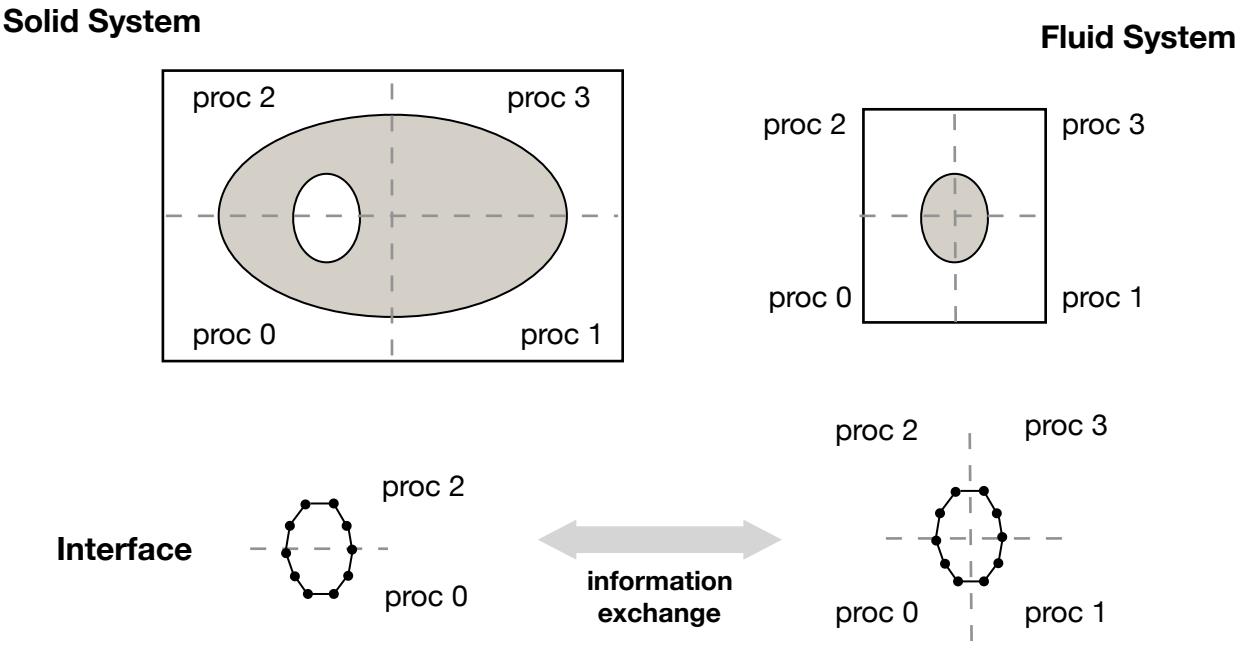

Figure 2.19: Domain partitioning example of the solid domain (top left), fluid domain (top right) and the Lagrangian interface markers (bottom) in a FSI problem.

process. In this example, information of some markers in process 2 needs to be sent to process 3. Similarly, information of some markers in process 0 also needs to be sent to process 1.

CHAPTER 3

Medical Image Processing

In this work, patient-specific nasopharyngeal airway and surrounding tissue geometries are obtained from cone-beam computed tomography (CBCT) scans of the head and neck. Patient data in the present study is drawn from the archives of the Oral & Maxillofacial Radiology Clinic and the Oro-facial Pain & Dental Sleep Medicine Clinic at the UCLA School of Dentistry. The CBCT scans (Figure 3.1) have isotropic voxels with a resolution of 0.3 mm, and are stored as a series of axial slices in DICOM format. Each voxel is assigned a gray value number, where larger gray values represent highly attenuating tissues such as cortical bone or soft tissue, and lower gray values represent low attenuating substances such as air. Image processing is necessary to convert the obtained CBCT scan data to the required signed distance field for the solver. This is achieved using the image processing toolbox of the MATLAB scientific software package MATLAB Image Processing Toolbox, and ITK-SNAP, the segmentation tool for 3D medical images (www.itksnap.org) (Yushkevich et al., 2006).

Two different ways of segmentation were used. In the simulation with the fixed airway geometry, MATLAB imaging processing toolbox can extract the airway geometry automatically because of the high contrast between the CBCT gray value of air and tissue. However, for soft tissue segmentation, different kinds of soft tissue are hard to be distinguished in the CBCT scan. The manual segmentation is done using ITK-SNAP for the FSI simulation. The following sections illustrates the procedures to acquire the upper airway and soft tissue geometries and the signed distance field with these two image processing softwares.

3.1 Image Processing with Matlab

To obtain the airway geometry for the simulation of the fixed airway, these DICOM files are imported by series into MATLAB. The region of interest is selected to extend from the level of the hard palate to laryngopharynx, inferior to the epiglottis. (See the region within the red lines in figure 3.1.) The grey value thresholding is applied to distinguish the border of the air and soft tissue. The thresholding grey value is chosen manually and may differ between patients. (Unlike CT Housefield units, CBCT gray values depend on the attenuating properties of neighboring anatomy, and are not invariant between patients of different anatomic size and structure.) The thresholding process will isolate all voxels within a specified gray value range in the region of interest, including those outside the nasopharyngeal airway, such as those from artifact and pockets of air within the oral cavity. It will also fail to include voxels within the airway of uncharacteristically high gray values, due to noise or artifact. This inevitably creates undesired internal and external extraneous isolated clusters of voxels, as shown in the Figure 3.2(a). The MATLAB function `bwareaopen` removes any clusters of connected points with fewer than some specified number; this helps to eliminate the undesired clusters of low gray value voxels outside the airway, and those of high value within the airway.

Next, the signed distance field of the airway is determined through the MATLAB function `bwdist`. Soft tissue (outside the airway) and air (inside the airway) are arbitrarily defined to have negative and positive values, respectively. The boundary of the airway, which is indicated by the zero level set of the signed distance field, still contains fine-scale noise inherent from the CBCT scan (figure 3.2(b)). This may lead to a large number of degenerate cases in the immersed-boundary fluid solver and thereby reduce accuracy near the boundary. To resolve this problem, smoothing—using Gaussian filters—is applied to the signed distance field using the MATLAB function `imfilter`. The airway geometries after Gaussian filtering are shown in the figure 3.3 with standard deviations of 1.6 (left) and 3.2 (right). The application of a Gaussian filter may lead to a reduction of the cross sectional area or volume

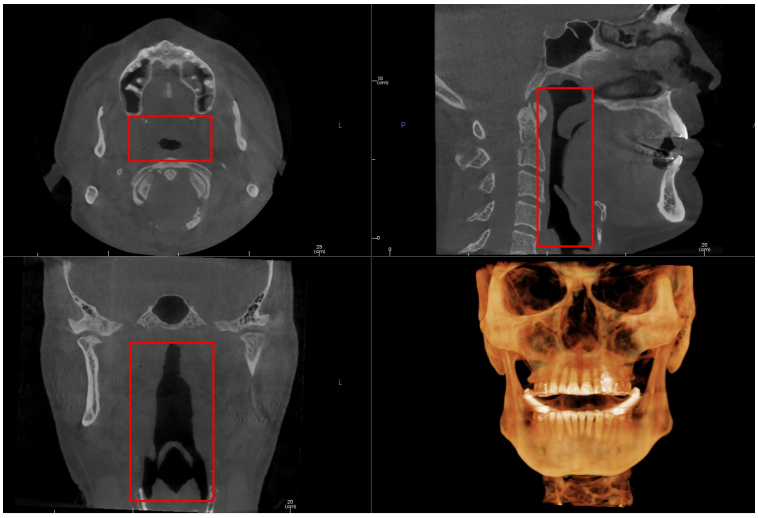

Figure 3.1: The CBCT scan data in the axial (upper left), sagittal (upper right), coronal (lower left) slices, and the 3D volumetric view (lower right). The region of interest is outlined by the red box.

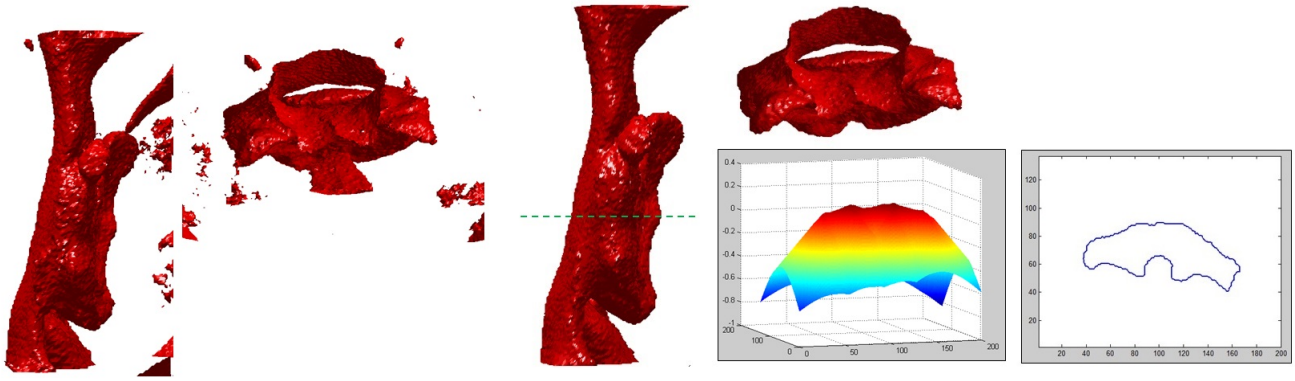

(a) (b)

Figure 3.2: (a) The air-tissue boundary after applying the thresholding in side view (left) and top view (right). (b) The air-tissue boundary after removing the undesired internal and external clusters. The lower right plots show the signed distance function and the tissue-air boundary of one axial slice (indicated by the green dashed line).

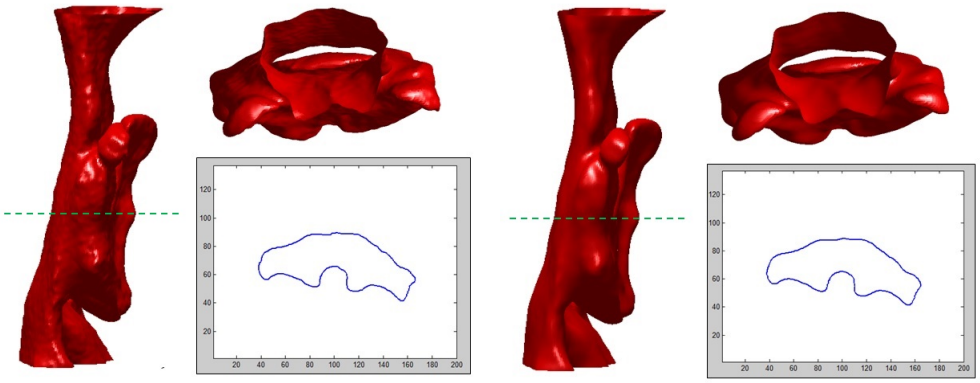

(a) (b)

Figure 3.3: (a) The air-tissue boundary after applying Gaussian filters of standard deviations of 1.6 (a) and 3.2 (b), with a selected axial slices at positions indicated by the green dashed lines.

of the airway. To explore this, the change in size of the smallest cross sectional area before and after smoothing was determined. The maximum reduction of the cross-sectional area or volume of the airway is calculated to be $< 5\%$ and $< 1\%$ for Gaussian filtering of standard deviations 3.2 and 1.6, respectively. Lastly, the smoothed signed distance field is interpolated onto the staggered velocity component and pressure grid points for determining forcing points and interpolation stencils in the fluid solver.

3.2 Segmentation with ITK-SNAP

In the FSI simulation, deformation of the tissue structure near the upper airway needs to be considered. Besides the soft palate and the tongue tissue, there are muscle, pharyngeal wall, bone and fat tissues around the upper airway (Schwab et al., 1995). Because the current solid solver is still lack of proper contact model to deal with the contact interaction between multiple structures, in the FSI model the soft tissues around the upper airway will be regarded as all connected together and having with uniform property.

According to the volumetric reconstruction of the upper airway tissue with magnetic resonance images (MRI) by Schwab et al., the soft palate, tongue, and pharyngeal walls are

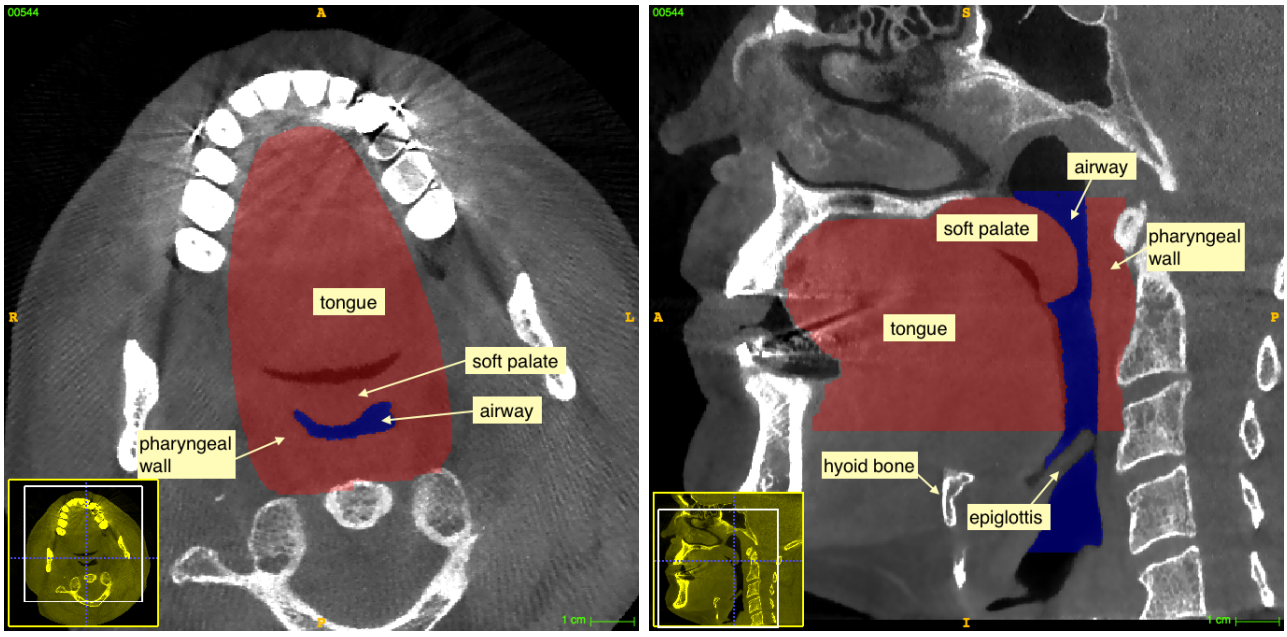

(a) (b)

Figure 3.4: The horizontal view (a) and the sagittal view (b) of the segmented tissues (red) and airway (blue) geometries.

the main soft tissues around the airway. These soft tissues and the airway geometries are manually segmented using ITK-SNAP following the tissue or tongue geometry described in Schwab et al. (2003), Buchaillard et al. (2009), and (Stavness et al., 2012).

The horizontal and the sagittal views of the segmented airway and tissue geometries are shown in the figure 3.4. The red color denotes the tissue geometry and the blue color denotes the upper airway. The tissue only contains the region starting from the top of the epiglottis to the hard palate, and from the tip of the tongue to the spine. The three-dimensional segmented geometries are shown in the figure 3.5.

The segmented data is saved as .mha file and is input into Matlab for further image processing. The procedures to generate the signed distance field and smoothing with Gaussian filter are the same as described in the previous section. However, since the surface of the geometries obtained from manual segmentation is uneven, three times of Gaussian filtering with deviation 2.33, 2.33, 1.48 are used to smooth out the surface. The tissue and airway

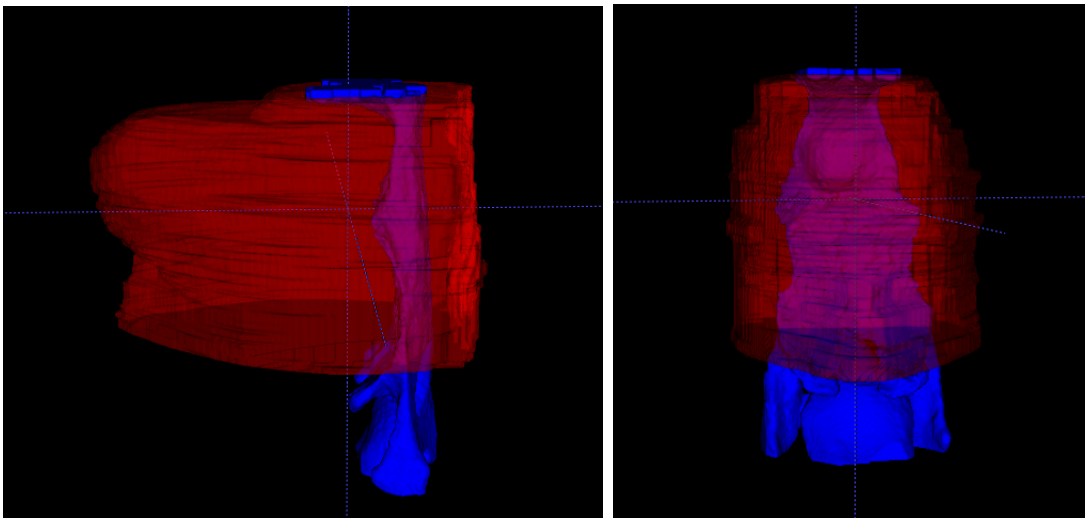

(a) (b)

Figure 3.5: The side view (a) and the front view (b) of the 3d segmentation of the tissues (red) and airway (blue).

geometry after smoothing are plotted in the figure 3.5.

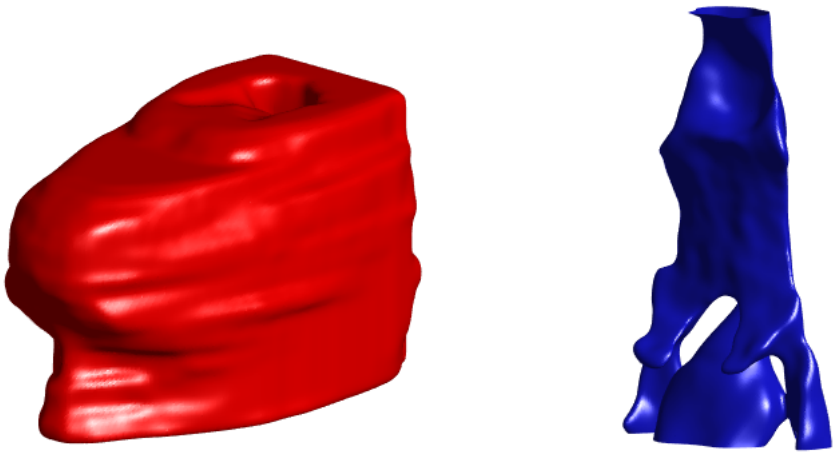

(a) (b)

Figure 3.6: The tissues geometry (left) and the airway geometry (right) after smoothing with Matlab.

CHAPTER 4

Results

The results shown in this chapter are divided into two parts. One main objective of this research lies in the numerical tool development of a novel approach of using purely non-body-conformal Cartesian grid. The first part includes the validation of the fluid solver, solid solver and the FSI solver separately. The scalability tests are conducted to test the performance of the parallel computing on the FSI problem. The second part includes the results related with the patient-specific geometries. The pressure driven flow in the rigid upper airway and the airflow-tissue interaction in upper airway are conducted.

4.1 Simulation of Validation Problems

4.1.1 Fluid Solver

The sharp interface immersed boundary method (embedded-boundary formulation) has been proven to be nearly second order in the Yang and Balaras (2006) with the simulation of the flow past circular cylinder. Here we tested the accuracy with an internal flow of the 2D simulation of flow in the channel with prescribed motion. The channel wall is only allowed to move in the y-direction and the wall displacement is prescribed to be a moving sinusoidal wave with wave length λ and angular frequency ω (see figure 4.1). The wall displacements are set to be

$$\xi = 0, \qquad \eta = Ae^{i\omega(t-x/c)}$$

where ξ and η represents the x- and y- component of the wall displacement, A is the amplitude of wall displacement, and c denotes the wave speed $c = \omega\lambda$.

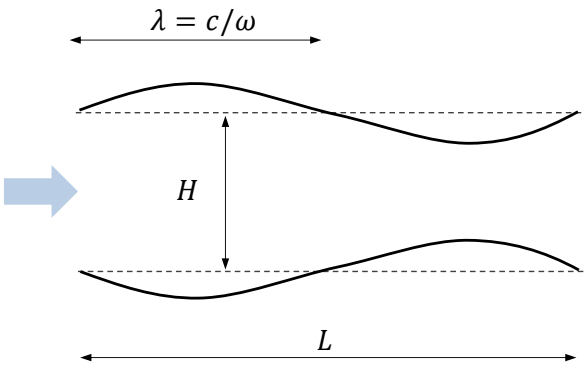

Figure 4.1: Channel configuration and prescribed wall displacement.

Under the assumption of infinitesimal wall deformation compared with channel height and relatively small induced velocity field, the analytical solution of the flow field can be obtained,

$$p = \text{Real}\left[B\left(e^{2\pi y/c} + e^{-2\pi y/c}\right)e^{i2\pi(t-x/c)}\right] \tag{4.1}$$

$$u = \text{Real}\left[\left(C_1\left(e^{2\pi y/c} + e^{-2\pi y/c}\right) + C_2\left(e^{\gamma y} + e^{-\gamma y}\right)\right)e^{i2\pi(t-x/c)}\right] \tag{4.2}$$

$$v = \text{Real}\left[\left(D_1\left(e^{2\pi y/c} - e^{-2\pi y/c}\right) + D_2\left(e^{\gamma y} - e^{-\gamma y}\right)\right)e^{i2\pi(t-x/c)}\right] \tag{4.3}$$

where

$$\gamma \equiv \sqrt{2i\pi\,\text{Re} + \frac{4\pi^2}{c^2}}, \qquad \text{Re} \equiv \frac{\rho L^2 \omega}{2\pi\mu}, \tag{4.4}$$

the coefficients are

$$C_1 = \frac{-2\pi A}{\left(e^{\gamma/2} + e^{-\gamma/2}\right)\left(-\tanh\left(\pi/c\right) + \frac{2\pi}{c\gamma}\tanh\left(\gamma/2\right)\right)}, \tag{4.5}$$

$$C_2 = \frac{2\pi A}{\left(e^{\gamma/2} + e^{-\gamma/2}\right)\left(-\tanh\left(\pi/c\right) + \frac{2\pi}{c\gamma}\tanh\left(\gamma/2\right)\right)}, \tag{4.6}$$

$$B = cC_1, \quad D_1 = iC_1, \quad D_2 = \frac{2i\pi}{c\gamma}C_2, \tag{4.7}$$

and the time is non-dimensionlized by $2\pi/\omega$, length by channel length L, velocities by $\omega L/2\pi$, pressure by $\rho\left(\omega L/2\pi\right)^2$, and ω by $2\pi/\omega$. Thus the non-dimensionalized angular frequency is a constant 2π.

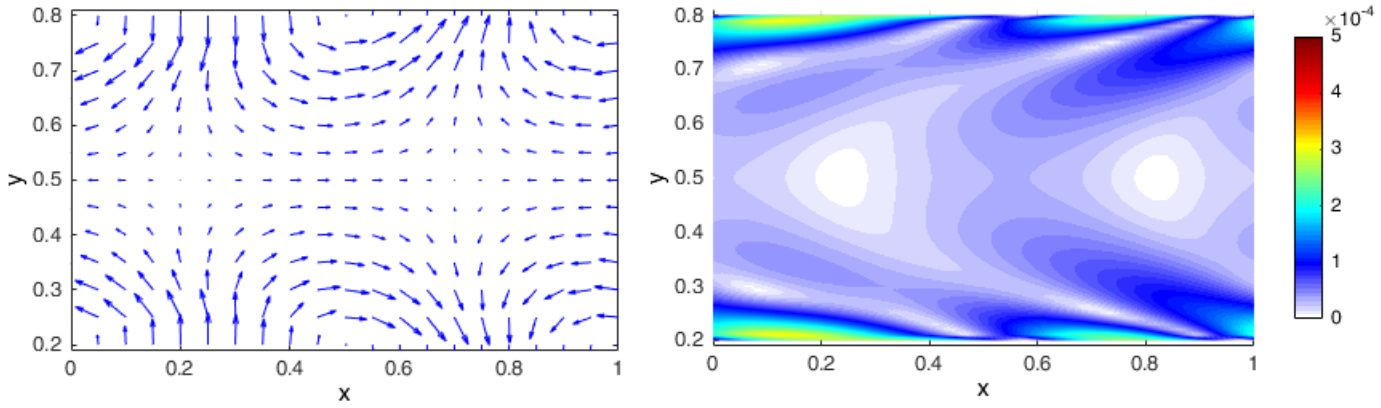

Figure 4.2: Left: the velocity field of the flow in the deforming channel at $t = 5$ with infinitesimal deforming amplitude. Right: the error distribution of velocity magnitude between the present work and the analytical solution.

The validation case of flow in the deforming channel is at $\mathrm{Re} = 100$ with wave speed $c = 1$. The channel height is chosen to be 0.605 in order to prevent both u and v forcing points from being conformal to the boundary. The amplitude of wall motion A is set to be 0.001. The simulation is conducted in a 1 by 1 domain, and the periodic boundary conditions are set at channel inlet (left side) and outlet (right side). Four kinds of grid sizes $\Delta x = 0.01, 0.0125, 0.025, 0.05$, and the corresponding time step sizes $0.001, 0.00125, 0.0025, 0.005$ are used. The obtained velocity vectors at $t = 5$ using $\Delta x = 0.01$ are shown in figure 4.2. The error distribution of the velocity magnitude field compared with analytical solution is plotted at the right in figure 4.2. The error is larger near the boundary on the order of 10^{-4}, while the error near the centerline of the channel reduces to the order of 10^{-5} with respect to the characteristic velocity $\omega L/2\pi$.

The L^2 norm error with different simulation resolution are depicted in figure 4.3. This shows that the rate of convergences for the x- and y- component of velocities are between first and second order of accuracy. In other words, the field reconstruction of the bilinear interpolation (in two-dimensional simulation) near the boundary may deteriorate the order of accuracy, but the accuracy still remains better than first order.

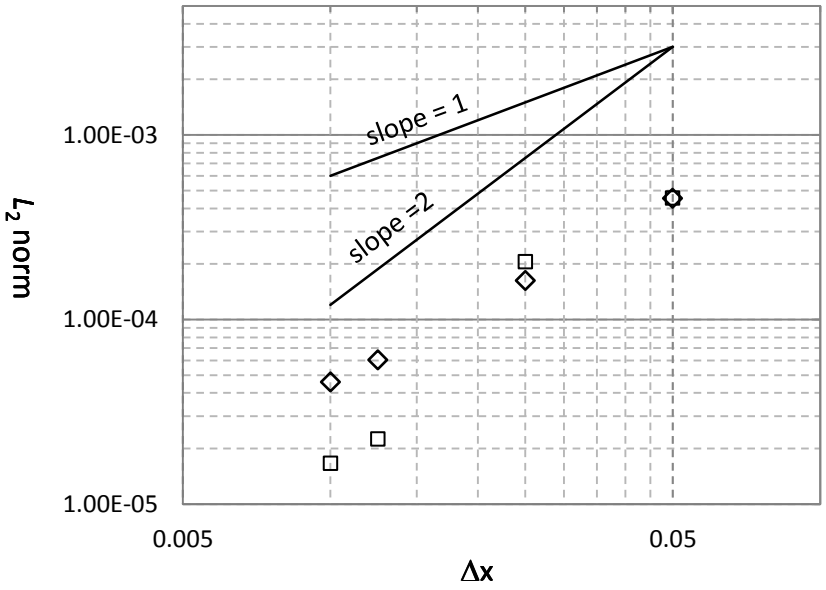

Figure 4.3: The L^2 norm error of fluid velocity field u ($\diamond$) and v ($\square$).

The flow simulation in the channel with larger wall deformation is also conducted. The amplitude $A = 0.05$ and fix the other parameters used in the previous simulations of infinitesimal wall deformation. The grid size is chosen to be 0.01 and size of time step is 0.001. The velocity field at $t = 1$ is plotted in figure 4.4.

4.1.2 Solid Solver

In the following section the solid solver will be validated with the classic cantilevered beam problem. The problem setup is chosen to be the same as in Bathe et al. (1975) and Tian et al. (2014). The two-dimensional and three-dimensional simulations of the cantilevered beam under uniformly distributed load are performed. The tests are designed to validate the nonlinear elasticity finite element formulation and the cut-cell treatment of the developed solver.

The configuration of the beam is shown in the figure 4.5. The beam is with length $L = 1$

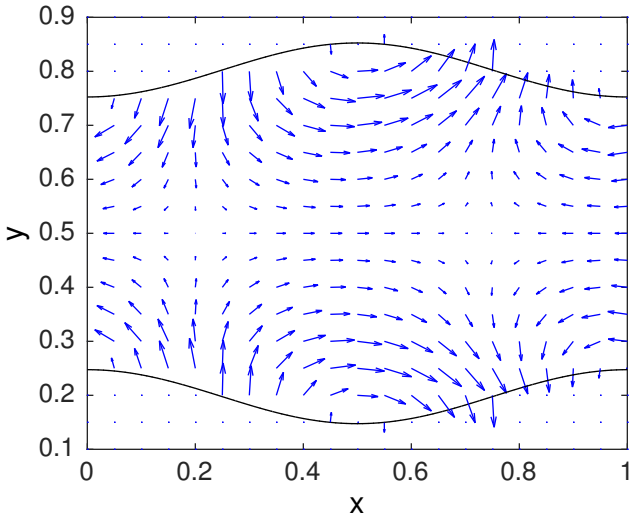

Figure 4.4: The velocity field of the flow in the deforming channel at $t = 1$ with deforming amplitude 0.05.

in, height $h = 0.1$ in, width $b = 0.1$ in, and density $\rho = 10^{-6}$ lbf s^2/in^4. The Young's modulus and poisson ratio are $E = 12000$ lbf/in^2 and $\nu = 0.2$. The uniformly distributed load with strength $q = 1.425$ lbf/in^2 is uniformly distributed on the upper and lower surface of the beam. There are no traction acting on the front and back surface of the beam.

4.1.2.1 Test of Two-Dimensional Nonlinear Elasticity Formulation

The two-dimensional simulations of the beam deformation with linear and nonlinear elasticity formulations are tested. The linear elasticity solver utilizes the mixed finite element method described in Bannier (2012), which is originally proposed by Zhu et al. (2012b). The displacement on the front-back direction is assumed to be zero. In other word, there exists additional stresses in the front-back direction to enforce the two-dimensionality.

The grid size is chosen to be $0.01L$ and the boundary of the beam is conformal to the grid lines. The time step size is $dt = 4.5 \times 10^{-5}$ s, which is 1/126 of the period of the beam oscillation. Three constitutive models are considered: linear elasticity, nonlinear elasticity formulation with and without iteration. No Rayleigh damping is added in the these

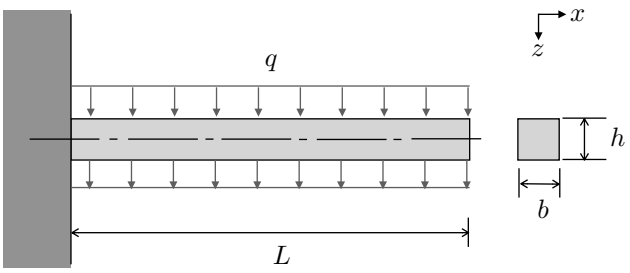

Figure 4.5: The configuration of the solid validation problem. The dimension of the cantilever beam is $L = 1$ in, height $h = 0.1$ in, width $b = 0.1$. The load pointing downward has strength $q = 1.425$ lbf/in^2.

simulations, so the oscillation amplitude of the beam is expected to stay constant, except for the influence of the numerical dissipation.

The z-displacement at the midpoint of the free end ($x = 1$ in) of the beam with the above-mentioned three models are plotted in the figure 4.6, comparing with the result in Bathe et al. (1975). It is worth noting that the amplitude of z-displacement calculated using the linear elasticity formulation is significantly larger than the amplitude obtained with the nonlinear elasticity formulation. The linear formulation ignoring the higher order terms in the strain measure is not adequate for structure undergoing large displacement and rotation. Figure 4.7 shows the distributions of material points in the beam at initial state and at its maximum displacement state. The obtained beam is elongated incorrectly with the prediction by linear elasticity formulation, especially near the free end. Under the linear elasticity, if an element is undergoing rigid body rotation, the normal strains are negative rather than zero. The element thus expands outward to remain zero strain under rigid body rotation. This is the reason why the element expansion is observed, and the degree of expansion increases toward the free end of the beam due to the larger rotation angle and larger displacement. On the other hand, under the nonlinear elasticity model, the Lagrangian Green strain $\underline{\underline{E}}$ remains

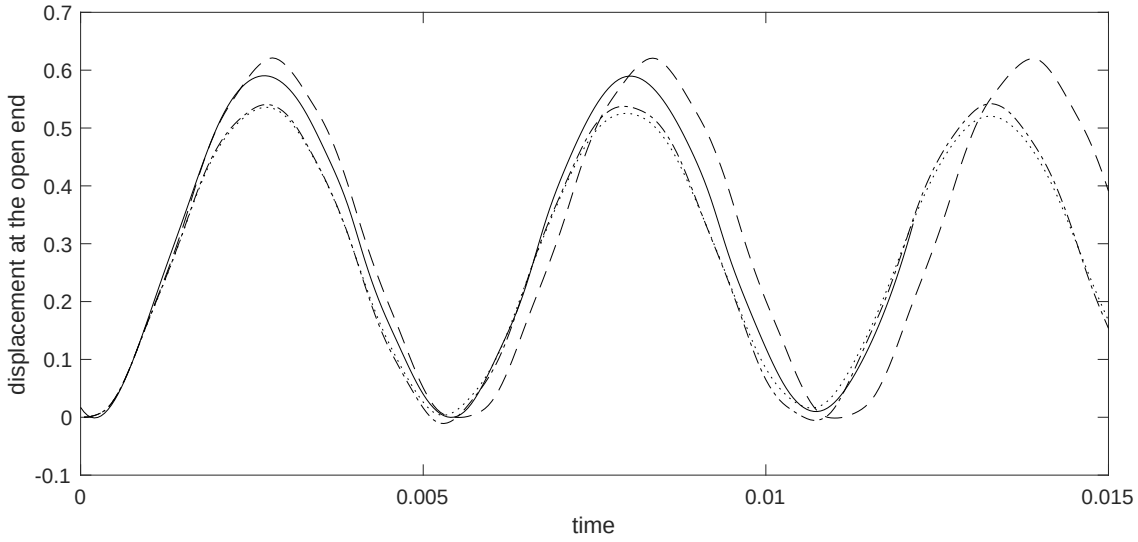

Figure 4.6: The z-displacement of the midpoint at the free end of the beam using linear elasticity (dashed line), nonlinear elasticity formulation without iteration (dotted line), nonlinear elasticity formulation without iteration (dot-dash line), and the results by Bathe et al. (solid line).

zero in the element undergoing rigid body rotation.

In the figure 4.6, the oscillation amplitude of the beam using the nonlinear elasticity formulation without iteration decreases slightly over time comparing with the result obtained using nonlinear elasticity formulation with iteration. This shows the dissipation of the internal energy over time without the iteration to reduce the out-of-balance of the internal and external energy. The dissipation becomes more obvious when the time step size increases as shown in the figure 4.8. These tests show that only using the nonlinear elasticity formulation with iteration can correctly predict the deformation of the structure undergoing large displacement and rotation.

4.1.2.2 Test of Three-dimensional Cut-Cell Treatment

In the three-dimensional validation, the simulations with body-conformal grid cells and non-body-conformal grids are performed to test the ability of the cut-cell treatment. The nonlinear elasticity formulation with iteration is used as the governing equations. For the body-conformal grid, the grid size is $dx = 0.02$, and the doubly refined grids are shown in the

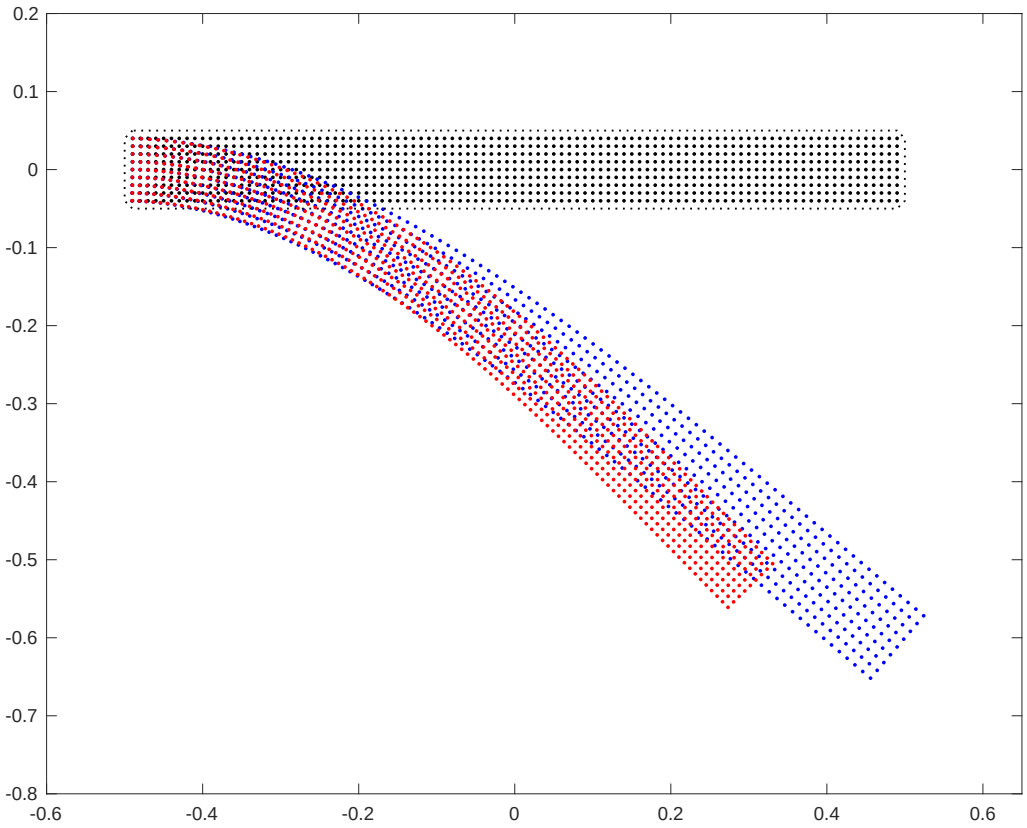

Figure 4.7: The location of the material marker points at initial state (black), and the marker points at the maximum displacement of the beam using linear elasticity formulation (blue) and nonlinear elasticity formulation with iteration (red).

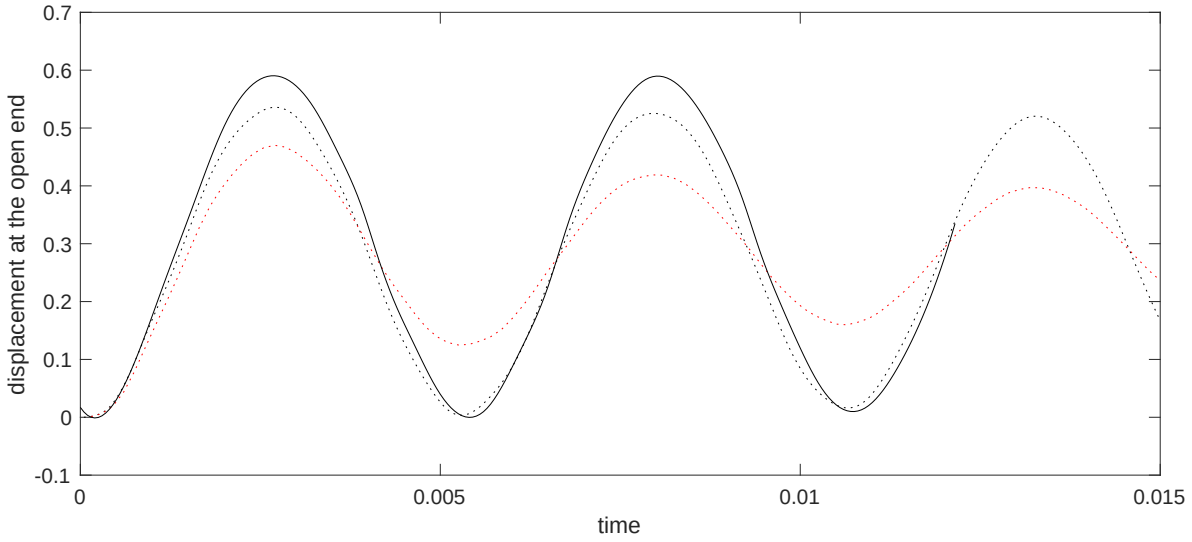

Figure 4.8: The z-displacement at the midpoint of the free end of the beam using nonlinear elasticity formulation without iteration with time step sizes $dt = 4.5 \times 10^{-5}$ s (blue dotted) and $dt = 1.35 \times 10^{-4}$ s (red dotted) comparing with the results by Bathe et al. (black solid).

figure 4.9. On the other hand, for the non-body-conformal case, a slightly smaller grid size is chosen $dx = 0.4/21 = 0.019048$, which is shown in the figure 4.10. The time step size is set to be $dt = 5 \times 10^{-5}$.

The z-displacement at the midpoint of the free end of the beam with two grid sizes are shown in the figure 4.11. The oscillation amplitude and the frequency in the present work are having a good agreement with the result by Bathe et al. (1975). This also demonstrates the ability of the cut-cell treatment. The figure 4.12 depicts the obtained distribution of the strain component E_{11} along the beam when it reaches the maximum displacement. The normal strain in the x direction E_{11} is positive (stretched) on the upper-half part and negative (compressed) on the lower-half part.

4.1.3 Fluid–Structure Interaction

In this section, an investigation of problems for the purpose of validating the fluid–structure coupling scheme described above is presented, including two- and three-dimensional problems.

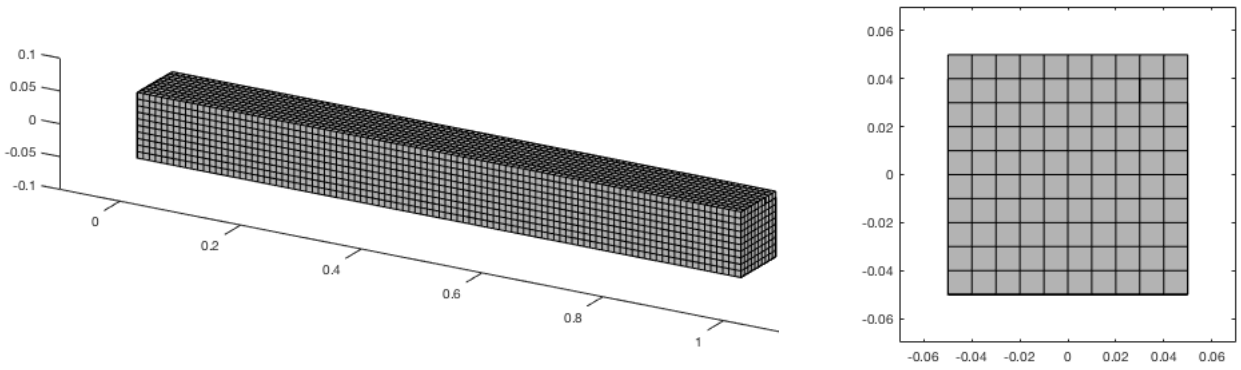

Figure 4.9: The body-conformal doubly refined grids with grid size $dx = 0.02$.

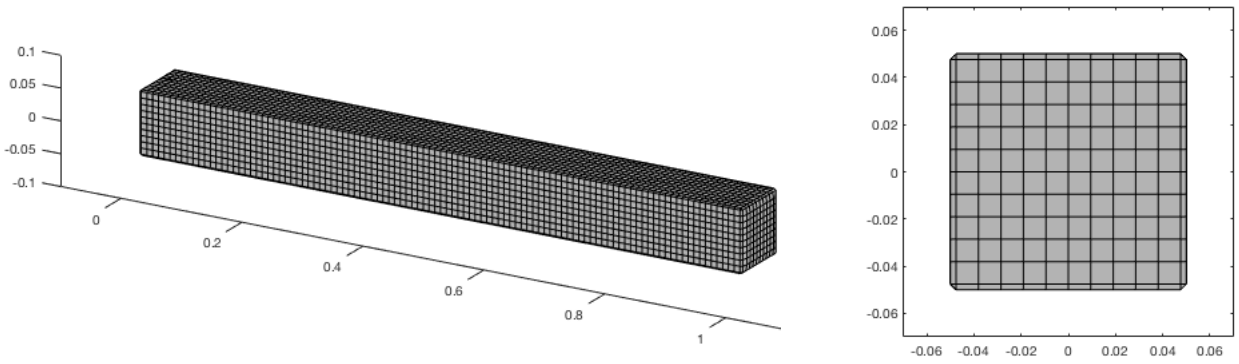

Figure 4.10: The non-body-conformal doubly refined grids with grid size $dx = 0.4/21 = 0.019048$.

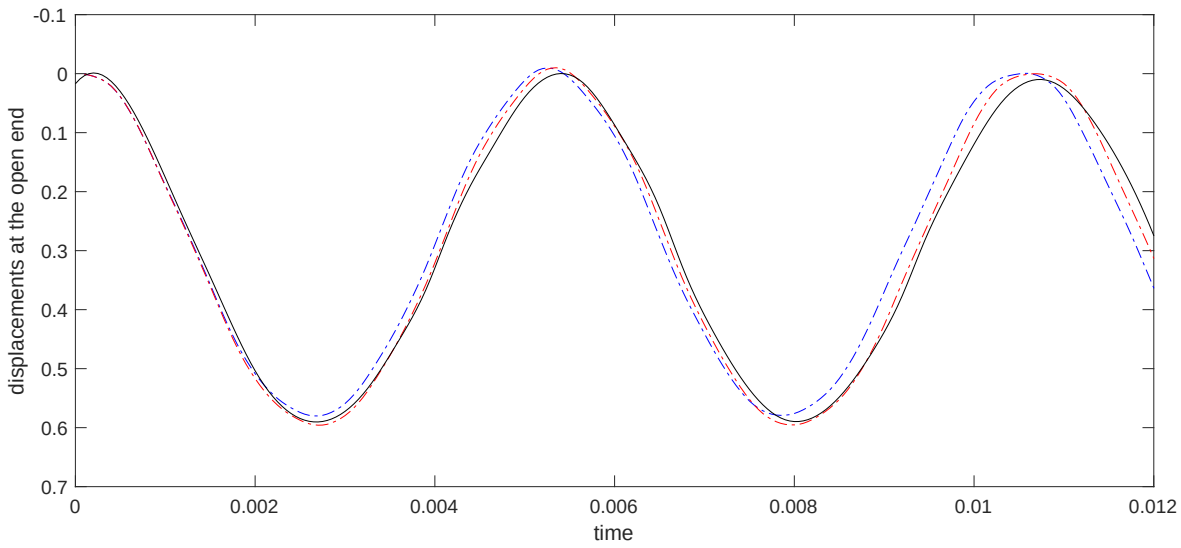

Figure 4.11: The z-displacement of the midpoint at the free end of the beam using body-conformal grids (blue dot-dash) and non-body-conformal grids (red dot-dash) comparing with the result by Bathe et al. (black solid).

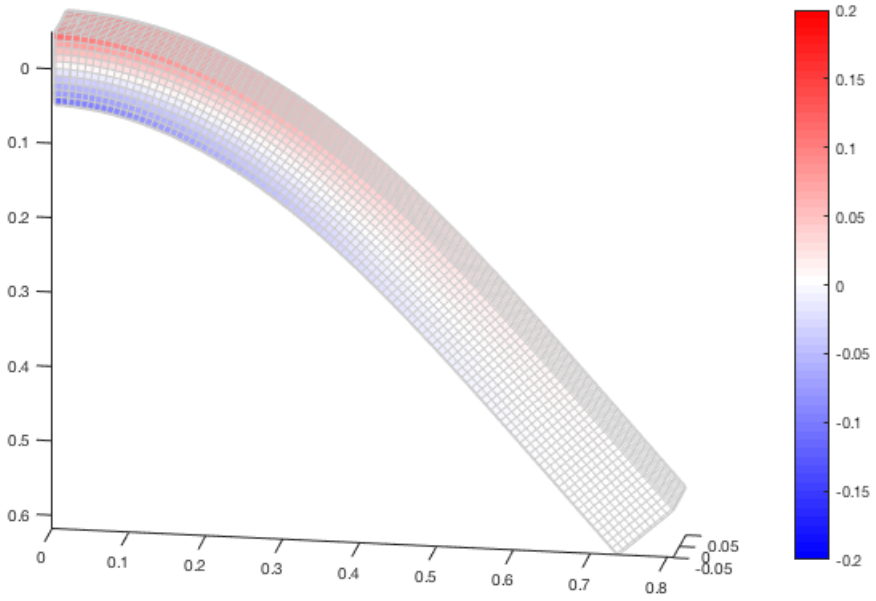

Figure 4.12: The distribution of the strain component E_{11} along the beam at the maximum displacement.

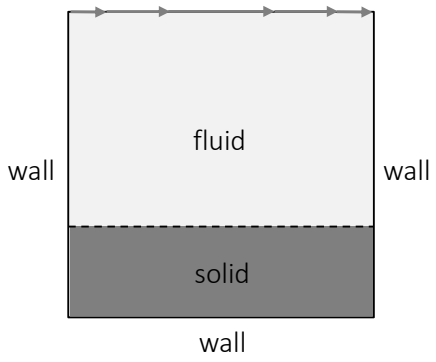

Figure 4.13: Lid-driven cavity flow with elastic material at the bottom.

4.1.3.1 The Two-Dimensional Lid-Driven Cavity Flow with Elastic Wall at Bottom

This cases consists of the deformation of an initially rectangular block of elastic material at the bottom of a lid-driven cavity, as shown in Figure 4.13. Because the tissue surrounding the upper airway are subjected to shear stress by the flow, which may lead to corresponding shear deformation, this validation problem aims to show the ability of the proposed FSI solver to handle such deformation. This problem, which eventually achieves a steady state consisting of the statically-deformed solid adjacent to the steady circulatory flow, has been considered previously in Dunne (2006) and Zhao et al. (2008). The square cavity—including fluid and solid—has height and width 2 and the rectangular solid has initial height 0.5 and length 2. The velocities at the cavity walls are fixed at zero, except for the velocity on the upper wall, which has non-zero velocity in the tangential (x) direction,

$$u = \frac{1}{2}\begin{cases} \sin^2(\pi x/0.6) & x \in [0, 0.3], \\ 1 & x \in (0.3, 1.7), \\ \sin^2(\pi(x-2)/0.6) & x \in [1.7, 2]. \end{cases} \tag{4.8}$$

For the solid, the Young's modulus is chosen to be 0.6. Our solid solver lacks the ability to strictly preserve the volume of the material. In order to approximately maintain incompressibility, the Poisson ratio is set to be 0.49. The left, right, and the bottom sides of

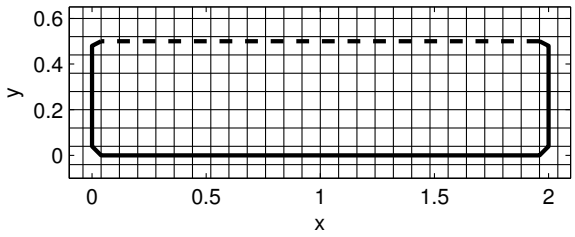

Figure 4.14: The non-body-conformal solid grid. The thick solid lines are the fixed boundary of the solid and the thick dashed line represents the fluid-solid interface. Note that the solid mesh extends beyond the cavity domain.

the rectangular solid are fixed, while the upper side is the fluid–structure interface. The size of initial elements in the solid mesh is uniformly 0.08 in both directions. The initially Cartesian solid mesh is purposely set up to not conform to the solid boundary or the fluid-solid interface (as shown in figure 4.14); this is done in order to test the capability of the cut-cell finite element method. The artificial Rayleigh damping uses coefficients with values $\alpha = 2.5 \times 10^{-4}$, and $\beta = 0.2038$, designed to ensure 2% damping of the first fundamental mode in a vacuum.

In the fluid, the viscosity is $\mu_f = 0.2$. The grid spacing in the fluid is uniformly 0.02, one quarter of the solid grid spacing; the domain is discretized into 100 by 100 cells. The density ratio between fluid and solid is $\rho_f/\rho_s = 1$. The tolerance for the fluid–structure coupling scheme is set to $\sqrt{2} \times 10^{-8}$. As to the choice of the relaxation factor, it was found that the preferred value of the relaxation factor is correlated with the density ratio ρ_f/ρ_s (Causin et al., 2005). In this case, the relaxation factor is set to 0.35 for most time steps, then is increased to 0.5 when the simulation approaches steady state. These choices are based on trial and error. The time step size is 5×10^{-4}. The problem is initially solved with a rigid solid until time $t = 3$, subsequent to which the solid is allowed to elastically deform. The system is considered to reach steady state when the velocities in the structure satisfy $\left\|\dot{X}\right\|_\infty < 10^{-4}$.

The streamlines and the solid deformation at steady state are compared with the results from previous work in Figure 4.15. Our results are in accordance with these previous results,

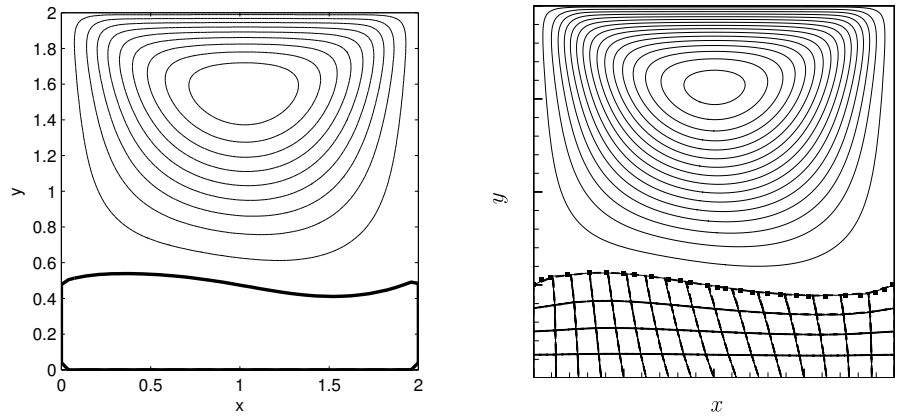

(a)

(b)

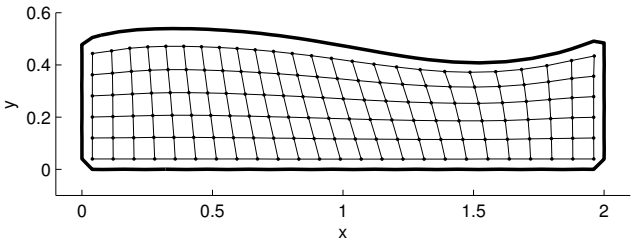

(c)

Figure 4.15: The streamline and deformation of solid at steady state. (a) present work. (b) results by Dunne (2006) (dots along interface) and Zhao et al. (2008) (streamlines and elastically-deformed mesh). (c) Solid deformation of present work.

despite our use of a non-body-conformal Cartesian mesh in the solid. This demonstrates the ability of our solver to use a non-body-conformal Cartesian mesh for treating fluid–structure interaction problems. The displacements and velocities in the y direction on the fluid-solid interface at $(1.6, 0.5)$ are shown in the left panel of Figure 4.16; the iterations required for the coupling scheme are reported in the right panel.

4.1.3.2 The Two-Dimensional Flow Induced Vibration of an Elastic Beam Behind a Rigid Cylinder.

The second case studied is an elastic beam mounted behind a rigid circular cylinder in a channel flow, as shown in Figure 4.17. This benchmark fluid–structure problem was originally

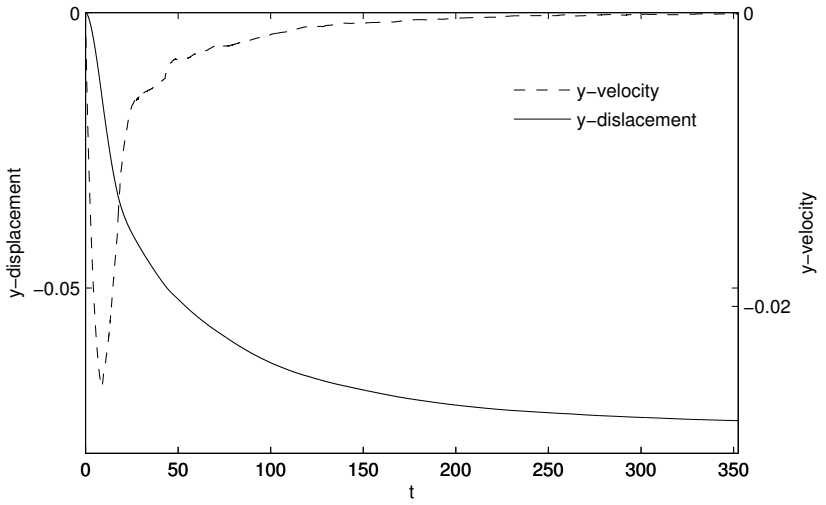

(a)

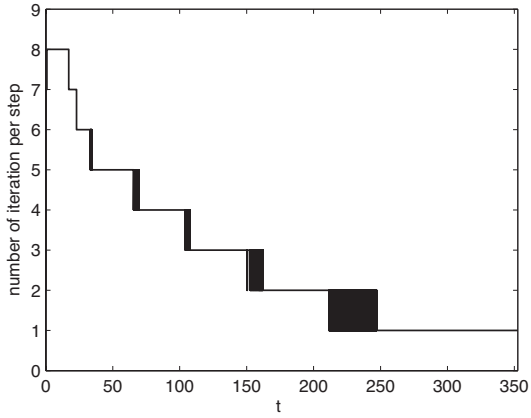

(b)

Figure 4.16: (a) The displacement (solid line) and velocity (dashed line) in the y-direction on the fluid-solid interface at location $(1.6, 0.5)$. (b) The number of iterations required for the strong fluid–structure coupling.

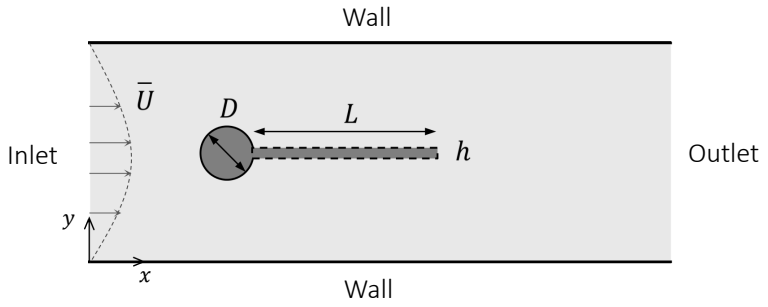

Figure 4.17: The beam behind the circular cylinder in the channel flow.

proposed by Turek and Hron (2006). The flow-induced vibration of the cantilevered beam in the channel is particularly relevant for validation of upper airway simulations, since the flow in the airway induces analogous vibrations of the soft palate, which itself is rigidly attached to the hard palate. Indeed, such air-induced vibration of the soft palate may be an important factor of airway occlusion. Thus, the ability to correctly capture the dynamic motion of the beam in this validation case ensures greater confidence in treating the soft palate motion in the full airway simulations.

In accord with the previous study of Turek and Hron (2006), the diameter of the rigid cylinder is $D = 1$, the channel has width 4.1 and length 11. The velocity at the upper and lower walls are set to zero while a parabolic velocity profile with mean velocity $\bar{U} = 1$ is specified at the inlet of the channel. The outlet is set to have zero velocity gradient. The beam is elastic with initial height $h = 0.2$ and length $L = 3.5$. The center of the cylinder is located at $(2, 2)$, sufficiently far from the inlet and outlet to induce vortex shedding and the fluid–structure interaction behind the cylinder.

For the structure, the non-dimensionalized Young's modulus $E = E^*/(\rho_f \bar{U}^2)$ is chosen to be 1400 and the Poisson ratio is 0.4. The solid mesh has spacing 0.04 and does not conform to the fluid-solid interface, as shown in Figure 4.18. The coefficients for the artificial damping are set to $\alpha = 1.4945 \times 10^{-3}$ and $\beta = 1.4066 \times 10^{-2}$, to ensure 0.5% damping of the second fundamental mode in a vacuum. To promote computational efficiency, iteration in the solid solver is not activated unless the displacements exceed 0.05. The iteration tolerance is set

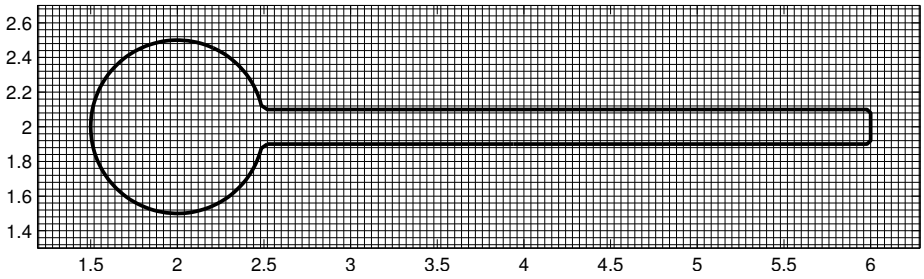

(a)

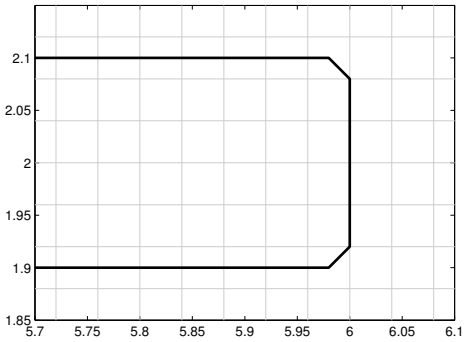

(b)

Figure 4.18: (a) The solid mesh for the elastic beam behind the circular cylinder. (b) The mesh near the tip of the beam.

to be 0.01 and 10^{-4}, for displacements larger than 0.05 and 0.1, respectively.

In the fluid, the Reynolds number is $Re = \rho_f \bar{U} D/\mu_f = 100$. The spacing of the fluid grid is 0.02, one half of the solid mesh spacing. The density ratio between solid and fluid is $\rho_s/\rho_f = 10$. The tolerance for the fluid–structure coupling is set to $\sqrt{2} \times 10^{-4}$, and the relaxation factor is set to 0.4. The time step size is set to be 0.01, which is nearly 1/500 of the resulting oscillation period of the beam.

To analyze the dynamic motion of this fluid–structure interaction problem, we can separately inspect the fundamental frequencies associated with the vortex shedding behind a rigid cylinder in the channel (without beam) and with the free vibration of a cantilever beam in vacuum. The obtained frequency of the vortex shedding is approximately 0.3. On the other hand, for the free vibration of a cantilevered beam in a vacuum, the first three

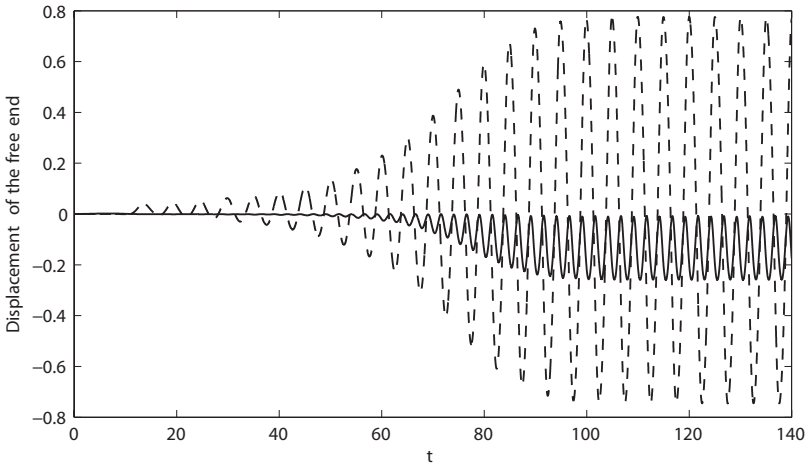

Figure 4.19: The x- (solid line) and y-displacement (dashed line) at the free end of the beam.

theoretical fundamental frequencies are 0.0311, 0.195,and 0.547. Though these fundamental frequencies are slightly modified by the presence of the fluid, they suggest that the second vibration mode of the beam is the one most likely to be excited.

The displacements of the tip of the beam are plotted in Figure 4.19 from $t = 0$ to $t = 140$. It can be observed that the displacements grow from 0 and finally reach stationary periodic oscillations. The frequency of the periodic oscillation is 0.1953, which is very close to the estimated second fundamental frequency of the cantilever beam. The number of iterations for fluid–structure coupling reaches 2, while the number of iterations in the solid remains at 2 after the system reaches periodic oscillations, as shown in Figure 4.17.

The vorticity fields when the beam has maximum deformation are compared with results by Turek and Hron Turek and Hron (2006) in Figure 4.21. The results of the present work exhibit good qualitative agreement with the results of Turek and Hron (2006). For quantitative comparison, the vibration amplitude at the free end of the beam and the Strouhal number are compared with results by Turek and Hron (2006), Bhardwaj and Mittal (2012), and Tian et al. (2014). The Strouhal number of the current work agrees well with the previous studies. The amplitude agrees well with the work of Tian et al. (2014), but has 6.2% and 15.4% discrepancies with the results by Turek and Hron (2006) and Bhardwaj and Mittal (2012), respectively. This may be due to the use of artificial damping in the solid solver or

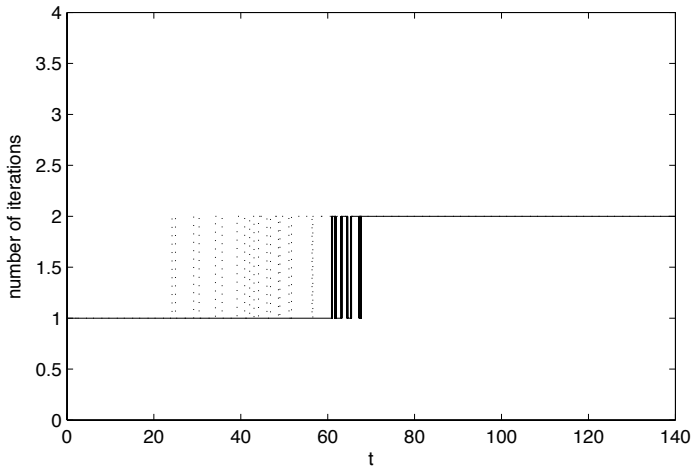

Figure 4.20: The number of iterations for fluid–structure interaction (solid line) and the non-linear solid solver (dashed line).

	Amplitude of the tip	**Strouhal number**
Turek and Hron (2006)	0.83	0.19
Bhardwaj and Mittal (2012)	0.92	0.19
Tian et al. (2014)	0.78	0.19
present work	0.7779	0.1953

Table 4.1: Comparison of the amplitude at the free end of the elastic beam and the Strouhal number with results in previous work.

to the lower resolution of the solid compared with that used in Bhardwaj and Mittal (2012).

4.1.3.3 The Three-Dimensional Simulation of a Cantilevered Plate in the Cross Flow

The FSI solver is tested with the three-dimensional flow past a cantilevered plate. The results will be qualitatively compared with the simulation done by Tian et al. (2014). The dimensions of the plate is shown in the figure 4.22. It is fixed at the bottom side and the top end is free. For the fluid simulation, the domain is in $[0, 10] \times [0, 8] \times [0, 10]$ with the plate

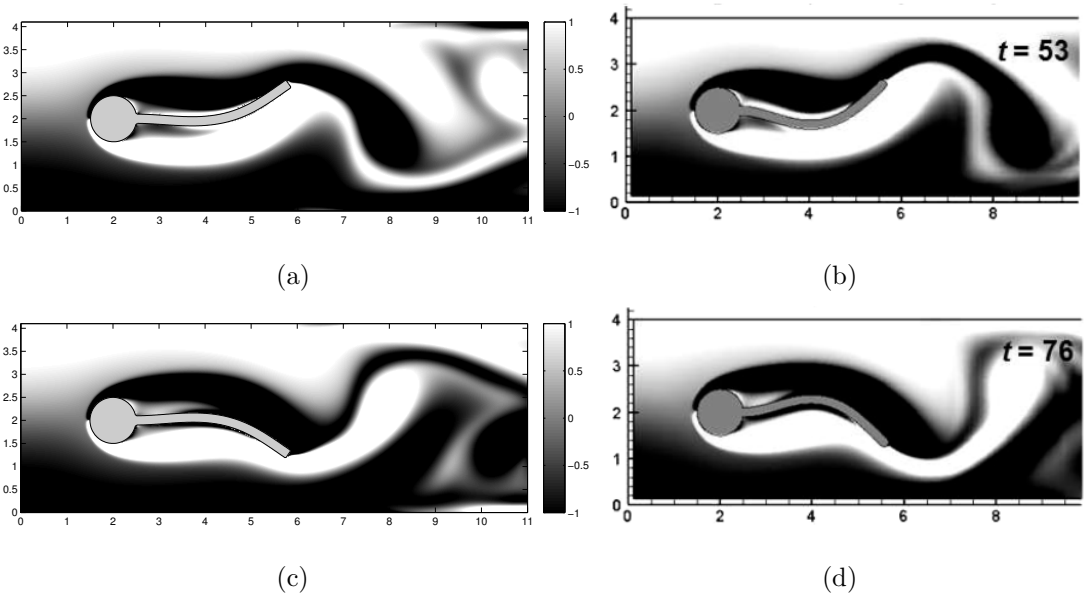

Figure 4.21: The comparison of vorticity contours when the beam reaches the periodic oscillation with maximum y-displacement at the tip of present work (a,b) and results by Bhardwaj and Mittal (2012) (c,d).

locating right at the middle of the rectangular domain. The $Re = 100$ and the density ratio between fluid and solid is $\rho_f/\rho_s = 0.678$. The buoyancy force is not taken into consideration. The domain is decomposed into $100 \times 80 \times 100$ grid cells with grid size 0.1 and time step size 0.001. The inlet at $x = 0$ is set to have uniform flow velocity U. U gradually increases from 0 to 1 and remains constant after reaching 1 (figure 4.23). The outlet boundary condition is imposed on the other boundaries. For the solid, the Young's modulus is $E = 12918.612$, poisson ratio $\nu = 0.4$, and the grid size is set to be 0.1. The artificial damping is introduced to allow only the lower frequency modes to develop. The coefficients in Rayleigh damping are $\alpha = 0.1$, and $\beta = 0.0002$ according to the vibration modes of the plate. The tolerance of the nonlinear iteration is 1×10^{-4}, while for the FSI iteration, the tolerance is 1×10^{-5} and the relaxation parameter is 0.2, chosen according to the density ratio between solid and fluid. The interface is decomposed into 8936 triangle elements as shown in figure 4.24.

The simulation has been conducted for 4000 steps until the plate nearly reaches the steady state. The x-displacement, which is along the flow direction, at the center of the free end is plotted in the figure 4.25. The final deformation of the plate is compared with the result

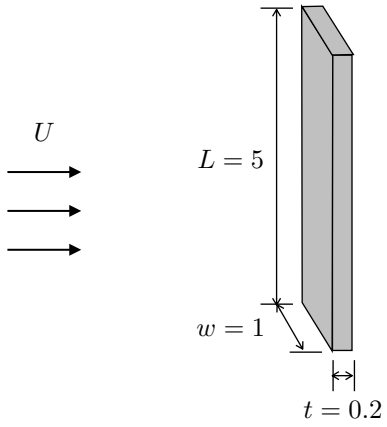

Figure 4.22: The setup of the validation problem of a cantilevered plate in the cross flow.

in Tian et al. (2014) with $Re = 1600$, $E = 19054.9$ and with buoyancy force (figure 4.26). The shape of the deformed plate matches qualitatively with the result by Tian et al.. The streamline near the deformed plate is shown in the figure 4.27.

4.1.4 Scalability Test

The parallel computing is achieved using MPI and PETSc. PETSc provides tools including data structures of distributed vectors and matrices as well as routines of domain partitioning and Krylov method for parallel computing related with solving PDE systems. For the fluid solver, the Distributed Arrays routine helps on the domain decomposition, data communication on the ghost cells, and managing distributed vectors on the structured grids. The poisson equation is solved using it's iterative Krylov subspace method. For the solid solver, since it is not using structured grid, the mapping between the global indices and the local involved indices needs to be established first. After that, PETSc can help on the data scattering and gathering between processors. As to the interface, the redistribution of the interface information between different processors are achieved using MPI sending and receiving routines.

The test problem are the flow in a deformable tube which is fixed at the inlet and outlet.

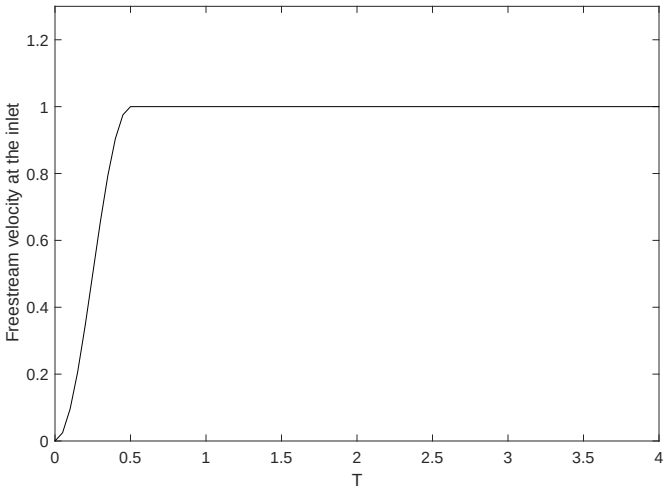

Figure 4.23: The prescribed inlet freestream velocity.

Three kinds of size of test problems are listed in the table 4.2. The tests are conducted on the Hoffman2 Cluster in UCLA Institute for Digital Research and Education (IDRE) with intel E5-2670 processors. At most 64 processors are used.

The results of the runtime in one FSI iteration of these three cases with different number of processor are shown in the figure 4.28. The runtime is nearly inversely proportional to the number of processor, but the speedup is slightly lower with more number of processors. The runtime used by the fluid solver, solid solver and the interface calculation has been plotted separately in the figure 4.29. The simulation time of solving poisson equation is shown in diamond marker, the time used in every nonlinear elasticity iteration is shown in triangle markers, and the runtime in the interface computation is shown in square markers. For most cases, solving poisson equation takes most of the computation time. However, when the number of processor increases, the runtime used in the solid and interface calculation

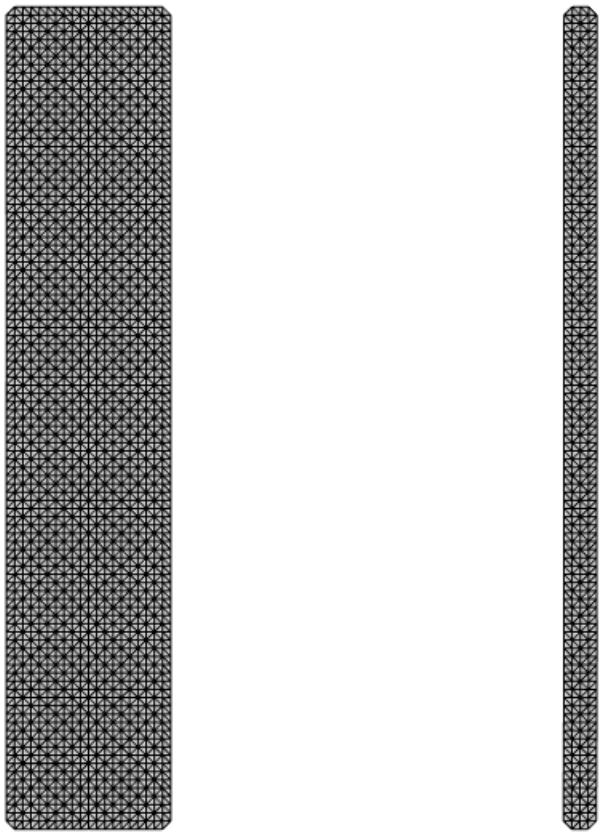

Figure 4.24: The surface of the plate is decomposed into 8936 triangular surface elements. Left: front view. Right: side view.

decrease less and even plateaus at last. The bottle neck of the solid solver is on the update of the governing stiffness matrices and load vector according to the current stress and strain distribution. Constructing the distributed matrices and vectors on more number of processors may deteriorate the performance.

4.2 Simulation Related with Patient-Specific Geometries

In this section, first we will demonstrate that the three-dimensional flow solver, whose methodology was described above in section 2.2, performs well on simplified flows through

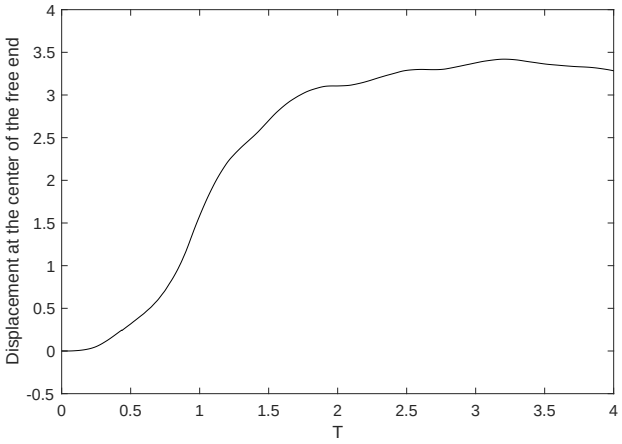

Figure 4.25: The displacement history at the center of the free end.

Table 4.2: The number of fluid grid, solid involved node and interface element used in the scalability test.

	Case 1	Case 2	Case 3
fluid grid	$200 \times 200 \times 300$	$250 \times 250 \times 375$	$320 \times 320 \times 480$
solid involved node:			
x component	19968	33970	64200
y component	19968	33970	64200
z component	19404	34944	62800
interface element	86800	135664	225248

rigid airways obtained by the image processing technique described in chapter 3. Airways from two arbitrarily chosen patients are chosen based on their dissimilarity. Secondly, the tissue deformation will be taken into consideration. The objective in this demonstration is not to simulate the airways under realistic flow conditions nor to compare their behaviors, but rather, to verify that the algorithm performs well with different and complex image-generated geometries.

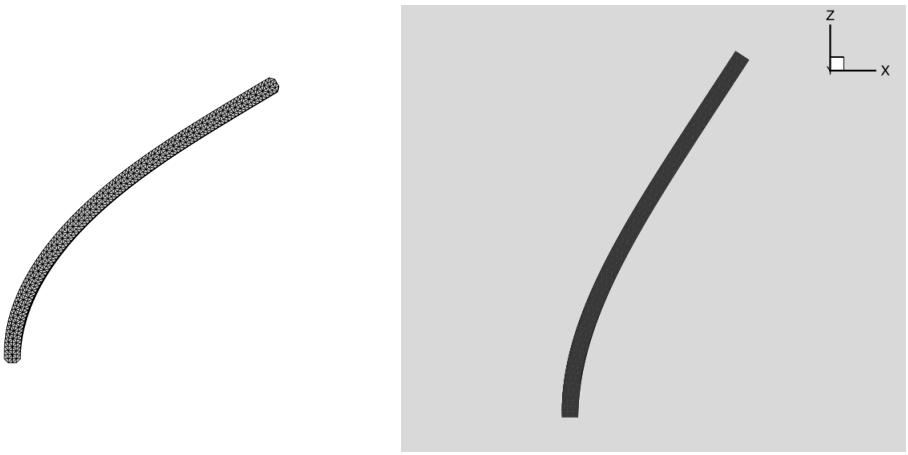

(a) (b)

Figure 4.26: The final deformation of the plate in the cross flow by the present work (a) and the result by Tian et al. with different parameters (b).

4.2.1 Pressure Driven Flow in the Three–Dimensional Patient-Specific Airway Geometry.

In this section, we consider reduced Reynolds number flows in two patient-specific airway geometries, labelled as case A and case B, that are extracted from three-dimensional imaging using the procedure described in Chapter 3. Each airway geometry is embedded in a three-dimensional Cartesian mesh (with axes labelled as x, y, and z, respectively) of uniform grid spacing. The mean flow is driven by pressure difference imposed between the inlet and outlet of the airway, where the fluid region of the signed distance field intersects the boundaries of the computational domain. The streamwise direction of the airway is primarily aligned with the z coordinate axis. The upper boundary plane of the domain intersects the uppermost (i.e. superior) portion of the airway, approximately at the nasopharynx, while the lower boundary plane intersects the lowermost (i.e. inferior) portion, just below the epiglottis. No-slip velocity boundary conditions are specified on all fluid-solid interfaces. The immersed boundary method described in Section 2.2 is used to handle velocity reconstruction adjacent to the irregular interface.

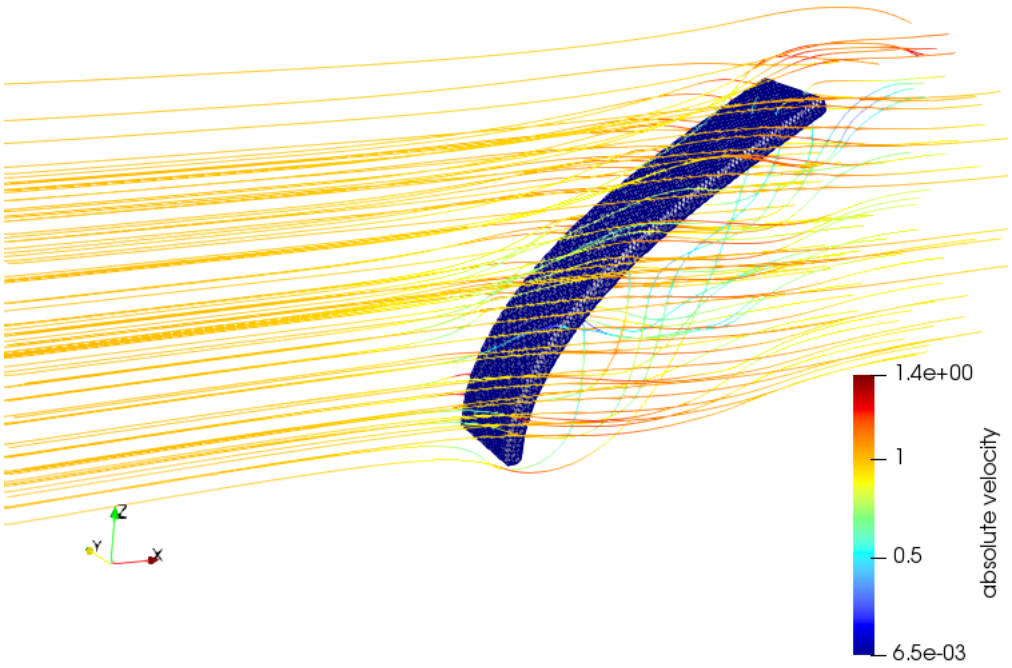

Figure 4.27: The streamlines at T=4. The color of the streamline represents the velocity magnitude.

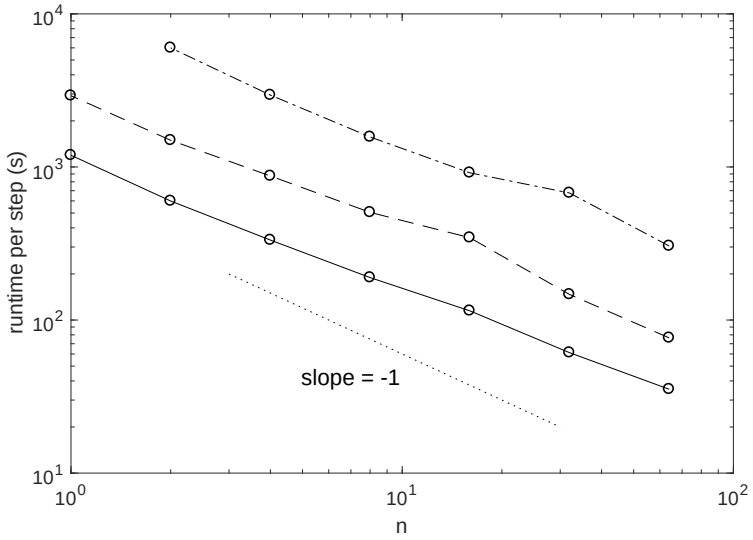

Figure 4.28: The runtime per FSI iteration versus the number of processors with test case 1(solid line), case 2 (dashed line), and case 3 (dot-dash line).

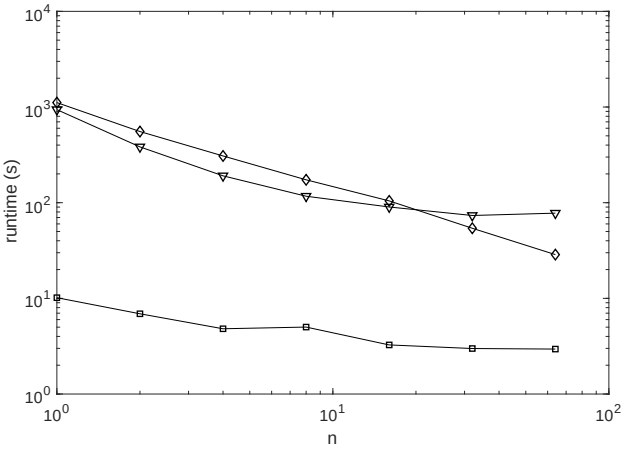

(a)

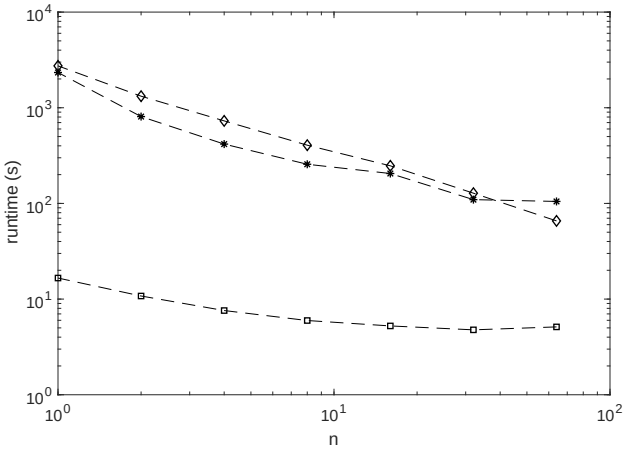

(b)

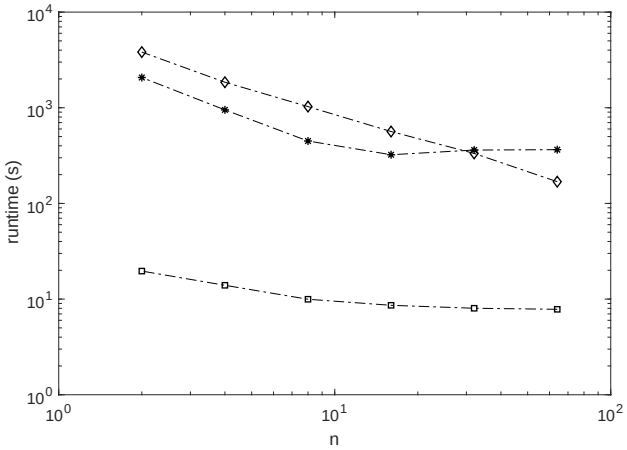

(c)

Figure 4.29: The simulation time of solving poisson equation ($\diamond$), nonlinear elasticity iteration ($\bigtriangledown$) and interface computation ($\square$).

4.2.1.1 Computational Setup

In this preliminary study, the pressure conditions are steady and set to inspiratory conditions (i.e. inhalation), as is typical of previous computational studies of the airway, because of the observed prevalence of airway occlusion in apnea patients during this portion of the breathing cycle.

The non-dimensional pressure boundary conditions are $p = 1$ on the upper boundary and $p = -1$ on the lower boundary. The distance variables are scaled by L, where the z heights of the computational domain are $2.13L$ for Case A and $2.52L$ for Case B. A uniform grid size is used and the time step sizes are adjusted such that the CFL number is maintained approximately at 0.25 throughout the simulations. Density is set uniformly to 1.

Before the pressure difference is imposed on the boundaries, the velocity field is set initially to zero everywhere. The portions of the computational domain in the solid region (with signed distance value of opposite sign to the fluid region) are assigned zero fluid velocity for all times. The simulation's time stepping starts at $t = 0$, when the pressure difference is applied. The flow then evolves toward a fully developed state.

4.2.1.2 Flow features

The simulations of steady flow in the upper airway geometries of patients A and B are each conducted for two Reynolds numbers. The Reynolds number is based on the hydraulic diameter and peak velocity in a representative cross-section. The development of the flow field is indicated by the evolution of (dimensionless) mass flow rate through the airway, defined as

$$q(z) = \int_{\text{fluid}} w \, \mathrm{d}S \tag{4.9}$$

where w is the streamwise velocity component; given a z location, the integration is carried out only in the fluid region in the corresponding $x-y$ plane. The fully developed state of the flow field is determined when q reaches a steady state. The flow rates in these simulations are found to be nearly invariant in the z-direction, indicating that mass is well conserved in

our implementation of the immersed boundary method.

Figure 4.30 depicts the simulation results of the flow fields in the upper airway geometry of patient A. Figure 4.30(a) is the iso-contour of velocity magnitude at selected $x - y$ cross sections at Reynolds number $Re = 29$ with grid size $0.01L$, superimposed with the airway geometry (identified by the zero level-set of the signed distance field). This figure indicates that the immersed boundary method correctly enforces the no-slip boundary conditions on the complex fluid-solid interface. Streamline traces, randomly seeded at upstream locations, are shown in Figure 4.30(b) to visualize the overall flow patterns. The maximum velocity magnitude $|\mathbf{u}| = 0.86$ for case A at $Re = 29$.

We conducted a grid resolution study for this case. Two grid resolutions were tested: the first grid used $134 \times 197 \times 213$ grid cells, while the second grid used $268 \times 394 \times 426$ grid cells. Between the two runs, the fully-developed cross-sectional flow rate differs by 3% (0.0442 and 0.0429, respectively), and the maximum velocity differs by less than 1% (0.86 and 0.857, respectively), indicating that the resolution is adequate for the coarser grid.

It is important to note that this Reynolds number is around 100 times smaller than the Reynolds numbers expected in a real airway during normal inspiration. The purpose of this study is only to report preliminary results; a simulation at real flow conditions would require large-eddy simulation (LES) to model the filtered scales on a grid with practically achievable resolution. In order to appreciate the influence of Reynolds number, the simulation of case A is carried out at somewhat larger (but still low) Reynolds number $Re = 263$. The computational domain has the same size as for the $Re = 29$ case, but the grid spacing is reduced to $0.005L$ in order to obtain convergent computations. Recirculation regions are evident in the flow around the epiglottis, near the lower (inferior) end of the airway, at the higher Reynolds number; however, the flow is still steady. In Figure 4.30(c), the maximum velocity reaches $|\mathbf{u}| = 1.72$.

For case B, the simulations at at $Re = 10$ and $Re = 203$ with grid spacing $0.01L$ and $0.005L$ were conducted. The results are shown in Figure 4.31. The maximum velocity reaches $|\mathbf{u}| = 0.6$ at $Re = 10$ and $|\mathbf{u}| = 1.99$ at $Re = 203$. These two cases with quite different upper

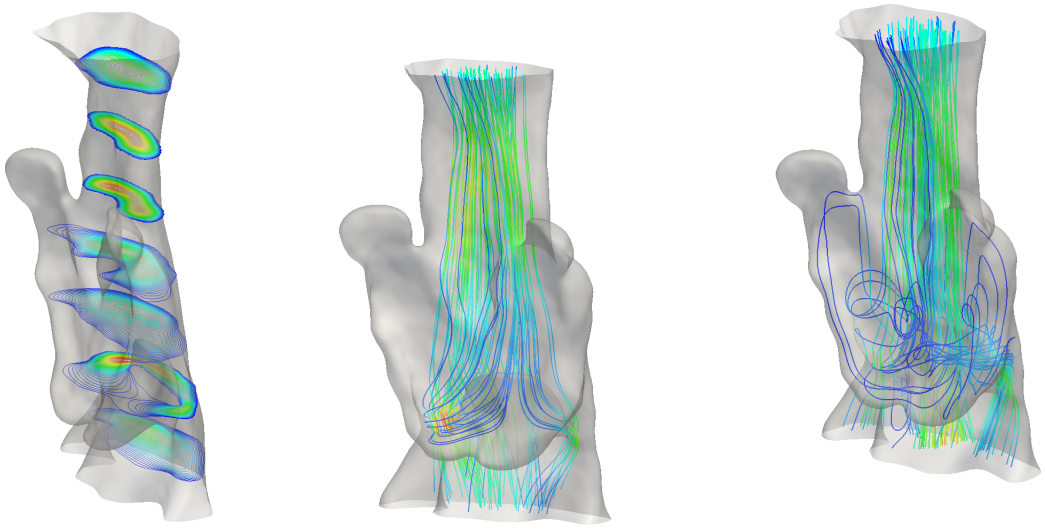

Figure 4.30: Simulation results of case A. (a) Velocity iso-contours at $Re = 29$; contour range extends from 0 (blue) to 0.69 (red). (b), (c) Streamline traces colored by velocity magnitude (red is high, blue is low), at $Re = 29$ and $Re = 268$, respectively.

airway shape we believe are sufficient to demonstrate that our proposed fluid solver can properly deal with a variety of complex airway geometries.

4.2.2 Deformable airway

In this section, the deformation of the tissue surrounding the upper airway is taken into consideration. The soft tissue including tongue, soft palate, pharyngeal wall and fat from the tip of epiglottis to the base of the soft palate is selected as described in the Chapter 3 (figure 4.32). It is worth noting that the real base of the tongue should be at the location connecting to the hyoid bone, which is about 1 cm lower than the tip of the epiglottis. In other word, the extracted tongue geometry will be slightly shorter than the real tongue geometry. The reason of removing some bottom part of the tongue is that the present solid solver does not have the ability to deal with the interaction between epiglottis and airway wall. We chose to assume the epiglottis and the surrounding tissue to be rigid, and not

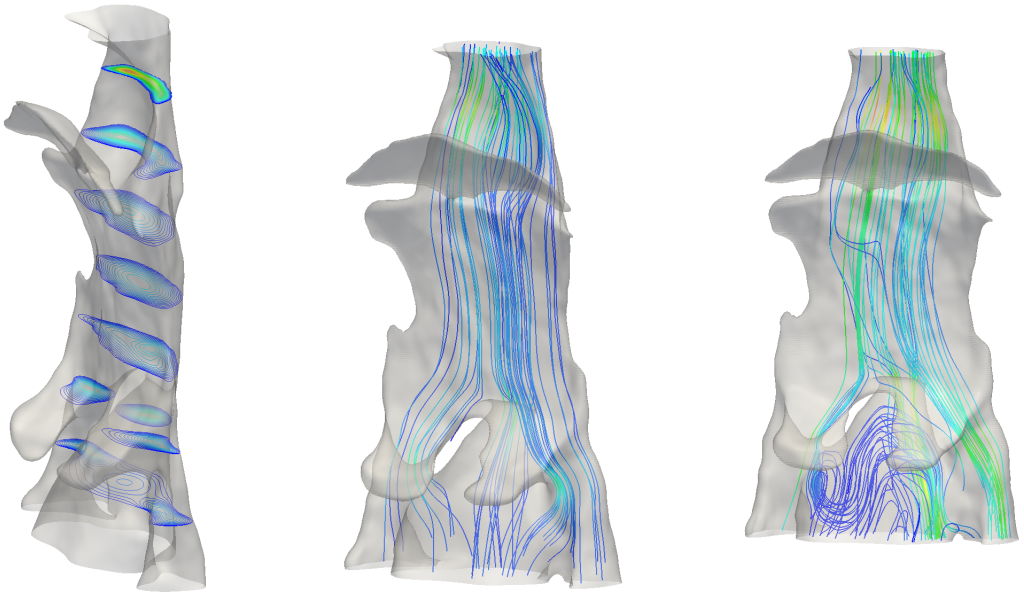

Figure 4.31: Simulation results of case B. (a) Velocity iso-contours at $Re = 10$; The contour range extends from 0 (blue) to 0.6 (red). (b), (c) Streamline traces colored by velocity magnitude (red is high, blue is low), at $Re = 10$ and $Re = 203$, respectively.

taking the nearby tongue tissue and pharyngeal wall into consideration. Moreover, due to that there is still lack of the contact model in the solid solver, the soft palate is set to be connected with the tongue, as shown on the right of figure 4.33. The dimension of the obtained tissue geometry is 5.07 cm (H) $\times$ 4.95 cm (W) $\times$ 7.11 cm (D), while the dimension of the upper airway is 6.84 cm (H) $\times$ 3.93 cm (W) $\times$ 1.26 cm (D).

As to the boundary condition, the setup of boundary conditions in the tissue and flow simulation are shown in the figures 4.34 and 4.35. The part of the airway below the tip of the epiglottis is considered to be fixed. As the matter of this fact, the bottom side of the obtained tissue geometry has to be set to be fixed. Since the base of the soft palate is connecting to the hard palate, the top side of the tissue is also set to be fixed. At the rear side of the upper airway, the pharyngeal wall tissue is connecting to the spine. The deformation at the rear side of the pharyngeal wall should be comparatively smaller than the front side associated with the deformation of the tongue and soft palate, so that it is assumed to be fixed in the simulation. We choose to use a simple straight dividing line to

divide the border of the fixed and FSI boundary condition in the fluid and solid solvers. For the part of the tissue boundary that is not fixed nor FSI interface, it is set to be traction-free.

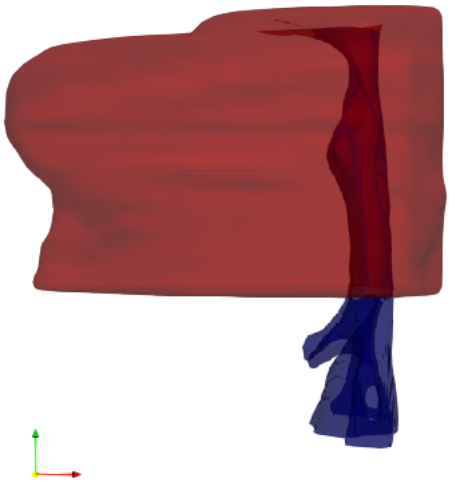

Figure 4.32: The tissue and upper airway geometries in the simulation.

For the simulation parameters, the flow is driven by the constant pressure difference at the inlet and outlet. The pressure at inlet and outlet is 0 Pa and -1.7 Pa. The $Re = 140$, density ratio $\rho_s/\rho_f = 849$, the Young's modules $E = 7539$ Pa, obtained from the result in Cheng et al. (2011), and the poisson ratio $\nu = 0.45$. The grid size of the flow simulation is the same with the resolution of the CT images, which is 0.3 mm, while the grid size in the solid solver is 0.9 mm. The time step size is 2.55×10^{-5} s. There are 5505024 of fluid grids as well as 189759,188697, and 187239 involved x-, y-, z-nodes in solid simulation. The FSI interface has been decomposed into 22336 triangular elements (figure 4.36).

The displacement history at the tip of the soft palate and the displacement field after 5000 steps are shown in the figure 4.37. Because the pressure distribution in the airway gradually decreases from inlet to outlet, and the tissue is fixed on the top and bottom sides, the maximum deformation appears at the posterior side of the tongue but not the soft palate. The obtained displacement is still relatively small and no airway occlusion is observed. The

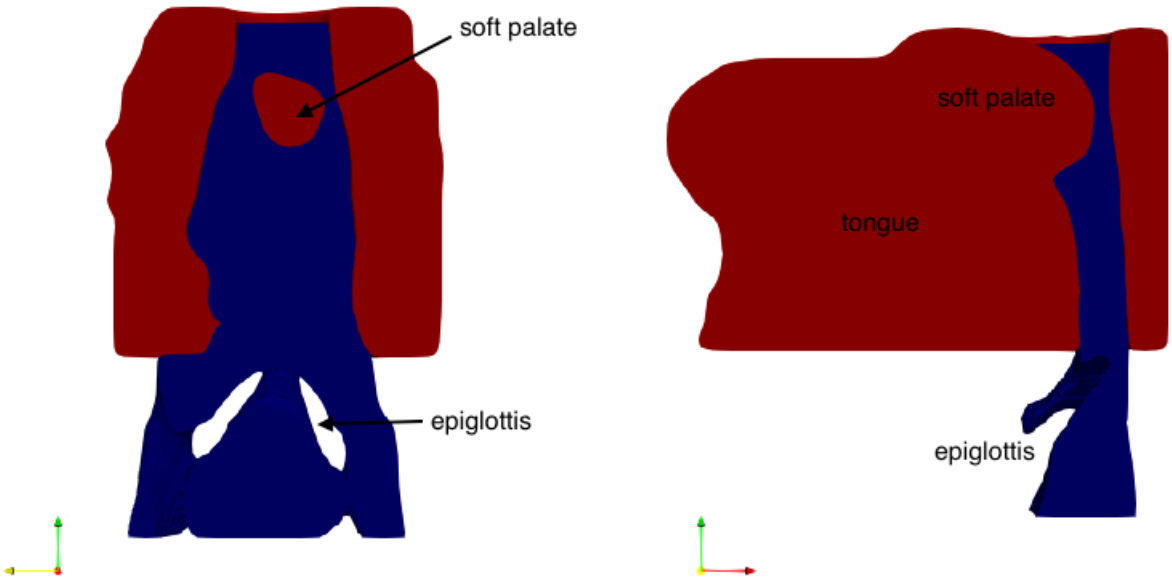

(a) (b)

Figure 4.33: The coronal (left) and sagittal (right) slices of the tissue and upper airway geometries used in the FSI simulation.

flow field obtained after 5000 steps (figure 4.38) is similar to the results obtained in the rigid upper airway simulation.

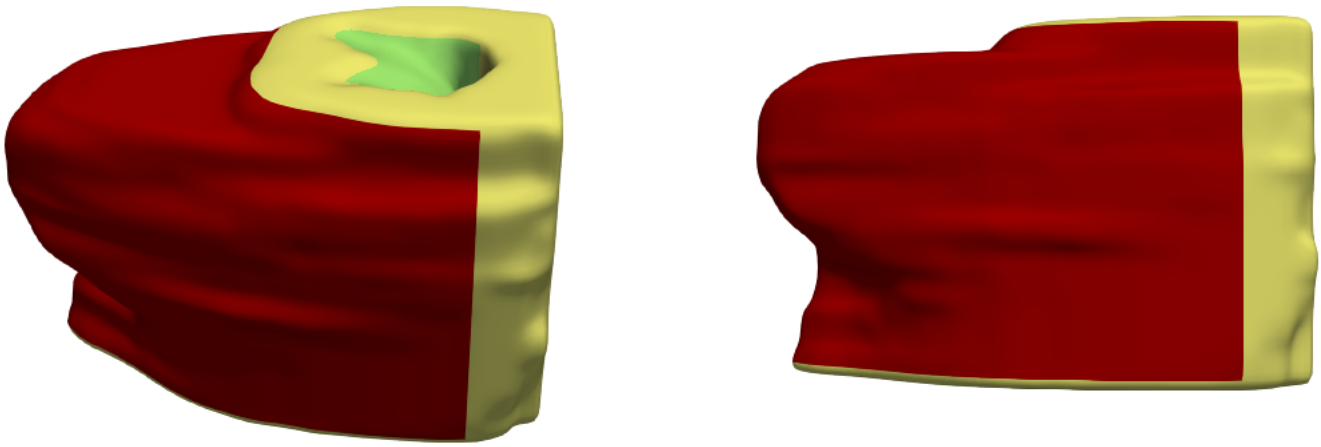

Figure 4.34: The boundary conditions used in the soft tissue simulation. The yellow color represents Dirichlet boundary condition, where the tissue is fixed. The red and green colors indicate the zero traction and the FSI boundary condition.

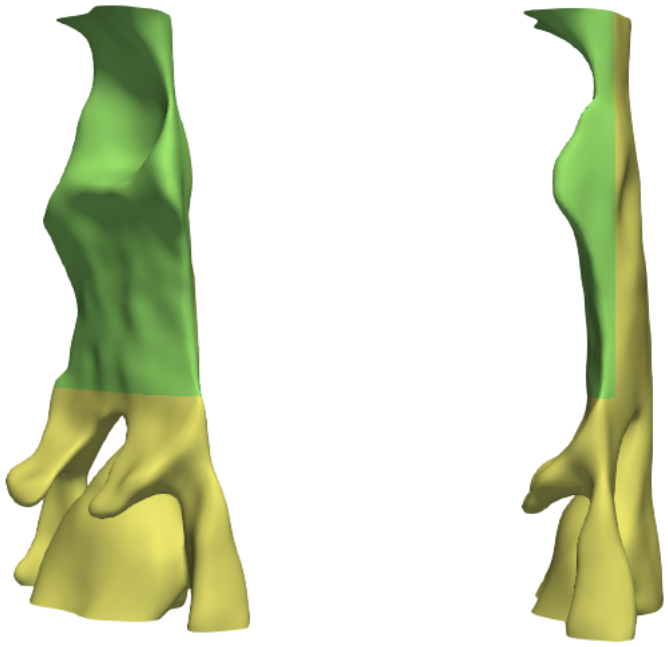

Figure 4.35: The boundary conditions used in the airflow simulation. The yellow color represents Dirichlet boundary condition, where the airway wall is fixed, while the green color indicates the FSI boundary condition.

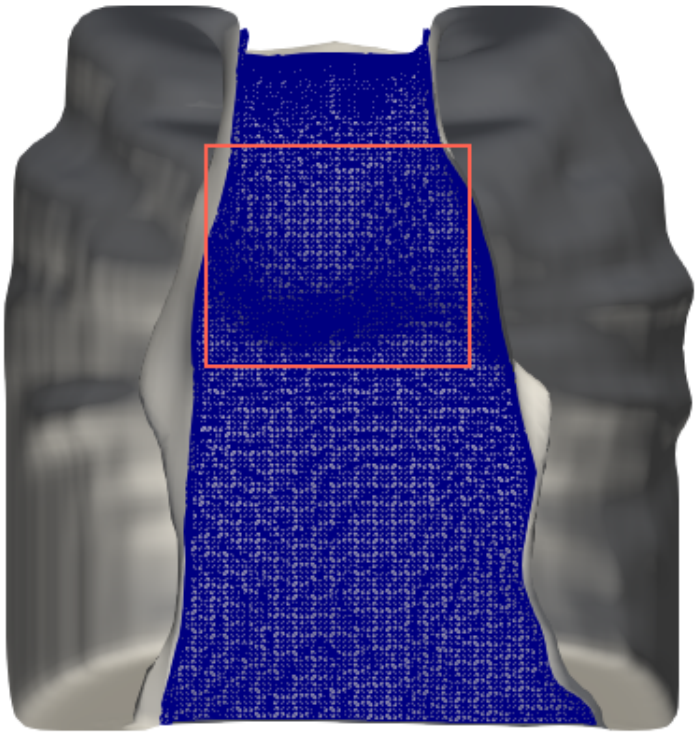

(a)

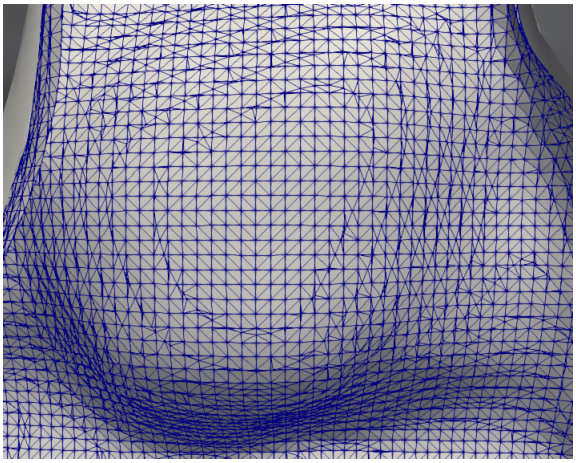

(b)

Figure 4.36: The Lagrangian triangle interface elements on the FSI boundary. The plot (b) is the zoomed plot of the area inside the red rectangle in (a).

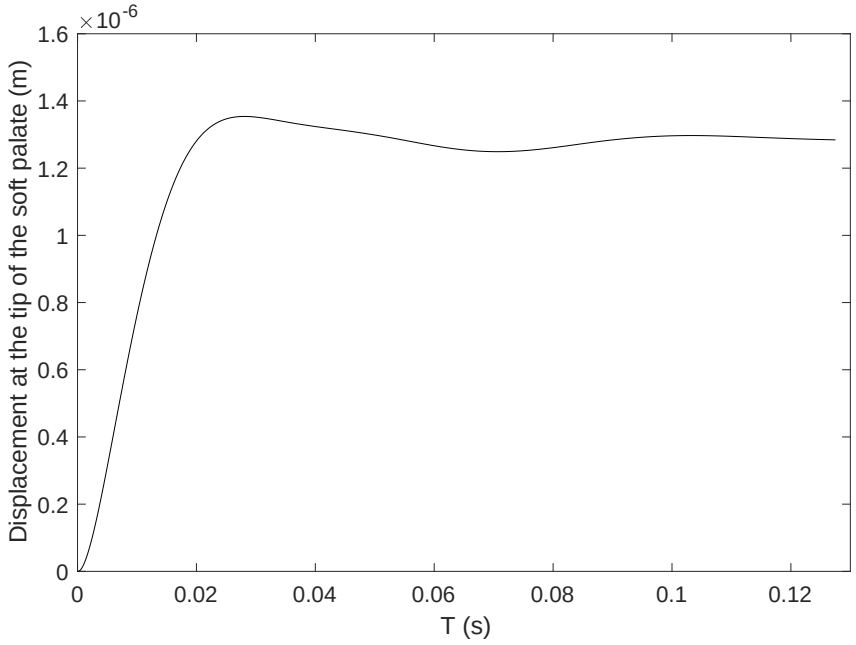

(a)

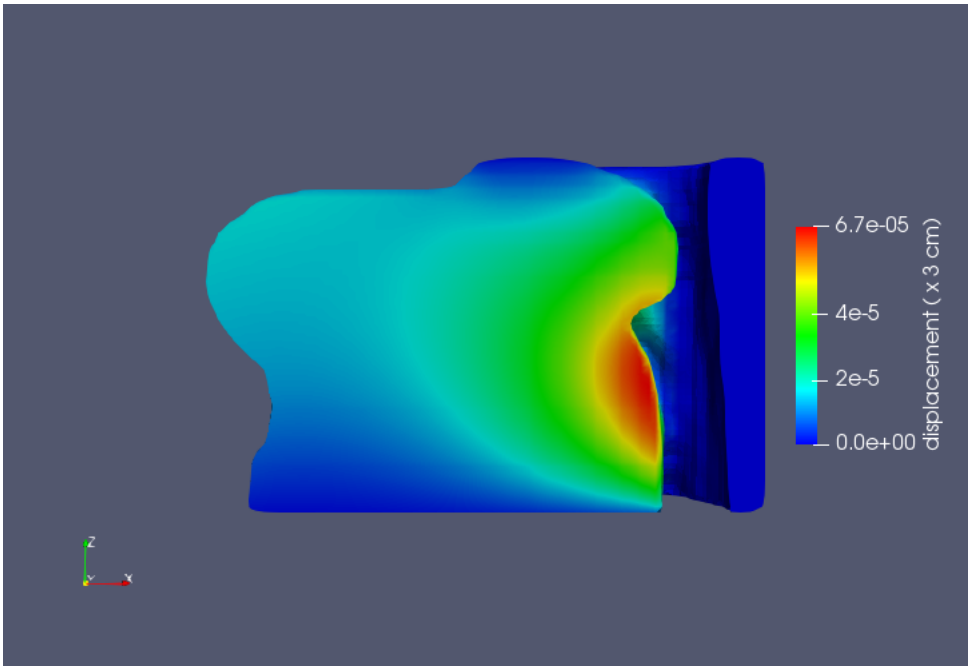

(b)

Figure 4.37: The history of the backward displacement at the tip of the soft palate (left) and the magnitude of the displacement field at the sagittal slice after 5000 steps.

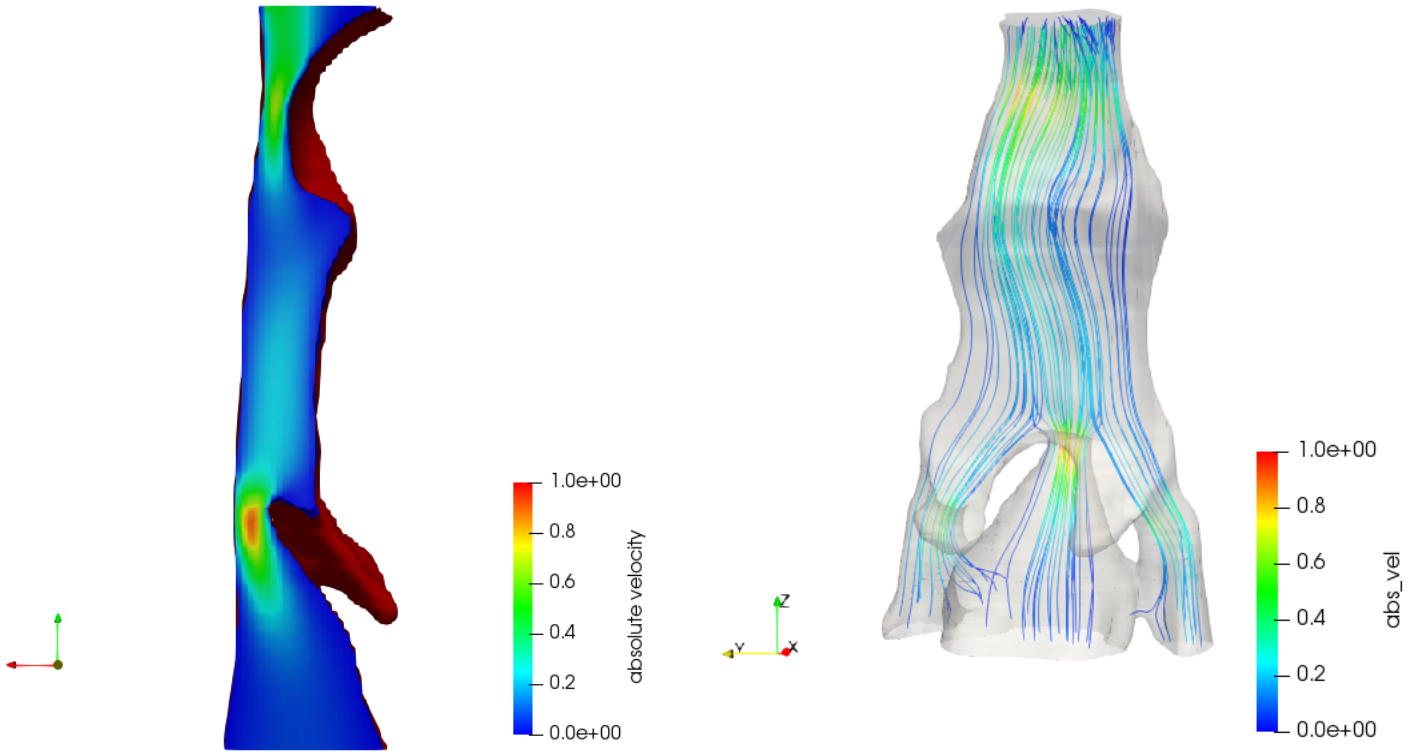

(a) (b)

Figure 4.38: The flow velocity magnitude on the sagittal slice (left) and the streamline (right) after 5000 steps.

CHAPTER 5

Discussion and Future Perspectives

Summary

In this dissertation, the ability of the developed numerical tool using non-body-comformal Cartesian grid with immersed boundary/embedded method to deal with fluid-structure problems has been demonstrated. The fluid field and solid deformation are computed respectively with separate solvers. The fluid and solid domain are decomposed into Cartesian grids with separately chosen grid sizes. The fluid field is solved with the sharp–interface embedded boundary formulation. The existence of the impermeable solid body is represented with the discrete forcing added on the forcing point near the fluid–structure interface. The solver has been proven to have the order of accuracy slightly less than 2^{nd} order. The solid solver combining the nonlinear elasticity finite element formulation and the cut-cell treatment has been successfully developed. The simulation results on the dynamics of a cantilever beam with uniformly distributed load not only shows the abilities of the solver generating the cut–cells from Eulerian signed-distance function, but also demonstrated appropriateness of the nonlinear elasticity formulation for large deformation/rotation. The flow field and solid deformation are solved iteratively until the boundary conditions are satisfied at the interface. This strong coupling algorithm is considered to be more stable than the non-iterative algorithm. The two- and three-dimensional simulation of flow-induced deformation problems with parallel computing have been successfully conducted, and the results show a good agreement with the ones by previous studies. The combination of non-body conforming solvers is novel. It has been proven to be feasible, and this removes much of the inherent challenge to the user in setting up a FSI problem.

To apply the designed numerical tool on the patient-specific upper airway geometries, a procedure has been described to obtained the patient-specific geometry from cone-beam CT scan. The segmentation of tissue and airway structure from CT scans has been performed with ITK-Snap and MATLAB. With the proposed image processing procedures, the obtained data has been transformed into a relatively smooth signed distance field description of the upper airway and the soft tissue geometries. We have shown the capability of the immersed-boundary fluid solver to deal with the three-dimensional flow in the irregular airway geometries obtained from different patients. It has been observed that even though the minimum cross-sectional areas of these two upper airway geometries are at similar location behind the soft palate, their maximum velocity magnitude ended up at very different locations, one behind the soft palate and the other one near the epiglottis. This result suggests that it is not enough to estimate the occlusion site from only the dimension of the static upper airway geometry.

The simulation of airflow-tissue interaction on the obtained upper airway and soft tissue geometry has been conducted with a lower Reynolds number. The flow is driven by the constant pressure difference at inlet (base of soft palate) and outlet (base of epiglottis). Only the fluid-structure interaction at the back of the soft palate and tongue are considered, and all the soft tissue around the airway are considered to be connected with uniform properties. Due to the large density ratio between the solid and fluid, the deformation of the soft tissue is mainly due to the pressure distribution in the airway. The soft palate and tongue are pulled backward due to the negative pressure in the airway. The displacement is relatively small because the inlet pressure is set to be ambient pressure rather than a realistic value lower than ambient pressure. However, the result shows the the ability of the solver dealing with the FSI problem in patient-specific geometries.

Future Work

There still exists a gap between the developed tool and the final desired tool to deal with real flow condition and soft tissue deformation in the patient-specific upper airway geometries.

Following are some suggestions that may help on reduce the gap:

- Improvement on the fluid solver: The fluid solver requires the large-eddy simulation (LES) modeling to enable practical simulations at the larger Reynolds numbers associated with airflow accompanied with adaptive mesh refinement to resolve the flow near the constriction and wall of the upper airway (Vanella et al., 2010). Also, the pressure-type outlet boundary condition should be replaced with an impedance-type condition in order to properly account for the influence of the lower airway and bronchial system; the inlet condition should be time-varying to account for the entire breathing cycle.

- Constitutive law of the soft tissue: The Saint-Venant model used in the simulation is the simplest hyperelastic model, but not the most appropriate one. Other hyperelastic model can be implemented in the solid solver once the partial derivative of the stress with respective to strain can be obtained. Moreover, the living tissues are usually viscoelastic material, where the stresses may depend on not only strain but also on strain rate (Fung, 1993). For numerical calculation, the linear Kelvin-Voigt viscoelastic model is the easiest one to implement. Luo et al. (2008) already used this model in the numerical calculation of FSI around vocal cord for phonation investigation.

- Handling multiple interacting solid objects: The tissues near the upper airway consist of tongue, soft palate, epiglottis, pharyngeal wall, and fat pad. These tissues should be considered as multiple bodies with different properties. The solid solver with cut-cell method is born with the ability of constructing the governing linear system with multiple bodies. It still needs the collision detection algorithm and the contact model in order to identify the location of contact of two bodies and predict the interaction between them. In addition, some part of the tongue, soft palate and pharyngeal wall are composed by muscles. Although muscle can be regarded as passive when OSA occur, the anisotropic material properties still affect the deformation of the muscle. The solid solver needs to equip with ability of tackling material with nonuniform and anisotropic properties.

- FSI coupling scheme: The iterative coupling procedure can be accelerated with dynamic relaxation, which the relaxation parameter varies iteration by iteration. This can be achieved with the use of Aitken or steepest descent relaxation using the interface displacement in previous iterations to estimate the proper relaxation parameter in the next iteration (Küttler and Wall, 2008).

APPENDIX

Finite element formulation for nonlinear analysis in Bathe (2006)

- Total Lagrangian formulation: use the principle of virtual displacement stating the total internal work is equal to the total external work; i.e.

$$\int {}^{t+\Delta t}S_{ij}\delta\, {}^{t+\Delta t}\epsilon_{ij}dV_0 = {}^{t+\Delta t}\mathcal{R} \tag{A.1}$$

where ${}^{t}S_{ij}$ is the 2nd Piola-Kirchhoff stress at time t, ${}^{t}\epsilon_{ij}$ is the Green-Lagrange strain tensor, which is defined as

$${}^{t}\epsilon_{ij} = \frac{1}{2}\left(\frac{\partial\, {}^{t}u_i}{\partial X_j} + \frac{\partial\, {}^{t}u_j}{\partial X_i} + \frac{\partial\, {}^{t}u_k}{\partial X_i}\frac{\partial\, {}^{t}u_k}{\partial X_j}\right) \tag{A.2}$$

and ${}^{t}\mathcal{R}$ is the external virtual work.

- Incremental decomposition: decompose stress and strain to be value obtained at the end of previous step and an incremental value.

$${}^{t+\Delta t}S_{ij} = {}^{t}S_{ij} + S_{ij} \tag{A.3}$$

$${}^{t+\Delta t}\epsilon_{ij} = {}^{t}\epsilon_{ij} + \epsilon_{ij} \tag{A.4}$$

Also, decompose the incremental strain into linear and nonlinear parts:

$$\epsilon_{ij} = e_{ij} + \eta_{ij} \tag{A.5}$$

$$e_{ij} = \frac{1}{2}\left(\frac{\partial u_i}{\partial X_j} + \frac{\partial u_j}{\partial X_i} + \frac{\partial\, {}^{t}u_k}{\partial X_i}\frac{\partial u_k}{\partial X_j} + \frac{\partial u_k}{\partial X_i}\frac{\partial\, {}^{t}u_k}{\partial X_j}\right) \tag{A.6}$$

$$\eta_{ij} = \frac{\partial u_k}{\partial X_i}\frac{\partial u_k}{\partial X_j} \tag{A.7}$$

where the displacement ${}^{t+\Delta t}u_i = {}^{t}u_i + u_i$. The internal virtual work becomes

$$\int {}^{t+\Delta t}S_{ij}\delta\, {}^{t+\Delta t}\epsilon_{ij}dV_0 = \int S_{ij}\delta\epsilon_{ij}dV_0 + \int {}^{t}S_{ij}\left(\delta e_{ij} + \delta\eta_{ij}\right)dV_0 \tag{A.8}$$

Using constitutive equation $S_{ij} = C_{ijrs}\epsilon_{rs}$, then equation 2.43 becomes

$$\int {}^{t+\Delta t}S_{ij}\delta\, {}^{t+\Delta t}\epsilon_{ij}dV_0 = \int C_{ijrs}\epsilon_{rs}\delta\epsilon_{ij}dV_0 + \int {}^{t}S_{ij}\delta e_{ij}dV_0 + \int {}^{t}S_{ij}\delta\eta_{ij}dV_0 \tag{A.9}$$

- Linearization: approximate the $\epsilon_{rs}\delta\epsilon_{ij}$ term to be $e_{rs}\delta e_{ij}$. The governing equation becomes

$$\int C_{ijrs}e_{rs}\delta e_{ij}dV_0 + \int {}^tS_{ij}\delta\eta_{ij}dV_0 \approx {}^{t+\Delta t}\mathcal{R} - \int {}^tS_{ij}\delta e_{ij}dV_0 \tag{A.10}$$

Due to the linearization approximation, iteration is used to reduce the "out-of-balance" of virtual work,

$$\int C_{ijrs}\Delta e_{rs}^{(k)}\delta e_{ij}dV_0 + \int {}^tS_{ij}\delta\Delta\eta_{ij}^{(k)}dV_0 = {}^{t+\Delta t}\mathcal{R} - \int {}^{t+\Delta t}S_{ij}^{(k-1)}\delta\ {}^{t+\Delta t}e_{ij}^{(k-1)}dV_0 \tag{A.11}$$

$${}^{t+\Delta t}u_i^{(k)} = {}^{t+\Delta t}u_i^{(k-1)} + \Delta u_i^{(k)} \tag{A.12}$$

Finite element discretization in 2D

Relate strain $\underline{\epsilon}$, displacement $\underline{u}$ with displacement on nodal points $\underline{\hat{u}}$ using displacement interpolation matrix $\underline{\underline{H}}$ and strain-displacement matrix $\underline{\underline{B}}$:

$$\underline{u}(\underline{x}) = \underline{\underline{H}}(\underline{x})\underline{\hat{u}} \rightarrow \underline{h}_x^T\underline{\hat{u}}_x + \underline{h}_y^T\underline{\hat{u}}_y \tag{A.13}$$

$$\delta\underline{u}(\underline{x}) = \underline{\underline{H}}(\underline{x})\delta\underline{\hat{u}} \tag{A.14}$$

$$\underline{e}(\underline{x}) = \begin{Bmatrix} e_{11} \\ e_{22} \\ 2e_{12} \end{Bmatrix} = \begin{bmatrix} \underline{h}_{x,x}^T & \\ & \underline{h}_{y,y}^T \\ \underline{h}_{x,y}^T & \underline{h}_{y,x}^T \end{bmatrix} \begin{Bmatrix} \underline{\hat{u}}_x \\ \underline{\hat{u}}_y \end{Bmatrix} + \begin{bmatrix} {}^tu_{x,x}\underline{h}_{x,x}^T & {}^tu_{y,x}\underline{h}_{y,x}^T \\ {}^tu_{x,y}\underline{h}_{x,y}^T & {}^tu_{y,y}\underline{h}_{y,y}^T \\ {}^tu_{x,x}\underline{h}_{x,y}^T + {}^tu_{x,y}\underline{h}_{x,x}^T & {}^tu_{y,x}\underline{h}_{y,y}^T + {}^tu_{y,y}\underline{h}_{y,x}^T \end{bmatrix} \begin{Bmatrix} \underline{\hat{u}}_x \\ \underline{\hat{u}}_y \end{Bmatrix}$$

$$\equiv \underline{\underline{B}}_L\underline{\hat{u}} \tag{A.15}$$

$$
{}^{t}S_{ij}\delta\eta_{ij} = \left\{\delta\hat{\underline{u}}_x^T \quad \delta\hat{\underline{u}}_y^T\right\}
\begin{bmatrix} \underline{h}_{x,x} & \underline{h}_{x,y} & & \\ & & \underline{h}_{y,x} & \underline{h}_{y,y} \end{bmatrix}
\begin{bmatrix} \begin{bmatrix} {}^{t}S_{11} & {}^{t}S_{12} \\ {}^{t}S_{21} & {}^{t}S_{22} \end{bmatrix} & \\ & \begin{bmatrix} {}^{t}S_{11} & {}^{t}S_{12} \\ {}^{t}S_{21} & {}^{t}S_{22} \end{bmatrix} \end{bmatrix}
$$

$$
\cdot \begin{bmatrix} \underline{h}_{x,x}^T & \\ \underline{h}_{x,y}^T & \\ & \underline{h}_{y,x}^T \\ & \underline{h}_{y,y}^T \end{bmatrix}
\begin{Bmatrix} \hat{\underline{u}}_x \\ \hat{\underline{u}}_y \end{Bmatrix} = \delta\hat{\underline{u}}^T \underline{\underline{B}}_{NL}^T \; {}^{t}\underline{\underline{S}} \; \underline{\underline{B}}_{NL}\hat{\underline{u}} \tag{A.16}
$$

$$
\int C_{ijrs}e_{rs}\delta e_{ij}dV_0 \rightarrow \delta\hat{\underline{u}}^T \int \underline{\underline{B}}_L^T \underline{\underline{C}} \; \underline{\underline{B}}_L dV_0 \; \hat{\underline{u}} \tag{A.17}
$$

$$
\int {}^{t}S_{ij}\delta\eta_{ij}dV_0 \rightarrow \delta\hat{\underline{u}}^T \int \underline{\underline{B}}_{NL}^T \; {}^{t}\underline{\underline{S}} \; \underline{\underline{B}}_{NL} dV_0 \; \hat{\underline{u}} \tag{A.18}
$$

$$
\int {}^{0}\rho \; {}^{t+\Delta t}\ddot{u}_i\delta u_i dV_0 \rightarrow \; {}^{0}\rho \; \delta\hat{\underline{u}}^T \int \underline{\underline{H}}^T \; \underline{\underline{H}} dV_0 \; {}^{t+\Delta t}\hat{\ddot{\underline{u}}} \tag{A.19}
$$

The governing equation for dynamics analysis after discretization becomes:

$$
\begin{aligned}
&\delta\hat{\underline{u}}^T \left[{}^{0}\rho \int \underline{\underline{H}}^T \; \underline{\underline{H}} dV_0 \; {}^{t+\Delta t}\hat{\ddot{\underline{u}}} + \int \underline{\underline{B}}_L^T \underline{\underline{C}} \; \underline{\underline{B}}_L dV_0 \; \hat{\underline{u}} + \int \underline{\underline{B}}_{NL}^T \; {}^{t}\underline{\underline{S}} \; \underline{\underline{B}}_{NL} dV_0 \; \hat{\underline{u}} \right] \\
&= \delta\hat{\underline{u}}^T \left[{}^{t+\Delta t}\underline{\underline{R}} + \int \underline{\underline{B}}_L^T \; {}^{t}\underline{\underline{S}} \; dV_0 \right]
\end{aligned} \tag{A.20}
$$

The $\delta\hat{\underline{u}}^T$ can be eliminated on both sides,

$$
{}^{0}\rho \int \underline{\underline{H}}^T \; \underline{\underline{H}} dV_0 \; {}^{t+\Delta t}\hat{\ddot{\underline{u}}} + \int \underline{\underline{B}}_L^T \underline{\underline{C}} \; \underline{\underline{B}}_L dV_0 \; \hat{\underline{u}} + \int \underline{\underline{B}}_{NL}^T \; {}^{t}\underline{\underline{S}} \; \underline{\underline{B}}_{NL} dV_0 \; \hat{\underline{u}} = {}^{t+\Delta t}\underline{\underline{R}} + \int \underline{\underline{B}}_L^T \; {}^{t}\underline{\underline{S}} \; dV_0 \tag{A.21}
$$

The nonlinear stiffness matrix thus becomes:

$$\delta\underline{\hat{u}}^T \underline{\underline{B}}_{NL}^T \, {}^t\underline{\underline{S}} \, \underline{\underline{B}}_{NL}\underline{\hat{u}} \equiv \delta\underline{\hat{u}}^T \underline{\underline{K}}_{NL}\underline{\hat{u}}$$

$$= \begin{Bmatrix} \delta\hat{u}_x \\ \delta\hat{u}_y \end{Bmatrix}^T \begin{bmatrix} h_{x,x} & h_{x,y} & & \\ & & h_{y,x} & h_{y,y} \end{bmatrix} \begin{bmatrix} {}^tS_{11} & {}^tS_{12} & & \\ {}^tS_{21} & {}^tS_{22} & & \\ & & {}^tS_{11} & {}^tS_{12} \\ & & {}^tS_{21} & {}^tS_{22} \end{bmatrix} \begin{bmatrix} {h_{x,x}}^T & \\ {h_{x,y}}^T & \\ & {h_{y,x}}^T \\ & {h_{y,y}}^T \end{bmatrix} \begin{Bmatrix} \hat{u}_x \\ \hat{u}_y \end{Bmatrix}$$

$$= \begin{Bmatrix} \delta\hat{u}_x \\ \delta\hat{u}_y \end{Bmatrix}^T \begin{bmatrix} h_{x,x}{h_{x,x}}^T S_{11} + h_{x,y}{h_{x,y}}^T S_{22} + \left(h_{x,y}{h_{x,x}}^T + h_{x,x}{h_{x,y}}^T\right) S_{12} & 0 \\ 0 & h_{y,x}{h_{y,x}}^T S_{11} + h_{y,y}{h_{y,y}}^T S_{22} + \left(h_{y,y}{h_{y,x}}^T + h_{y,x}{h_{y,y}}^T\right) S_{12} \end{bmatrix} \begin{Bmatrix} \hat{u}_x \\ \hat{u}_y \end{Bmatrix} \tag{A.22}$$

Also, the linear stiffness matrix is then:

$$\delta\underline{\hat{u}}^T \underline{\underline{B}}_L^T \underline{\underline{C}} \, \underline{\underline{B}}_L\underline{\hat{u}} \equiv \delta\underline{\hat{u}}^T \underline{\underline{K}}_L\underline{\hat{u}}$$

$$= \begin{Bmatrix} \delta\hat{u}_x \\ \delta\hat{u}_y \end{Bmatrix}^T \begin{bmatrix} (1+u_{x,x})\, h_{x,x} & u_{x,y}h_{x,y} & (1+u_{x,x})\, h_{x,y} + u_{x,y}h_{x,x} \\ u_{y,x}h_{y,x} & (1+u_{y,y})\, h_{y,y} & (1+u_{y,y})\, h_{y,x} + u_{y,x}h_{y,y} \end{bmatrix} \begin{bmatrix} \lambda+2\mu & \lambda & 0 \\ \lambda & \lambda+2\mu & 0 \\ 0 & 0 & \mu \end{bmatrix}$$

$$\cdot \begin{bmatrix} (1+u_{x,x})\, {h_{x,x}}^T & u_{y,x}{h_{y,x}}^T \\ u_{x,y}{h_{x,y}}^T & (1+u_{y,y})\, {h_{y,y}}^T \\ (1+u_{x,x})\, {h_{x,y}}^T + u_{x,y}{h_{x,x}}^T & (1+u_{y,y})\, {h_{y,x}}^T + u_{y,x}{h_{y,y}}^T \end{bmatrix} \begin{Bmatrix} \hat{u}_x \\ \hat{u}_y \end{Bmatrix} \tag{A.23}$$

The submatrices compoments of the linear stiffness matrix are respectively

$$\begin{aligned} K_{L11} = {} & \left[(1+u_{x,x})^2 (\lambda+2\mu) + \mu {u_{x,y}}^2\right] h_{x,x}{h_{x,x}}^T \\ & + \left[\mu(1+u_{x,x})^2 + (\lambda+2\mu)\, {u_{x,y}}^2\right] h_{x,y}{h_{x,y}}^T \\ & + \left[(\lambda+\mu)\, u_{x,y}\,(1+u_{x,x})\right]\left[h_{x,y}{h_{x,x}}^T + h_{x,x}{h_{x,y}}^T\right] \end{aligned} \tag{A.24}$$

$$\begin{aligned} K_{L12} = K_{L21}^T = {} & \left[(1+u_{x,x})\,(\lambda+2\mu)\, u_{y,x} + \mu u_{x,y}\,(1+u_{y,y})\right] h_{y,x}{h_{x,x}}^T \\ & + \left[\lambda\,(1+u_{x,x})\,(1+u_{y,y}) + \mu u_{x,y}u_{y,x}\right] h_{y,y}{h_{x,x}}^T \\ & + \left[\mu\,(1+u_{x,x})\,(1+u_{y,y}) + \lambda u_{x,y}u_{y,x}\right] h_{y,x}{h_{x,y}}^T \\ & + \left[\mu\,(1+u_{x,x})\, u_{y,x} + (\lambda+2\mu)\, u_{x,y}\,(1+u_{y,y})\right] h_{y,y}{h_{x,y}}^T \end{aligned} \tag{A.25}$$

$$
\begin{aligned}
K_{L22} = & \left[(\lambda+2\mu)\left(1+u_{y,y}\right)^2 + \mu {u_{y,x}}^2\right] h_{y,y} {h_{y,y}}^T \\
& + \left[(\lambda+2\mu){u_{y,x}}^2 + \mu(1+u_{y,y})^2\right] h_{y,x} {h_{y,x}}^T \\
& + (\lambda+\mu)\left(1+u_{y,y}\right) u_{y,x}\left[h_{y,x}{h_{y,y}}^T + h_{y,y}{h_{y,x}}^T\right]
\end{aligned} \tag{A.26}
$$

The load vector is then,

$$
\begin{aligned}
& \delta\underline{\hat{u}}^T \underline{\underline{B}}_L^T \, {}^t\underline{\underline{S}} \equiv \delta\underline{\hat{u}}^T \underline{\underline{F}} \\
& = \left\{ \begin{array}{c} \delta\hat{u}_x \\ \delta\hat{u}_y \end{array} \right\}^T \left[\begin{array}{ccc} \left(1+u_{x,x}\right) h_{x,x} & u_{x,y} h_{x,y} & \left(1+u_{x,x}\right) h_{x,y} + u_{x,y} h_{x,x} \\ u_{y,x} h_{y,x} & \left(1+u_{y,y}\right) h_{y,y} & \left(1+u_{y,y}\right) h_{y,x} + u_{y,x} h_{y,y} \end{array} \right] \left[\begin{array}{c} S_{11} \\ S_{22} \\ S_{12} \end{array} \right] \\
& = \left\{ \begin{array}{c} \delta\hat{u}_x \\ \delta\hat{u}_y \end{array} \right\}^T \left[\begin{array}{c} \left[\left(1+u_{x,x}\right) S_{11} + S_{12} u_{x,y}\right] h_{x,x} + \left[S_{22} u_{x,y} + S_{12}\left(1+u_{x,x}\right)\right] h_{x,y} \\ \left[S_{11} u_{y,x} + S_{12}\left(1+u_{y,y}\right)\right] h_{y,x} + \left[S_{22}\left(1+u_{y,y}\right) + S_{12} u_{y,x}\right] h_{y,y} \end{array} \right]
\end{aligned} \tag{A.27}
$$

The stress and displacement gradient are calculated according to the from the last iteration. The details of these calculation will be described in the Cut-Cell FEM implementation report.

Finite element discretization in 3D

Extending to 3D, the z component is taken into consideration:

$$
\underline{u}(\underline{x}) = \underline{\underline{H}}(\underline{x})\underline{\hat{u}} \rightarrow \underline{h}_x^T \underline{\hat{u}}_x + \underline{h}_y^T \underline{\hat{u}}_y + \underline{h}_z^T \underline{\hat{u}}_z \tag{A.28}
$$

The strain, which has 6 components in 3D, can also be related to the displacement vector by strain-displacement matrix $\underline{\underline{B}}$:

$$\underline{e}(\underline{x}) = \begin{Bmatrix} e_{11} \\ e_{22} \\ e_{33} \\ 2e_{12} \\ 2e_{23} \\ 2e_{13} \end{Bmatrix} = \begin{bmatrix} \underline{h}_{x,x}^T & & \\ & \underline{h}_{y,y}^T & \\ & & \underline{h}_{y,y}^T \\ \underline{h}_{x,y}^T & \underline{h}_{y,x}^T & \\ & \underline{h}_{y,z}^T & \underline{h}_{z,y}^T \\ \underline{h}_{x,z}^T & & \underline{h}_{z,x}^T \end{bmatrix} \begin{Bmatrix} \hat{\underline{u}}_x \\ \hat{\underline{u}}_y \\ \hat{\underline{u}}_z \end{Bmatrix}$$

$$+ \begin{bmatrix} & {}^t u_{x,x} \underline{h}_{x,x}^T & & {}^t u_{y,x} \underline{h}_{y,x}^T & & {}^t u_{z,x} \underline{h}_{z,x}^T \\ & {}^t u_{x,y} \underline{h}_{x,y}^T & & {}^t u_{y,y} \underline{h}_{y,y}^T & & {}^t u_{z,y} \underline{h}_{z,y}^T \\ & {}^t u_{x,z} \underline{h}_{x,z}^T & & {}^t u_{y,z} \underline{h}_{y,z}^T & & {}^t u_{z,z} \underline{h}_{z,z}^T \\ {}^t u_{x,x} \underline{h}_{x,y}^T + & {}^t u_{x,y} \underline{h}_{x,x}^T & {}^t u_{y,x} \underline{h}_{y,y}^T + & {}^t u_{y,y} \underline{h}_{y,x}^T & {}^t u_{z,x} \underline{h}_{z,y}^T + & {}^t u_{z,y} \underline{h}_{z,x}^T \\ {}^t u_{x,y} \underline{h}_{x,z}^T + & {}^t u_{x,z} \underline{h}_{x,y}^T & {}^t u_{y,z} \underline{h}_{y,y}^T + & {}^t u_{y,y} \underline{h}_{y,z}^T & {}^t u_{z,z} \underline{h}_{z,y}^T + & {}^t u_{z,y} \underline{h}_{z,z}^T \\ {}^t u_{x,x} \underline{h}_{x,z}^T + & {}^t u_{x,z} \underline{h}_{x,x}^T & {}^t u_{y,x} \underline{h}_{y,z}^T + & {}^t u_{y,z} \underline{h}_{y,x}^T & {}^t u_{z,x} \underline{h}_{z,z}^T + & {}^t u_{z,z} \underline{h}_{z,x}^T \end{bmatrix} \begin{Bmatrix} \hat{\underline{u}}_x \\ \hat{\underline{u}}_y \\ \hat{\underline{u}}_z \end{Bmatrix} \tag{A.29}$$

$$\equiv \underline{\underline{B}}_L \hat{\underline{u}}$$

The resulting stiffness submatrices,

$$\underline{\underline{K}}_L = \begin{bmatrix} K_{L11} & K_{L12} & K_{L13} \\ {K_{L12}}^T & K_{L22} & K_{L23} \\ {K_{L13}}^T & K_{L23}^T & K_{L33} \end{bmatrix} \tag{A.30}$$

,and

$$\underline{\underline{K}}_{NL} = \begin{bmatrix} K_{NL11} & & \\ & K_{NL22} & \\ & & K_{NL33} \end{bmatrix} \tag{A.31}$$

Th diagonal and off-diagonal stiffness submatrices can be written as (without loss of generalty, listing K_{L11},K_{L12} and K_{NL11})

$$\begin{aligned}
K_{L11} = & \left[(\lambda+2\mu)\left(1+u_{x,x}\right)^2+\mu {u_{x,y}}^2+\mu {u_{x,z}}^2\right] h_{x,x}{h_{x,x}}^T \\
& + \left[\mu(1+u_{x,x})^2+(\lambda+2\mu){u_{x,y}}^2+\mu {u_{x,z}}^2\right] h_{x,y}{h_{x,y}}^T \\
& + \left[\mu(1+u_{x,x})^2+\mu {u_{x,y}}^2+(\lambda+2\mu){u_{x,z}}^2\right] h_{x,z}{h_{x,z}}^T \\
& + \left[(\lambda+\mu)\,u_{x,y}\left(1+u_{x,x}\right)\right]\left(h_{x,y}{h_{x,x}}^T+h_{x,x}{h_{x,y}}^T\right) \\
& + \left[(\lambda+\mu)\,u_{x,z}\left(1+u_{x,x}\right)\right]\left(h_{x,z}{h_{x,x}}^T+h_{x,x}{h_{x,z}}^T\right) \\
& + \left[(\lambda+\mu)\,u_{x,y}u_{x,z}\right] \qquad \left(h_{x,y}{h_{x,z}}^T+h_{x,z}{h_{x,y}}^T\right)
\end{aligned} \tag{A.32}$$

$$\begin{aligned}
K_{L12} = & \left[(\lambda+2\mu)\,u_{y,x}\left(1+u_{x,x}\right)+\mu u_{x,y}\left(1+u_{y,y}\right)+\mu u_{x,z}u_{y,z}\right] h_{x,x}{h_{y,x}}^T \\
& + \left[\mu u_{y,x}\left(1+u_{x,x}\right)+(\lambda+2\mu)\,u_{x,y}\left(1+u_{y,y}\right)+\mu u_{x,z}u_{y,z}\right] h_{x,y}{h_{y,y}}^T \\
& + \left[\mu u_{y,x}\left(1+u_{x,x}\right)+\mu u_{x,y}\left(1+u_{y,y}\right)+(\lambda+2\mu)\,u_{x,z}u_{y,z}\right] h_{x,z}{h_{y,z}}^T \\
& + \left[\lambda\left(1+u_{x,x}\right)\left(1+u_{y,y}\right)+\mu u_{x,y}u_{y,x}\right]\left(h_{x,x}{h_{y,y}}^T+h_{y,y}{h_{x,x}}^T\right) \\
& + \left[\lambda\left(1+u_{x,x}\right)u_{y,z}+\mu u_{x,z}u_{y,x}\right] \qquad \left(h_{x,x}{h_{y,z}}^T+h_{y,z}{h_{x,x}}^T\right) \\
& + \left[\lambda u_{x,y}u_{y,x}+\mu\left(1+u_{x,x}\right)\left(1+u_{y,y}\right)\right]\left(h_{x,y}{h_{y,x}}^T+h_{y,x}{h_{x,y}}^T\right) \\
& + \left[\lambda u_{x,y}u_{y,z}+\mu\left(1+u_{y,y}\right)u_{x,z}\right] \qquad \left(h_{x,y}{h_{y,z}}^T+h_{y,z}{h_{x,y}}^T\right) \\
& + \left[\lambda u_{x,z}u_{y,x}+\mu\left(1+u_{x,x}\right)u_{y,z}\right] \qquad \left(h_{x,z}{h_{y,x}}^T+h_{y,x}{h_{x,z}}^T\right) \\
& + \left[\lambda\left(1+u_{y,y}\right)u_{x,z}+\mu u_{x,y}u_{y,z}\right] \qquad \left(h_{x,z}{h_{y,y}}^T+h_{y,y}{h_{x,z}}^T\right)
\end{aligned} \tag{A.33}$$

$$\begin{aligned}
K_{NL11} = & S_{11}h_{x,x}{h_{x,x}}^T+S_{22}h_{x,y}{h_{x,y}}^T+S_{33}h_{x,z}{h_{x,z}}^T \\
& + S_{12}\left(h_{x,y}{h_{x,x}}^T+h_{x,x}{h_{x,y}}^T\right) \\
& + S_{13}\left(h_{x,z}{h_{x,x}}^T+h_{x,x}{h_{x,z}}^T\right) \\
& + S_{23}\left(h_{x,y}{h_{x,z}}^T+h_{x,z}{h_{x,y}}^T\right)
\end{aligned} \tag{A.34}$$

The subvector of the load vector $\underline{F}$

$$
\begin{aligned}
F_1 = & \left[\left(1+u_{x,x}\right) S_{11} + u_{x,y} S_{12} + u_{x,z} S_{13}\right] {h_{x,x}}^T \\
& + \left[\left(1+u_{x,x}\right) S_{21} + u_{x,y} S_{22} + u_{x,z} S_{23}\right] {h_{x,y}}^T \\
& + \left[\left(1+u_{x,x}\right) S_{31} + u_{x,y} S_{32} + u_{x,z} S_{33}\right] {h_{x,z}}^T
\end{aligned} \tag{A.35}
$$

Other parts of the stiffness submatrices have similar expression. To get the formulation of K_{ij}, for the shape functions, just change the $h_{x,m}{h_{x,n}}^T$ or $h_{x,m}{h_{y,n}}^T$ in above equations to $h_{i,m}{h_{j,n}}^T$. Also, for the displacement gradient, change the $u_{x,m}u_{x,n}$ or $u_{x,m}u_{y,n}$ to $u_{i,m}u_{j,n}$. The terms associated to normal displacement gradients $u_{i,i}$ should then modified to $1+u_{i,i}$. Similarly, to get other load subvectors F_i, change ${h_{x,n}}^T$ to ${h_{i,n}}^T$ and $u_{x,m}$ to $u_{i,m}$.

BIBLIOGRAPHY

Zachary Abramson, Srinivas Susarla, Meredith August, Maria Troulis, and Leonard Kaban. Three-dimensional computed tomographic analysis of airway anatomy in patients with obstructive sleep apnea. *Journal of Oral and Maxillofacial Surgery*, 68(2):354–362, 2010.

Harold P Adams, Gregory del Zoppo, Mark J Alberts, Deepak L Bhatt, Lawrence Brass, Anthony Furlan, Robert L Grubb, Randall T Higashida, Edward C Jauch, Chelsea Kidwell, et al. Guidelines for the early management of adults with ischemic stroke a guideline from the american heart association/american stroke association stroke council, clinical cardiology council, cardiovascular radiology and intervention council, and the atherosclerotic peripheral vascular disease and quality of care outcomes in research interdisciplinary working groups: The american academy of neurology affirms the value of this guideline as an educational tool for neurologists. *Circulation*, 115(20):e478–e534, 2007.

Tero Aittokallio, Mats Gyllenberg, and Olli Polo. A model of a snorer's upper airway. *Mathematical biosciences*, 170(1):79–90, 2001.

Indu Ayappa and David M Rapoport. The upper airway in sleep: physiology of the pharynx. *Sleep Medicine Reviews*, 7(1):9–33, 2003.

Elias Balaras. Modeling complex boundaries using an external force field on fixed cartesian grids in large-eddy simulations. *Computers & Fluids*, 33(3):375–404, 2004.

Satish Balay, Shrirang Abhyankar, Mark F. Adams, Jed Brown, Peter Brune, Kris Buschelman, Lisandro Dalcin, Victor Eijkhout, William D. Gropp, Dinesh Kaushik, Matthew G. Knepley, Lois Curfman McInnes, Karl Rupp, Barry F. Smith, Stefano Zampini, Hong Zhang, and Hong Zhang. PETSc Web page, 2016. URL `http://www.mcs.anl.gov/petsc`.

TS Balint and AD Lucey. Instability of a cantilevered flexible plate in viscous channel flow. *Journal of Fluids and Structures*, 20(7):893–912, 2005.

A. Bannier. Immersed boundary method for coupled fluid-structure interaction problems.(master thesis). 2012.

Klaus-Jürgen Bathe. *Finite element procedures*. Klaus-Jurgen Bathe, 2006.

Klaus-Jürgen Bathe, Ekkehard Ramm, and Edward L Wilson. Finite element formulations for large deformation dynamic analysis. *International Journal for Numerical Methods in Engineering*, 9(2):353–386, 1975.

Ted Belytschko and William E Bachrach. Efficient implementation of quadrilaterals with high coarse-mesh accuracy. *Computer Methods in Applied Mechanics and Engineering*, 54(3):279–301, 1986.

Rajneesh Bhardwaj and Rajat Mittal. Benchmarking a coupled immersed-boundary-finite-element solver for large-scale flow-induced deformation. *AIAA Journal*, 50(7):1638–1642, 2012.

I Bijelonja, I Demirdžić, and S Muzaferija. A finite volume method for incompressible linear elasticity. *Computer methods in applied mechanics and engineering*, 195(44):6378–6390, 2006.

Stéphanie Buchaillard, Pascal Perrier, and Yohan Payan. A biomechanical model of cardinal vowel production: Muscle activations and the impact of gravity on tongue positioning. *The Journal of the Acoustical Society of America*, 126(4):2033–2051, 2009.

Sean M Caples, James A Rowley, Jeffrey R Prinsell, John F Pallanch, Mohamed B Elamin, Sheri G Katz, and John D Harwick. Surgical modifications of the upper airway for obstructive sleep apnea in adults: a systematic review and meta-analysis. *Sleep*, 33(10):1396, 2010.

Paola Causin, Jean-Frédéric Gerbeau, and Fabio Nobile. Added-mass effect in the design of partitioned algorithms for fluid–structure problems. *Computer methods in applied mechanics and engineering*, 194 (42):4506–4527, 2005.

Andrew SL Chan, Kate Sutherland, Richard J Schwab, Biao Zeng, Peter Petocz, Richard WW Lee, M Ali Darendeliler, and Peter A Cistulli. The effect of mandibular advancement on upper airway structure in obstructive sleep apnoea. *Thorax*, 65(8):726–732, 2010.

S Cheng, SC Gandevia, M Green, R Sinkus, and LE Bilston. Viscoelastic properties of the tongue and soft palate using mr elastography. *Journal of Biomechanics*, 44(3):450–454, 2011.

Alexandre Joel Chorin. Numerical solution of the navier-stokes equations. *Mathematics of computation*, 22 (104):745–762, 1968.

Franz Chouly, Annemie Van Hirtum, P-Y Lagrée, Xavier Pelorson, and Yohan Payan. Numerical and experimental study of expiratory flow in the case of major upper airway obstructions with fluid–structure interaction. *Journal of Fluids and Structures*, 24(2):250–269, 2008.

Julien Cisonni, NSJ Elliott, AD Lucey, and M Heil. A compound cantilevered plate model of the palate-uvula system during snoring. In *19th Australasian fluid mechanics conference*, volume 8, 2014.

TP Collins, GR Tabor, and PG Young. A computational fluid dynamics study of inspiratory flow in orotracheal geometries. *Medical & Biological Engineering & Computing*, 45(9):829–836, 2007.

Tommaso Cosentini, R Le Donne, D Mancini, and N Colavita. Magnetic resonance imaging of the upper airway in obstructive sleep apnea. *La Radiologia medica*, 108(4):404, 2004.

Christophe Daux, Nicolas Moes, John Dolbow, Natarajan Sukumar, and Ted Belytschko. Arbitrary branched and intersecting cracks with the extended finite element method. *Int. J. Numer. Meth. Engng*, 48:1741–1760, 2000.

DA Dunavant. High degree efficient symmetrical gaussian quadrature rules for the triangle. *International journal for numerical methods in engineering*, 21(6):1129–1148, 1985.

Th Dunne. An Eulerian approach to fluid–structure interaction and goal-oriented mesh adaptation. *International Journal for Numerical Methods in Fluids*, 51(9-10):1017–1039, 2006.

Lawrence J Epstein, David Kristo, Patrick J Strollo Jr, Norman Friedman, Atul Malhotra, Susheel P Patil, Kannan Ramar, Robert Rogers, Richard J Schwab, Edward M Weaver, et al. Clinical guideline for the evaluation, management and long-term care of obstructive sleep apnea in adults. *Journal of clinical sleep medicine: JCSM: official publication of the American Academy of Sleep Medicine*, 5(3):263–276, 2009.

EA Fadlun, R Verzicco, P_ Orlandi, and J Mohd-Yusof. Combined immersed-boundary finite-difference methods for three-dimensional complex flow simulations. *Journal of Computational Physics*, 161(1):35–60, 2000.

Kathleen A Ferguson, Rosalind Cartwright, Robert Rogers, and Wolfgang Schmidt-Nowara. Oral appliances for snoring and obstructive sleep apnea: a review. *Sleep*, 29(2):244–262, 2006.

R Fodil, C Ribreau, B Louis, F Lofaso, and D Isabey. Interaction between steady flow and individualised compliant segments: application to upper airways. *Medical and Biological Engineering and Computing*, 35(6):638–648, 1997.

RB Fogel, A Malhotra, and DP White. Sleep· 2: Pathophysiology of obstructive sleep apnoea/hypopnoea syndrome. *Thorax*, 59(2):159–163, 2004.

Yuan-cheng Fung. *Biomechanics: mechanical properties of living tissues*. Springer-Verlag, 1993.

Noam Gavriely and Oliver Jensen. Theory and measurements of snores. *Journal of Applied Physiology*, 74 (6):2828–2837, 1993.

Massimo Germano, Ugo Piomelli, Parviz Moin, and William H Cabot. A dynamic subgrid-scale eddy viscosity model. *Physics of Fluids A: Fluid Dynamics*, 3:1760, 1991.

Iain C Gleadhill, Alan R Schwartz, Norman Schubert, Robert A Wise, Solbert Permutt, and Philip L Smith. Upper airway collapsibility in snorers and in patients with obstructive hypopnea and apnea. *American Review of Respiratory Disease*, 143(6):1300–1303, 1991.

Roland Glowinski, T-W Pan, Todd I Hesla, and Daniel D Joseph. A distributed lagrange multiplier/fictitious domain method for particulate flows. *International Journal of Multiphase Flow*, 25(5):755–794, 1999.

D Goldstein, R Handler, and L Sirovich. Modeling a no-slip flow boundary with an external force field. *Journal of Computational Physics*, 105(2):354–366, 1993.

Intaek Hahn, PETER W Scherer, and Maxwell M Mozell. Velocity profiles measured for airflow through a large-scale model of the human nasal cavity. *Journal of Applied Physiology*, 75(5):2273–2287, 1993.

AF Heenan, E Matida, A Pollard, and WH Finlay. Experimental measurements and computational modeling of the flow field in an idealized human oropharynx. *Experiments in Fluids*, 35(1):70–84, 2003.

Jeffrey Lee Hellrung, Luming Wang, Eftychios Sifakis, and Joseph M Teran. A second order virtual node method for elliptic problems with interfaces and irregular domains in three dimensions. *Journal of Computational Physics*, 231(4):2015–2048, 2012.

Leonard R Herrmann. Elasticity equations for incompressible and nearly incompressible materials by a variational theorem. *AIAA journal*, 3(10):1896–1900, 1965.

Alexander Hrennikoff. Solution of problems of elasticity by the framework method. *Journal of applied mechanics*, 8(4):169–175, 1941.

Yaqi Huang, David P White, and Atul Malhotra. Use of computational modeling to predict responses to upper airway surgery in obstructive sleep apnea. *The Laryngoscope*, 117(4):648–653, 2007.

Soo-Jin Jeong, Woo-Seung Kim, and Sang-Jin Sung. Numerical investigation on the flow characteristics and aerodynamic force of the upper airway of patient with obstructive sleep apnea using computational fluid dynamics. *Medical engineering & physics*, 29(6):637–651, 2007.

JT Kelly, AK Prasad, and AS Wexler. Detailed flow patterns in the nasal cavity. *Journal of Applied Physiology*, 89(1):323–337, 2000.

John Kim and Parviz Moin. Application of a fractional-step method to incompressible navier-stokes equations. *Journal of computational physics*, 59(2):308–323, 1985.

C Kleinstreuer and Z Zhang. Laminar-to-turbulent fluid-particle flows in a human airway model. *International Journal of Multiphase Flow*, 29(2):271–289, 2003.

Ulrich Küttler and Wolfgang A Wall. Fixed-point fluid–structure interaction solvers with dynamic relaxation. *Computational Mechanics*, 43(1):61–72, 2008.

Ming-Chih Lai and Charles S Peskin. An immersed boundary method with formal second-order accuracy and reduced numerical viscosity. *Journal of Computational Physics*, 160(2):705–719, 2000.

Haoxiang Luo, Rajat Mittal, Xudong Zheng, Steven A Bielamowicz, Raymond J Walsh, and James K Hahn. An immersed-boundary method for flow–structure interaction in biological systems with application to phonation. *Journal of computational physics*, 227(22):9303–9332, 2008.

XY Luo and TJ Pedley. A numerical simulation of unsteady flow in a two-dimensional collapsible channel. *Journal of Fluid Mechanics*, 314:191–226, 1996.

Alain Lurie. Obstructive sleep apnea in adults: epidemiology, clinical presentation, and treatment options. *Advances in cardiology*, 46:1, 2011.

Sekhar Majumdar, Gianluca Iaccarino, and Paul Durbin. Rans solvers with adaptive structured boundary non-conforming grids. *Annual Research Briefs*, pages 353–366, 2001.

José Marin, Alvar Agusti, Isabel Villar, Marta Forner, David Nieto, Santiago J Carrizo, Ferran Barbé, Eugenio Vicente, Ying Wei, F Javier Nieto, et al. Association between treated and untreated obstructive sleep apnea and risk of hypertension. *Survey of Anesthesiology*, 57(1):50–51, 2013.

Jose M Marin, Santiago J Carrizo, Eugenio Vicente, and Alvar GN Agusti. Long-term cardiovascular outcomes in men with obstructive sleep apnoea-hypopnoea with or without treatment with continuous positive airway pressure: an observational study. *The Lancet*, 365(9464):1046–1053, 2005.

Miguel Ángel Martínez-García, Juan José Soler-Cataluña, Laura Ejarque-Martínez, Youssef Soriano, Pilar Román-Sánchez, Ferrán Barbé Illa, Josep María Montserrat Canal, and Joaquín Durán-Cantolla. Continuous positive airway pressure treatment reduces mortality in patients with ischemic stroke and obstructive sleep apnea: a 5-year follow-up study. *American journal of respiratory and critical care medicine*, 180(1): 36–41, 2009.

Edgar A Matida, Warren H Finlay, Michael Breuer, and Carlos F Lange. Improving prediction of aerosol deposition in an idealized mouth using large-eddy simulation. *Journal of aerosol medicine*, 19(3):290–300, 2006.

MATLAB Image Processing Toolbox. Matlab image processing toolbox, R2017a. The MathWorks, Natick, MA, USA.

Mihai Mihaescu, Shanmugam Murugappan, Maninder Kalra, Sid Khosla, and Ephraim Gutmark. Large eddy simulation and reynolds-averaged navier–stokes modeling of flow in a realistic pharyngeal airway model: An investigation of obstructive sleep apnea. *Journal of biomechanics*, 41(10):2279–2288, 2008.

Chohong Min and Frédéric Gibou. Geometric integration over irregular domains with application to level-set methods. *Journal of Computational Physics*, 226(2):1432–1443, 2007.

Rajat Mittal and Gianluca Iaccarino. Immersed boundary methods. *Annu. Rev. Fluid Mech.*, 37:239–261, 2005.

M Mohammad Rasani, K Inthavong, and J Tu. Simulation of pharyngeal airway interaction with air flow using low-re turbulence model. *Modelling and Simulation in Engineering*, 2011:1–9, 2011.

J Mohd-Yusof. Combined immersed-boundary/b-spline methods for simulations of ow in complex geometries. *Annual Research Briefs. NASA Ames Research Center= Stanford University Center of Turbulence Research: Stanford*, pages 317–327, 1997.

Il Joon Moon, Doo Hee Han, Jeong-Whun Kim, Chae-Seo Rhee, Myung-Whun Sung, Jong-Wan Park, Dong Sung Kim, and Chul Hee Lee. Sleep magnetic resonance imaging as a new diagnostic method in obstructive sleep apnea syndrome. *The Laryngoscope*, 120(12):2546–2554, 2010.

Nathan Mortimore Newmark. A method of computation for structural dynamics. In *Proc. ASCE*, volume 85, pages 67–94, 1959.

Yen Ting Ng, Chohong Min, and Frédéric Gibou. An efficient fluid–solid coupling algorithm for single-phase flows. *Journal of Computational Physics*, 228(23):8807–8829, 2009.

American Academy of Sleep Medicine. *International Classification of Sleep Disorders, 3rd Edition*. American Academy Of Sleep Medicine, 2014.

Eugenio Oñate, Jerzy Rojek, Robert L Taylor, and Olgierd C Zienkiewicz. Finite calculus formulation for incompressible solids using linear triangles and tetrahedra. *International journal for numerical methods in engineering*, 59(11):1473–1500, 2004.

Charles S Peskin. Flow patterns around heart valves: a numerical method. *Journal of Computational Physics*, 10(2):252–271, 1972.

Jernej Pirnar, Leja Dolenc-Grošelj, Igor Fajdiga, and Iztok Žun. Computational fluid-structure interaction simulation of airflow in the human upper airway. *Journal of biomechanics*, 48(13):3685–3691, 2015.

Andrew Pollard and Abdul-Monsif Shinneeb. Oro-pharangeal-laryngeal flow physics. In *Proceedings of the 17th Australasian Fluid Mechanics Conference, Auckland, New Zealand*, page 861, 2010.

Naresh M Punjabi. The epidemiology of adult obstructive sleep apnea. *Proceedings of the American Thoracic Society*, 5(2):136, 2008.

SF Quan, J Christian Gillin, MR Littner, and JW Shepard. Sleep-related breathing disorders in adults: Recommendations for syndrome definition and measurement techniques in clinical research. editorials. *Sleep*, 22(5):662–689, 1999.

JE Remmers, EK Sauerland, AM Anch, et al. Pathogenesis of upper airway occlusion during sleep. *Journal of Applied Physiology*, 44(6):931–938, 1978.

Valerij K Saulev. On solution of some boundary value problems on high performance computers by fictitious domain method. *Siberian Math. J*, 4(4):912–925, 1963.

Richard J Schwab, Krishanu B Gupta, Warren B Gefter, Louis J Metzger, Eric A Hoffman, and Allan I Pack. Upper airway and soft tissue anatomy in normal subjects and patients with sleep-disordered breathing. significance of the lateral pharyngeal walls. *American journal of respiratory and critical care medicine*, 152(5):1673–1689, 1995.

Richard J Schwab, Michael Pasirstein, Robert Pierson, Adonna Mackley, Robert Hachadoorian, Raanan Arens, Greg Maislin, and Allan I Pack. Identification of upper airway anatomic risk factors for obstructive sleep apnea with volumetric magnetic resonance imaging. *American journal of respiratory and critical care medicine*, 168(5):522–530, 2003.

B Shome, LP Wang, MH Santare, AK Prasad, AZ Szeri, and D Roberts. Modeling of airflow in the pharynx with application to sleep apnea. *Transactions of the ASME-K-Journal of Biomechanical Engineering*, 120 (3):416–422, 1998.

Joseph Smagorinsky. General circulation experiments with the primitive equations: I. the basic experiment*. *Monthly weather review*, 91(3):99–164, 1963.

Philip L Smith and ALAN R Schwartz. Biomechanics of the upper airway during sleep. *Sleep Apnea Pathogenesis, Diagnosis and Treatment*, pages 27–52, 2011.

Philip L Smith, Robert A Wise, Avram R Gold, Alan R Schwartz, and Solbert Permutt. Upper airway pressure-flow relationships in obstructive sleep apnea. *Journal of Applied Physiology*, 64(2):789–795, 1988.

Ian Stavness, John E Lloyd, and Sidney Fels. Automatic prediction of tongue muscle activations using a finite element model. *Journal of biomechanics*, 45(16):2841–2848, 2012.

Xiuzhen Sun, Chi Yu, Yuefang Wang, and Yingxi Liu. Numerical simulation of soft palate movement and airflow in human upper airway by fluid-structure interaction method. *Acta Mechanica Sinica*, 23(4): 359–367, 2007.

Theodore Sussman and Klaus-Jürgen Bathe. A finite element formulation for nonlinear incompressible elastic and inelastic analysis. *Computers & Structures*, 26(1):357–409, 1987.

Fang-Bao Tian, Hu Dai, Haoxiang Luo, James F Doyle, and Bernard Rousseau. Fluid–structure interaction involving large deformations: 3d simulations and applications to biological systems. *Journal of computational physics*, 258:451–469, 2014.

Stefan Turek and Jaroslav Hron. Proposal for numerical benchmarking of fluid-structure interaction between an elastic object and laminar incompressible flow. In Hans-Joachim Bungartz and Michael Schäfer, editors, *Fluid-Structure Interaction*, volume 53 of *Lecture Notes in Computational Science and Engineering*, pages 371–385. Springer Berlin Heidelberg, 2006. ISBN 978-3-540-34595-4.

Fredrik Valham, Thomas Mooe, Terje Rabben, Hans Stenlund, Urban Wiklund, and Karl A Franklin. Increased risk of stroke in patients with coronary artery disease and sleep apnea a 10-year follow-up. *Circulation*, 118(9):955–960, 2008.

Marcos Vanella, Patrick Rabenold, and Elias Balaras. A direct-forcing embedded-boundary method with adaptive mesh refinement for fluid–structure interaction problems. *Journal of Computational Physics*, 229 (18):6427–6449, 2010.

WDBJ Vos, Jan De Backer, Annick Devolder, O Vanderveken, Stijn Verhulst, Roberto Salgado, Paul Germonpré, Bart Partoens, Floris Wuyts, P Parizel, et al. Correlation between severity of sleep apnea and upper airway morphology based on advanced anatomical and functional imaging. *Journal of biomechanics*, 40(10):2207–2213, 2007.

Bart Vossen, HR Javani Joni, and RHJ Peerlings. Volumetric locking in finite elements. 2008.

Ying Wang, Jie Wang, Yingxi Liu, Shen Yu, Xiuzhen Sun, Shouju Li, Shuang Shen, and Wei Zhao. Fluid–structure interaction modeling of upper airways before and after nasal surgery for obstructive sleep apnea. *International Journal for Numerical Methods in Biomedical Engineering*, 28(5):528–546, 2012.

David C Wilcox. Comparison of two-equation turbulence models for boundary layers with pressure gradient. *AIAA journal*, 31(8):1414–1421, 1993.

Chun Xu, SangHun Sin, Joseph M McDonough, Jayaram K Udupa, Allon Guez, Raanan Arens, and David M Wootton. Computational fluid dynamics modeling of the upper airway of children with obstructive sleep apnea syndrome in steady flow. *Journal of biomechanics*, 39(11):2043–2054, 2006.

J. Yang and E. Balaras. An embedded-boundary formulation for large-eddy simulation of turbulent flows interacting with moving boundaries. *Journal of Computational Physics*, 215(1):12–40, 2006.

Tao Ye, Rajat Mittal, HS Udaykumar, and Wei Shyy. An accurate cartesian grid method for viscous incompressible flows with complex immersed boundaries. *Journal of Computational Physics*, 156(2):209–240, 1999.

Terry Young, Mari Palta, Jerome Dempsey, James Skatrud, Steven Weber, and Safwan Badr. The occurrence of sleep-disordered breathing among middle-aged adults. *New England Journal of Medicine*, 328(17):1230–1235, 1993.

Paul A. Yushkevich, Joseph Piven, Heather Cody Hazlett, Rachel Gimpel Smith, Sean Ho, James C. Gee, and Guido Gerig. User-guided 3D active contour segmentation of anatomical structures: Significantly improved efficiency and reliability. *Neuroimage*, 31(3):1116–1128, 2006.

Hong Zhao, Jonathan B Freund, and Robert D Moser. A fixed-mesh method for incompressible flow–structure systems with finite solid deformations. *Journal of Computational Physics*, 227(6):3114–3140, 2008.

Moyin Zhao, Tracie Barber, Peter A Cistulli, Kate Sutherland, and Gary Rosengarten. Simulation of upper airway occlusion without and with mandibular advancement in obstructive sleep apnea using fluid-structure interaction. *Journal of biomechanics*, 46(15):2586–2592, 2013.

Jian Hua Zhu, Heow Pueh Lee, Kian Meng Lim, Shu Jin Lee, Li San Lynette Teo, and De Yun Wang. Passive movement of human soft palate during respiration: A simulation of 3d fluid/structure interaction. *Journal of biomechanics*, 45(11):1992–2000, 2012a.

Yongning Zhu, Yuting Wang, Jeffrey Hellrung, Alejandro Cantarero, Eftychios Sifakis, and Joseph M Teran. A second-order virtual node algorithm for nearly incompressible linear elasticity in irregular domains. *Journal of Computational Physics*, 231(21):7092–7117, 2012b.